1988

c-Axis oriented barium(2) titanium silicon(2) oxygen(8) thin films.

Paul Michael. Kawa
University of Windsor

NOTICE

The quality of this microform is heavily dependent upon the quality of the original thesis submitted for microfilming. Every effort has been made to ensure the highest quality of reproduction possible.

If pages are missing, contact the university which granted the degree.

Some pages may have indistinct print especially if the original pages were typed with a poor typewriter ribbon or if the university sent us an inferior photocopy.

Previously copyrighted materials (journal articles, published tests, etc.) are not filmed.

Reproduction in full or in part of this microform is governed by the Canadian Copyright Act, R.S.C. 1970, c. C-30.

AVIS

La qualité de cette microforme dépend grandement de la qualité de la thèse soumise au microfilmage. Nous avons tout fait pour assurer une qualité supérieure de reproduction.

S'il manque des pages, veuillez communiquer avec l'université qui a conféré le grade.

La qualité d'impression de certaines pages peut laisser à désirer, surtout si les pages originales ont été dactylographiées à l'aide d'un ruban usé ou si l'université nous a fait parvenir une photocopie de qualité inférieure.

Les documents qui font déjà l'objet d'un droit d'auteur (articles de revue, tests publiés, etc.) ne sont pas microfilmés.

La reproduction, même partielle, de cette microforme est soumise à la Loi canadienne sur le droit d'auteur, SRC 1970, c. C-30.

Canada

c-AXIS ORIENTED $Ba_2TiSi_2O_8$ THIN FILMS

by.

PAUL MICHAEL KAWA

A Thesis

submitted to the

Faculty of Graduate Studies and Research

through the Department of

Engineering Materials in.Partial Fulfillment

of the requirements for the Degree

of Master of Applied Science at

the University of Windsor

Windsor,Ontario,Canada

1988

To My Mother

ABSTRACT

. The potential of piezoelectric Fresnoite ($Ba_2TiSi_2O_8$, henceforth B2TS2) in the form of a thin film has shown great promise theoretically. This has led to the fabrication of Ba-Ti-Si-O thin films, by r.f. triode sputter deposition, in an attempt to obtain a piezoelectric thin film for device application.

In order to obtain a piezoelectric thin film, the proper composition and structure of the source material are required. Target fabrication was scrutinized in an attempt to fabricate a better quality sputtering target. Previous procedures resulted in a non-equilibrated material being formed after sintering, with B2TS2 coexisting with $BaTiO_3$, Ba_2SiO_4 and $BaSiO_3$. These targets also contained large pores and fractured when exposed to the extreme heat of sintering and sputtering. A modified procedure, placing more emphasis on the powder grain size and grain boundary diffusion prior to sintering, resulted in a smoother, less porous target which did not fracture like previous attempts. This target was also in a full equilibrium, as B2TS2 was the only phase present after sintering.

Analysis of the B2TS2 targets was performed to determine their density, composition (energy dispersive spectroanalysis), and phase relations (x-ray diffractometry) before, during and after sintering. Raman spectroscopy was also used to study the bonding states of the ceramics.

The main objective of this study was to fabricate preferentially oriented thin films of B2TS2. Previous studies suggested that crystalline thin films could be obtained, in the as-deposited state, if the substrate was heated above 650°C. No such thin films had been fabricated, due to a lack of a high-temperature substrate heater with the ability to perform in a highly oxidized atmosphere under high vacuum. The development of a tantalum wire heater solved the problem of high-temperature deposition.

A thin film deposited at 300°C portrayed a polycrystalline morphology indicating that the crystalline transition temperature had been surpassed. Thus, thin films were deposited for 6 to 3 hours at 25°C intervals between 650 and 300°C. Analysis of the films showed the preferentially [00n] oriented morphology to exist between 700 and 750°C.

Thin films were deposited for extended periods of time in this range to obtain thicker films suitable for the study of their electronic properties. However, analysis of these thin films showed a polycrystalline structure existed.

Temperature decreases were then necessary to maintain the preferred orientation of the thin films. Tests performed on the thin films showed that decreases by as much as 50°C, after 4 hours, still allowed the polycrystalline morphology to exist, although the larger the decrease, the less intense were the non-preferred peaks. A further decrease is suggested to obtain a preferentially oriented morphology.

Compositional analysis of the thin films showed the films to have a higher Ti and Si content, when compared to the target material, although the Si increase is probably due to the effect of the Si substrate. Raman spectroscopy analysis is inconclusive at this time.

ACKNOWLEDGEMENTS

help, support and encouragement throughout the course of this study.

TABLE OF CONTENTS

TABLE OF CONTENTS (continued)

—

LIST OF TABLES

LIST OF FIGURES

Chapter I

INTRODUCTION

The electronics industry has grown very rapidly in the past few decades with the increasing demand of its applications on today's society. This increased demand has pumped new life into many electronics fields for both its research and development of new and old materials and in their applications to everyday living.

Of particular interest are devices fabricated in the thin film field. The commercial use of thin films has been growing at an increasingly rapid rate for the past several years, particularly in the electronics industry. Piezoelectric thin films have useful electrical and acoustical properties which have led to their applications in electromechanical transducers, including surface acoustic wave (SAW) devices such as oscillators, TV-IF filters, optical image scanners, and so on.

Since the first report of vapour deposited CdS thin films for VHF and UHF acoustic wave transducers by N.F. Foster, in 1963 [1], a number of investigations on piezoelectric thin films have been carried out using a variety of deposition

techniques.   Research has expanded to include   such binary
compounds as ZnO [2-15], AlN [11,16-19], and Ta_2O_5 [20] and
more complex compounds such as LiNbO$_3$ [21,22],   BaTiO$_3$
[23-25], PbTiO$_3$ [26-28],   and lead-zirconate-lead-titanate
(PZT) [29,30].   More recently, piezoelectric polymer elec-
trets of semicrystalline poly vinylidene fluoride (PVDF)
films have been produced [31-34].   These crystalline and
highly oriented piezoelectric thin films have been fabricat-
ed using a wide spectrum of techniques including chemical
vapour deposition (CVD), ion plating, reactive sputtering,
planar magnetron sputtering, and so on.   This increased
demand has rekindled interest in natural as well as artifi-
cially prepared materials for thin film fabrication.

One such material is a complex oxide called Fresnoite
($Ba_2TiSi_2O_8$,henceforth abbreviated B2TS2) which can be found
occuring naturally [35], or can be synthetically made
[36-40]. The crystallographic structure of b2TS2 was deter-
mined to be noncentrosymmetric tetragonal, P4bm [35], which
is indicative of a piezoelectric material [36,37] and this
was confirmed experimentally by M. Kimura et al. [41,43], J.
Eckstein et al. [42], and S. Haussuhl et al. [44].   The SAW
characteristics of B2TS2 were also investigated and it was
found that bulk, single-crystals showed little, if any,
advantages over existing materials [45,46], while thin films

deposited on fused quartz were calculated and predicted to be very useful in device application, if they were c-axis oriented [47]. The fabrication of c-axis oriented B2TS2 thin films, to this author's knowledge, have not yet been achieved.

Previous studies performed on Fresnoite have reported the successful fabrication of B2TS2 thin films [48-52]. However, although the films were smooth and continuous, they had an amorphous structure. M. Ayakawa [43] studied the crystallization process of amorphous B2TS2 thin films sputtered-deposited on fused quartz substrates. However, he did not succeed in obtaining c-axis oriented thin films. Various methods have been attempted to deposit thin films in the [001] orientation, from post annealing of the amorphous thin films [48-52] to heating the substrate during depositon [50,51]. Post annealing of the thin films above 700°C gave crystallized films on a (100) silicon single crystal substrate [51] and above 780°C on a fused quartz substrate [52]. In-situ heating of the substrate during deposition gave an indication of crystallinity on (100)Si at a temperature of 650°C [50].

The work performed here will consist of sputter depositing B2TS2 thin films at temperatures, in-situ, of 650°C and above for the purpose of determining the range of maximum c-axis orientation.

Chapter II

LITERATURE REVIEW

2.1 Piezoelectricity

Piezoelectric materials have the ability to become electrically polarized in response to an applied mechanical stress or vice versa [53]. The appearance of electric polarization due to an applied stress is known as the direct piezoelectric effect. When an electric field is applied to a piezoelectric crystal, it causes strain which produces stress and is known as the converse piezoelectric effect. Thus mechanical energy can be converted to electrical energy or the other way around. These piezoelectric effects were first discovered by Jacques and Pierre Curie in 1880.

Some piezoelectric materials contain dipoles, which are positive and negative charges of the same magnitude which do not coincide with each other. However, to obtain piezoelectricity, these dipoles must be oriented to a certain degree. The structure can be centrosymmetric in most planes while not symmetric in others (ie. 32TS2). Thus a small electric dipole is created along the non-symmetrical axis giving the material its piezoelectric property. The piezoelectric

effect is limited only to those crystals which have a non-centrosymmetric structure.

A linear relationship exists between the components of stress or strain and the electric field. This first order effect, known as the electromechanical coupling factor (k^2), is defined as follows [54] :

$$k^2 = \frac{\text{resultant electrical energy}}{\text{input mechanical energy}}$$

The electric field produced by an applied stress can be reversed by a direction or sign reversal in the stress. k^2 does not represent the absolute efficiency of a device, which is the ratio of useful converted power to input power. The latter quantity may be lower than k^2 at low frequencies but higher than k^2 at a resonance. For most applications, a high k^2 is desirable, that is the ability to convert energy readily from one form to another.

Piezoelectric materials can be classified into two categories. The first set of materials which show piezoelectricity because of their original crystal structure, includes 32TS2 and zinc-blend crystals such as ZnO and CdS. The other is for ferroelectric materials such as $BaTiO_3$, $LiNbO_3$, $PbTiO_3$, and PZT which have piezoelectricity only

after applying a high electric field below the Curie temperature. Of the 32 classifications of crystals, only 20 are piezoelectric. Ten of the piezoelectric groups are pyroelectric, in which crystals are able to change their polarization due to an increase in temperature. A subset of pyroelectric materials are ferroelectric materials which, along with what is mentioned above, also exhibit an electric dipole even in the absence of an electric field and can reverse or change the orientation of their polarization direction because of an electric field [53,55]. Although a subset of pyroelectricity, ferroelectricity cannot be predicted from crystal symmetry but must be tested for experimentally.

Since the discovery of piezoelectric $BaTiO_3$ in 1942, piezoelectric materials have been used for a wide range of applications including transducers and surface acoustic wave (SAW) devices. Table 1 summarizes some of the practical applications of piezoelectric materials.

2.2   SAW_Characteristics_and_Device_Applications

One of the most promising areas for the application of piezoelectric devices is in the field of surface acoustic waves (SAW's) [56,57]. SAW's were first described by Lord Rayleigh in a theoretical investigation in 1885. Some of the more important types of acoustic waves that can travel

through a solid are: longitudinal waves, transverse, waves, and Rayleigh waves (Figure 1). Longitudinal waves are the simplest type of elastic wave in which the material is alternately compressed and expanded. The transverse, or shear, wave allows acoustic energy to travel through a solid by oscillating the materials particles from side to side at right angles to the acoustic signal. The third type of wave is the Rayleigh (or SAW) wave which exists only near the free surface of a solid. The Rayleigh wave incorporates both the longitudinal and transverse waves in phase, which are required to satisfy the boundary conditions, while a force normal to the surface is zero. This wave travels along the surface of the solid much like ripples on the surface of a pond. The Rayleigh wave is the wave type of most interest to thin film applications.

Piezoelectric materials used for the purpose of SAW devices have their Rayleigh waves excited by the application of electrical signals. Each SAW produced on the material contains a small amount of electric energy which provides a physical mechanism for the coupling of electromagnetic signals and propagating SAW's. The SAW's excited in this manner can be used to filter out signals, to amplify weak signals or to store signal for later use. The waves can be easily excited anywhere on the piezoelectric materials sur-

face and readily collected anywhere on the same surface. Also, because the wave is so easily accessible, signals with different delay times can be tapped at various points along their path.

The first acoustic wave devices employed either transverse or longitudinal waves passing through the interior of the solid material. Also, an efficient transducer for converting electrical signals into mechanical signals was unheard of. These volume-wave devices produced waves with low frequencies.(10^1-10^4 Hz). However, with the discovery of Rayleigh waves and the development of the interdigital transducer (IDT), SAW technology has expanded rapidly with frequencies above 10^7 Hz.

There are many parameters which are used to characterize the suitability of a piezoelectric material for SAW applications. However, the two most important factors are the electromechanical coupling factor (k^2), as described previously, and the temperature coefficient of delay (TCD). k^2 will vary depending on the geometry under investigation and indicates the direct estimation of electromechanical coupling to IDT's. The TCD relates the velocity of the SAW phase to the thermal expansion coefficient along the SAW propagation direction. The TCD can be useful for material characterization and it can be important in device functions where ambient temperature changes could cause unwanted

changes in device performance. Ideally, for SAW applications, a high k^2 value and a TCD of zero are required for piezoelectric materials. No such materials exist yet [58], so usually there is an unfavourable trade-off between the TCD and k^2 values in most materials [59].

The discovery of Rayleigh waves, which concentrates the SAW energy on the surface of the material, made possible the generation, detection and control of waves on the surface of the material instead of internally. This made possible the microminiaturization of SAW devices and their fabrication economically feasible to the electronics industry. Piezoelectric materials are used for a wide range of SAW applications and can be divided up into three categories: piezoelectric single crystals, piezoelectric ceramics, and piezoelectric thin films. Each will be discussed below.

2.2.1 Single Crystals

One of the most studied single crystals for its piezoelectric applications is quartz. Quartz is a physically and chemically stable material, with a high Q and low TCD which are ideal properties for oscillators, resonators and narrow-band signal processors. However, quartz cannot be applied for filters, resonators, or transducers of a wide band width because of its small k^2 value (ST-cut quartz ~ 0.0016). Also, as with all single crystals, Quartz must be cut in a

certain crystal direction for particular vibrational modes to be enhanced. The importance of quartz and its large demand has led to synthetic quartz being mass-produced by the hydrothermal process. Other piezoelectric compounds include Rochelle salt and ammonium dihydrogen phosphate (ADP), which have very high k^2 values but are water soluble; and ZnO, CdS, and LiNbO$_3$, which are used as high k^2 crystals for resonators and transducers. However, most are not in use anymore because of the development of piezoelectric ceramics and thin films. The SAW characteristics of single crystal 32TS2 were theoretically calculated [45,46] and found to be between LiNbO$_3$ and LiTaO$_3$ (Figure 2).

2.2.2 Piezoelectric Ceramics

With the discovery of BaTiO$_3$ in 1942, while trying to improve the permittivity in titanate ceramic materials, piezoelectric ceramics have taken on a wide range of applications. Ceramics are usually oxide powders which are compressed and sintered at high temperatures to form a polycrystalline mass. This mass would be intrinsically isotropic because its properties would be averaged over all crystal directions. However, when heated and cooled in the presence of an electric field, poling occurs as in BaTiO$_3$ ceramics (ferroelectricity). Thus, ferroelectric ceramics obtain their properties from the impregnating of a polar

axis.   Most ferroelectric ceramic materials have a perovskite structure including $BaTiO_3$ and $PbTiO_3$

Piezoelectric ceramics have many advantages over single crystals and piezoelectric thin films in that they could have higher k^2 values, are easier to prepare, can be fabricated into many shapes and sizes, and the polarization axis can be selected. Disadvantages of piezoelectric and ferroelectric ceramics include a high dielectric constant, a porous structure, and a high TCD. Again, however, the unfavourable trade off between these factors occurs for most materials [59].

$BaTiO_3$ ceramics were the first of a completely new type of material and they ensured the possibility of a wide range of piezoelectric applications for the future.   Initially $BaTiO_3$ and $PbTiO_3$ ceramics were used in low frequency, ultrasonic transducers (as fish finders and sonars) and are still in use today (in piezoelectric speakers and buzzers, etc.), although they have been improved and modified. Due to the weak temperature stability of pure $BaTiO_3$ and $PbTiO_3$ at high frequencies, many studies were performed to find high quality ceramics.   In 1965, $PbTiO_3$ ceramics were discovered to be a practical piezoelectric material of excellent quality, but with slight additions of compounds (ie. Mn, Ca, Bi, Nb, etc.) [60], and are now used mainly for high

frequency filters for televisions [61]. Lead-zirconate-titanate (PZT) ceramics were developed and solved the temperature stability problem. With the advantage of a large k^2 value, PZT ceramics were initially applied to mechanical filters for uses ranging from radio communications to telephone channel filters and later for piezoelectric ignitors, high frequency acoustic transducers and medical transducers [62].

Since only ferroelectric materials were able to reorient their polar axis in ceramics under a high electrical field so as to impart a long-range remnant polar order for use in piezoelectric applications, many attempts were made to impart a polar axis in nonferroelectric materials which have interesting single crystal properties. Halliyal et al. [63,64] developed a glass-ceramic which provided a polar texture during the formation of the crystallites. Although used extensively in the electronics industry for non-piezoelectric applications, studies performed by the aforementioned have shown that glass-ceramics can be prepared for inexpensive, large-area, pyroelectric detectors and piezoelectric resonators. Glass-ceramics is a growing field to be reckoned with in the future.

2.2.3   Piezoelectric Thin Films

Recently, considerable attention has been focussed on piezoelectric thin films because of their many possible applications to electronic devices and integrated circuit technology.   Highly oriented piezoelectric thin films have been fabricated using a variety of methods including chemical vapour deposition (CVD), reactive sputtering, planar mangetron sputtering, and r.f. sputtering.   The advantages of piezoelectric thin films over single crystals and ceramics include:

1.   the size and shape, which have led to the microminiaturization of many piezoelectric devices.   .

2.   the control of effective material constants by choosing suitable substrate and thin film materials.

3.   the control of the piezoelectric characteristics of a thin film by controlling the layer thickness and the microstructure (ie. grain size and orientation, local composition, etc).

4.   relatively easy and inexpensive fabrication methods.

5.   the fabrication of high frequency, temperature stable, piezoelectric devices.

In order to obtain a piezoelectric thin film (of a material with a tetragonal structure) with properties similar to that of a single crystal, the piezoelectric (or c-)

axis, which has the dipole moment along it, should be oriented perpendicular to the substrate surface. The a and b axes can be randomly oriented in the plane parallel to the substrate surface. This type of structure is called a columnar structure (Figure 3) and may be produced during the depositon process.

The first piezoelectric thin films were obtained by a vapour deposition technique in 1963, when N.F. Foster produced a CdS thin film [1] used for an ultrasonic transducer in VHF and UHF bands. In 1365, ZnO thin films were initially fabricated by reactive sputtering [2] and because these thin films drew such wide attention for their most effective piezoelectric properties (particularily in the generation and detection of SAW's), most of the above fabrication techniques have been utilized to form highly oriented ZnO thin films for transducers [2-15]. In the early 1970's, SAW transducers studies were performed on ZnO thin films [4-7] and in 1974, ZnO thin films were fabricated in the frequency range from audio frequency to 100 MHz. This coupled with its large electromechanical coupling factor and low dielectric constant allowed ZnO to be applied for bulk acoustic wave and SAW devices [11-15]. AlN thin films are another highly investigated piezoelectric material since their fabrication by reactive sputtering in 1962 [16]. With a

crystal structure similar to that of ZnO thin films, and an acoustic velocity and thermal stability higher than both ZnO and CdS [16]. AlN thin films are well suited for ultra-high frequency transducers (>1.0 GHz). Initial experimentation had AlN reactively sputter deposited on sapphire at relatively high temperatures [16,17] making it economically unfeasible. But with a change in deposition methods, oriented thin films are now being deposited at temperatures as low as 50°C with similar SAW characteristics [18,19]. Although the most highly investigated and widely used piezoelectric materials for thin films are the binary compounds ZnO and AlN, many other materials have been studied. These include other binary compounds such as Ta_2O_5 [20] and more complex compounds such as $LiNbO_3$ [21,22], $BaTiO_3$ [23-25], $PbTiO_3$ [26-28], and (PZT) [29,30]. The more complex compounds were studied because their ferroelectric properties brought forth many possible applications to electronic, piezoelectric, and pyroelectric devices. More recently even more multi-complex compounds have been studied, along with polymers such as PVDF [31-34], and these piezoelectric materials are found more and more in industrial applications.

Piezoelectric thin films can be used for transducers, oscillators, convolvers, optical image scanners and SAW

devices. In order to use SAW devices for high frequency, ultrasonic applications, a large k^2 value is required along with a low TCD (ie. in the order of 0-50 ppm/K [46]).

Determined to be a most promising temperature-compensated material for SAW device applications [65], H. Yamauchi et al. [47] theoretically investigated the piezoelectric properties of B2TS2 thin films deposited on a fused quartz substrate. They found that for a Z·45°Y B2TS2 thin film, a low TCD and a high k^2 value resulted which was comparable to ZnO and also more thermally stable. These promising and possible piezoelectric results have led us to attempt to fabricate c-axis oriented B2TS2 thin films.

2.3 Fresnoite

Until 1965, when J.T. Alfors et al. [35] discovered crystals of Fresnoite (B2TS2), as one of seven new barium silicates, during a geological study of the sanbornite deposits of eastern Fresno county, California, this naturally occurring mineral was unheard of. B2TS2, whose chemical formula is $Ba_2TiSi_2O_8$, was not even investigated during a study of the $BaTiO_3-SiO_2$ system by D.E. Rase et al. in 1955 [66]. In fact, part of their findings has been widely disputed and will be discussed later in Appendix A.

In 1967, R. Masse et al. [36] investigated the structure of synthetic B2TS2 crystals while P. B. Moore et al. [37] determined the structure from a natural crystal. Both groups agreed that the crystal structure of B2TS2 was non-centrosymmetric tetragonal and in the space group P4bm as previously determined [35]. The lattice constants of B2TS2 are a=b=0.852nm and c=0.521nm [36]. The crystal structure, interatomic distances, and bond angles were determined, and used to construct the B2TS2 unit cell projected onto the X-Y and X-Z planes, as shown in Figures 4 and 5 respectively. The unit cell of B2TS2 consists of four silicon centred oxygen tetrahedra (one oxygen from each is shared with an independent pyrosilicate group) which are joined to a titanium centred oxygen square pyramid. The barium atoms are surrounded by ten oxygen atoms, six of which are nearest neighbours and four, more remote. Figure 4 shows that the B2TS2 unit cell is centrosymmetric in the X-Y plane while Figure 5 shows no such symmetry in the X-Z plane. In the X-Z plane, the positively charged ions (Ba^{2+}, Ti^{4+}, and Si^{4+}) are centred midway through the cell while the negatively charged ions (O^{2-}) are centred slightly below the midway point. This nonsymmetric alignment creates a net electrical polarization along the Z-axis. Thus B2TS2 is accentric and should possess polar properties like piezoelectric (but not

ferroelectric), electroptic, pyroelectric, and nonlinear effects. The structural results were later confirmed experimentally by G. Blasse [39] and C. R. Robbins [40] on synthetically grown single crystals and along with the structural analogies of B2TS2 and $Ba_2TiGe_2O_8$, whose synthetic single crystals have a large electromechanical coupling factor [67] B2TS2 was expected to be a better piezoelectric material than quartz. This led to the synthesis of large, single crystals of B2TS2, using the Czochralski method, by M. Kimura et al. [41] and J. Eckstein et al. [42], which in turn helped M. Kimura [43] and S. Haussuhl et al. [44], in 1977, to experimentally measure the piezoelectric effect of B2TS2 along with the elastic, dielectric, optical, electroptic, and thermal properties relevant for technical applications.

In the early 1980's, A. Halliyal et al. [63,64] analyzed the dielectric, piezoelectric and pyroelectric properties of B2TS2 glass-ceramics. The glasses and glass-ceramic showed pyroelectric responses of up to 50% of single crystals [63]. Electromechanical and hydrostatic piezoelectric measurements of the grain-oriented, glass-ceramic were comparable to other piezoelectric device oriented materials and seem to be an attractive material for piezoelectric devices [64]. In 1985, S. A. Markgraf et al. [55] and A. Halliyal et al. [53]

again studied the dielectric, piezoelectric, and pyroelectric properties of B2TS2 single crystals and glass-ceramics along with the x-ray structure. The crystal structure parameters were refined from single crystal x-ray intensity data collected from B2TS2 at 24°C and 300°C [63]. These values were in good agreement with the results obtained earlier by R. Masse et al. [36] and P. B. Moore et al. [37], although more precise. The dielectric properties of B2TS2 were measured between -150°C and 200°C and showed maximums for the dielectric constant, pyroelectric and planar coupling coefficients occurring at 160°C for single crystals and 120°C for glass ceramics. A minimum resonance frequency was observed at the same temperatures. Analysis of the single crystal x-ray data taken at 24°C and 300°C showed no change in crystal symmetry or space group of the crystal. Thus, an explanation of the sharp change in parameters at 160°C is unclear, although it was attributed to either a subtle structural change, which must be polar to polar, or a large oxygen displacement change of a few elastic constants, enough to cause a reversal.

In 1975, B2TS2 was listed among potential temperature-compensated materials for surface acoustic wave (SAW) devices [65]. Three years later, with the aid of material constants previously published by M. Kimura [43], J. Meln-

gailis et al. [45] determined the theoretical SAW character-
istics of bulk B2TS2 single crystals and also measured the
values along several orientations cut from single crystals.
These values were compared and found to be in good agree-
ment. H. Yamauchi [46] also calculated the SAW characteris-
tics of B2TS2 single crystals, taking into account the temp-
erature coefficients of the piezoelectric constants. Both
studies found the SAW characteristics of single crystal
B2TS2 to be rather intermediate, between $LiNbO_3$ and $LiTaO_3$.
However, in 1980, Y. Ito et al. [70] partially substituted
Sr for Ba in single crystals grown by the Czochralski method
and this/resulted in greatly lowered temperature coefficient
of delay (TCD) times with no change in the electromechanical
coupling factor when compared to B2TS2. In 1979, H. Yamau-
chi et al. [47] calculated the SAW characteristics for
c-axis oriented B2TS2 thin films deposited on fused quartz
and found a TCD equal to zero along with other useful SAW
characteristics. A low TCD and a high k^2 are required prop-
erties for SAW devices, although a trade-off between the two
properties is generally observed in most SAW materials [53].

H. Yamauchi's theoretical results [47] have led to an
extensive investigation into the fabrication techniques of
c-axis oriented B2TS2 thin films here at the University of
Windsor. M. Ayukawa [48] employed both rf diode magnetron

and rf triode sputter deposition techniques to fabricate B2TS2 thin films on a variety of substrate materials. B2TS2 thin films deposited at low temperatures resulted in amorphous structures on all substrates. Ayukawa determined the amorphous-to-crystalline transition temperature of B2TS2 to be in the range of 700°C to 800°C. Ayukawa, along with T. C. Murray [49] measured the degree of crystallinity in partially crystallized thin films using the x-ray diffraction data of annealed B2TS2 thin films. 100% crystallinity occured above 900°C. R.J. White [50] performed a compositional analysis on the B2TS2 thin films and target and found the thin films to have a Ba deficiency and a Ti excess, when compared to the target material. The sintered target was also found to be off-stoichiometric. A Ba-enriched target was fabricated but this also resulted in an off-stoichiometric thin film. Analysis of the sintered B2TS2 target found three distinct phases present, mainly B2TS2, $BaTiSiO_5$, and $BaSi_2O_5$ (These findings will be discussed later in this study). White also performed dielectric measurements on the B2TS2 ceramics, which he found comparable to B2TS2 single crystal values. Again, all the thin films deposited with a substrate temperature below 650°C were amorphous, except for the B2TS2 thin film deposited on (100) Si at 650°C which gave a slight indication of c-axis orien-

tation. Two resulting studies were used to confirm the structure of B2TS2 thin films. R.J. White et al. [51] confirmed the amorphous-to-crystalline transition temperature again to be above 700°C and the crystalline thin film to be comprised of four phases: B2TS2, BaTiSiO$_5$, BaTiSi$_2$O$_7$, and BaTiSi$_3$O$_9$. H. Yamauchi et al. [52] confirmed this morphology using TEM patterns of B2TS2 thin films deposited on NaCl. As-deposited thin films showed near-amorphous structures with a void network morphology, while a thin film annealed at 750°C, for ten hours, had an appreciable amount of amphorous material remaining along with a morphology of the aforementioned phases. After annealing, a considerable amount of flaking was seen on the thin film surface making post sputtering annealing unfeasible.   This was attributed to the difference in thermal expansion rates between the substrate and the thin film material. Again, as stated previously, no c-axis oriented B2TS2 thin films have been fabricated yet to this author's knowledge.

The physical and chemical properties of B2TS2 are listed in Table 2.

2.4   Sputter Deposition of Thin Films

Sputtering is a vacuum coating method wherein a coating material is "vaporized" by ion bombardment of a source, consisting of the material in question, and the recombination of the coating atoms on a substrate surface forming a solid [71]. This coating has the same chemical composition as the target, though it may or may not have the same physical properties. Sputtering as a source of material deposition into thin films was first reported in literature in 1852 [72], but only recently has a sufficient understanding of the complex processes occuring during, and simultaneously with, ion bombardment of solid surfaces allowed for the fabrication of high quality, single crystal, semiconducting thin films. Parallel development of ultra high vacuum technology, and high quality microanalysis techniques for identifying the microstructure and composition of the films has allowed the science of ion-surface interactions to grow [73].

Sputtering is essential to modern semiconductor technology for selective etching of patterns for device fabrication, substrate cleaning, and deposition of insulating and passivating layers as well as metal contacts. Sputter deposition is also used for the growth of active layers in commercial piezoelectric devices. Since sputtering is a physical phe-

nomenon, not related to the melting points or vapour pressures of elemental species, it is well suited for compound and alloy growth. The advantages of sputtering deposition compared to other deposition techniques are:

1. strong adhesion between film and substrate

2. versatility to be able to deposit thin films of almost any element or compound, conductive or non-conductive

3. ability to simultaneously sputter identical or different materials or use a gas to introduce one or more coating materials into the chamber (reactive sputtering)

4. sequentially sputter different targets to create a layered thin film

5. ability to deposit high melting point materials (ie. AlN)

6. fabrication of thick homogeneous films over large planar areas

7. a high degree of reproducibility

Minor disadvantages include:

1. slow deposition rates (less than 200 nm/minute)

2. target material must be available in smooth plate form

3. the cathode filament (in triode sputtering) is vulnerable to reactive gases, especially oxygen.

Sputtering involves placing the target material and substrate into a chamber, as shown schematically in Figure 6 [73], which is evacuated down to a pressure range around 10^{-7} Torr. The chamber is then backfilled with an inert gas (usually argon) to a pressure above 10^{-3} Torr. Through suitable electrodes (not shown in Figure 6), an electric (glow) discharge is created near the target causing the inert gas to ionize (plasma gas) adjacent to the target. The plasma gas is confined to the target area by surrounding magnets and a grounded shield. A power supply is utilized to maintain a negative potential to the target, relative to the plasma gas. This negative potential draws argon ions from the plasma which are accelerated towards the target, whereupon they strike the target with sufficient energy (greater than the binding energy of the material) to dislodge the atoms from the surface and cause them to be ejected in all directions. The substrate is suitably placed to intercept these atoms and thus form a continuous, solid thin film.

Incident ions (from the plasma gas) bombarding the target surface can create both elastic and inelastic collision effects as indicated schematically in Figure 7 [74]. The predominant effects depend primarily upon the energy and mass of the incident ions, the angle of incidence the masses of the lattice atoms involved, and the texture and orienta-

tion of the target. Under typical sputter deposition conditions, most of the ejected target material is in the neutral atomic state.

In recent years, various sputtering techniques have been developed and improved so that almost any material can be sputter deposited. Therefore, sputter deposited films have been successfully fabricated for piezoelectric devices such as SAW devices. However, to obtain a piezoelectric thin film for SAW device applications, the thin film must be c-axis oriented perpendicular to the substrate surface (Figure 3). Piezoelectric B2TS2 is an electrically insulating material and thus sputtering must be performed in the r.f. sputtering mode.

Chapter III

EQUIPMENT REVIEW

3.1   R.F. Triode Sputtering

R.F. (radio frequency) triode sputtering is one of the most common methods used to sputter deposit insulating materials such as oxides.   Conventional sputtering methods cannot be used due to a charge build-up which occurs on the surface of these materials. In r.f. sputtering, a high r.f. voltage is applied between the target and the substrate when the target is negatively charged, causing the positive ions in the plasma gas to strike the target surface.   Once a charge build-up occurs, the phase shifts by 90° making the target positively charged.   Thus the positive ions are repelled out of the target allowing the target surface to remain electrically neutral.

Triode sputtering is obtained using a magnetron supported triode r.f.   sputtering gun[1] installed in the sputtering deposition system at the University of Windsor. A schematic diagram of the type of triode sputtering source is shown if Figure 6. . In triode sputtering, the filament is heated by

---

[1] Tri-Mag model 3121 assembled by L.M. Simard, Inc., Santa Barbara, California

an a.c. current sufficiently high enough to allow for ther-
mionic electrons to be emitted from its surface. These
electrons are attracted to an anode biased positively by a
high voltage d.c. power supply. Argon gas atoms let into
the target area collide with the accelerated electrons where
they become ionized (due to collision) and create a self-
sustaining arc-type plasma. Sufficient filament-anode volt-
age, argon gas atoms and electrons are required to maintain
the plasma. Control of the plasma current is maintained
with a constant-current d.c. supply while the plasma voltage
supply is maintained by adjustment of both the argon gas
flow and the filament electron emission. Advantages of
triode sputtering include plasma being obtained at low pres-
sures and independently from the power applied to the tar-
get. A schematic illustration and overall view of the r.f.
triode sputtering deposition system can be seen in Figures
3(a) and 3(b) respectively.

3.2   Substrate Heater

In order to obtain a c-axis oriented thin film perpendic-
ular to the substrate, it was necessary to heat the subs-
trate "in-situ" while sputtering. This was made possible
with the design and fabrication of a Tantalum wire heater,
shown in Figure 10. High purity Ta wire[2], 0.25mm in diame-

---

[2] AESAR, Johnson Matthey Inc., 99.95%, cat. no. 10348A.

ter, was threaded through a stainless steel frame and placed inside a stainless steel box. Ceramic sleeves[3] were placed between the Ta wire and the stainless steel frame to electrically insulate the wire from the rest of the heater. This heater box was placed inside another stainless steel box which contained the substrate and holder. A stainless steel heat deflector was placed on top to deflect the heat downwards and thus maximize the effect of the heater.

3.3 Differential Thermal Analyzer

The differential thermal analyzer (DTA) unit[*], shown in Figure 11, measures the temperature difference between the sample material and a standard material which is non-reactive (in our case Al_2O_3) The materials are heated at a constant rate from room temperature to a temperature above the melting point of the sample material. Thermocouples connected to both samples record any temperature differences by detecting endothermic or exothermic reactions due to thermodynamical phase changes in the sample material. The temperature difference is plotted on a DTA graph versus the temperature of the standard. A non-reacting material has a gently sloping curve and any deviation in this curve is the

---

[3] Omega Engineering Inc., cat. no. SH-1-24

[*] Harrop Laboratories, Differential Thermal Analyser DT-715 and Control Console TA-700

result of a chemical reaction.

3.4 X-Ray Diffraction

In order to determine the existing phases and the crystal structure of the ceramic targets and thin films, x-ray diffraction (XRD) was used. Analyses are qualitative and semi-quantitative. Each compound produces a unique x-ray pattern or "finger print" and the intensity of this pattern indicates the quantity of this compound present in the specimen. Monochromatic CuKα (λ=0.15418 nm) radiation from a Cu x-ray tube, operating at 40 kV and 20 mA, was used. Diffracted x-rays are detected by a counter connected to a chart recorder with a scanning rate of 2°/minute. The diffraction peaks were identified using the JCPDS diffraction file cards shown in Table 3. A schematic diagram and photograph of the x-ray diffractometer[5] used are shown in Figures 12 and 13, respectively.

3.4.1 Inverse Pole Figures

The inverse pole figure shows the distribution of a selected direction in the specimen relative to the crystal axes [75]. The projection plane for an inverse pole figure is thus a standard projection of the crystal, of which only a unit stereographic triangle need be shown. It should be

---

[5] XRD:Philips model PW1011/60.

noted that an inverse pole figure shows immediately the crystallographic "direction" of any scatter.

The inverse pole figure comes from the analysis of the x-ray diffraction data. For randomly oriented crystals, the relative intensity of x-ray reflections, I_r, depends on five factors [77]: 1) the structure factor, F_{hkl}, 2) the multiplicity factor, P_{hkl}, 3) the Lorentz Polarization Factor, $(1 + \cos 2\theta)/(\sin \theta \cos \theta)$, 4) the temperature factor, $\exp(-2m)$, and 5) the absorption factor, $A(\theta)$. Thus, I_r can be expressed as:

$$I_r = F_{hkl} * P_{hkl} * \exp(-2m) * A(\theta) * (1+\cos 2\theta)/(\sin \theta \cos \theta) \quad (1)$$

Hence, the probability of a crystal axis taking any direction is impartial. However, if most of the crystal axes take up a certain direction, the crystals' orientation can be considered and is represented in terms of the volume fraction, $p(\alpha,\beta)$, of material with repsect to a certain crystal direction (ie. plane) [76,77]. The variables α and β, defining the crystal orientation, depend only on the indices, hkl, of the reflecting plane normal to the crystal direction. Harris [77] introduced the inverse pole figure method and described the pole density in terms of the ratio I_{hkl}/I^0_{hkl} as:

$$I_{hkl}/I^0_{hkl} = (C/Co) \, p(\alpha,\beta) \quad (2)$$

where I^o_{hkl} and I_{hkl} are the diffraction intensities of randomly oriented and preferentially oriented samples, respectively; C and Co are parameters which depend on the crystal imperfection, surface preparation (eg. oxide layer thickness), the absorption coefficient in the specimen, effective line breadth, and instrumental factors. Since p is normalized in such a way that upon integration $(1/n)$ $p(\alpha,\beta) = 1$, $p(\alpha,\beta)$ can be calculated following:

$$p(\alpha,\beta) = (I_{hkl}/I^o_{hkl})/\{(1/n)<(I_{hkl}/I^o_{hkl})\} \qquad (3)$$

Thus if $p(\alpha,\beta) = 1$, the crystals are randomly oriented; if $p(\alpha,\beta)<1$, the crystals are short of orientation; if $p(\alpha,\beta)>1$, the crystals are preferrentially oriented.

Since Harris' method depends on the measurement of diffracted intensities by a large number of planes in order to achieve a thorough coverage of orientation, most results are usually discontinuous and spotty.

The following procedure was used to obtain an inverse pole figure:

1. a stereo-projection figure of a B2TS2 crystal was drawn. Figure 14 schematically shows the designation of a stereo-projection figure. All the two-dimensional coordinates of every crystal plane with

the c-axis of a tetragonal unit cell perpendicular to the equatorial plane and the a and b axes (where a=b) parallel to the plane were calculated.

2. the x-ray diffraction pattern of a randomly oriented B2TS2 crystal was obtained. A B2TS2 thin film obtained when deposited at 480°C and annealed at 725°C for 10 hours [51] possessed a non-preferred orientation and thus was used for these calculations.

3. the pole density, $p(\alpha,\beta)$ was calculated. Since Harris' derivation of the inverse pole figure, many methods with quite accurate results have come into use. One such method studied by Hotta [73] took the multiplicity of the crystal plane, P_{hkl}, into account:

$$p(\alpha,\beta)=(P_{hkl})*(I_{hkl}/I^0_{hkl})/[P_{hkl}*(I_{hkl}/I^0_{hkl})] \quad (4).$$

Both Harris' and Horta's method were utilized in this study and their differences were determined.

4. drawing the inverse pole figure. The $p(\alpha,\beta)$ values were given in the (001) stereo-projection figure by means of contour lines (where p=constant)

Finally, it should be noted that an inverse pole figure is a two-dimensional plot that fixes, at a point, only a direction in space, be it crystal space or specimen space. Only a three-dimensional plot afforded by the crystal orien-

tation distribution can completely describe the orientation present.

3.5 Optical Microscopy

Optical micrographs were taken of the thin films at various temperatures in order to observe the microstructural changes. A Bausch and Lomb Stereo Zoom microscope along with a halogen lamp for lighting, available in the Department of Engineering Materials, were used to photograph the thin films on Kodak ektapan film. All micrographs were taken at approximately 400 times magnification.

3.6 Thin Film Thickness Measurements

A multiple beam interferometer[6] was used to measure the thickness of the films (Figure 15). This instrument provides an absolute measurement of vertical surface variations between 3 and 2,000 nm ± 1 nm. The interferometer employs a sodium vapour lamp with an effective wavelength of 533.2 nm. The light is optically directed to a specially coated Fizeau plate, as indicated in Figure 16, which makes contact with the specimen at a slight angle and forms an air wedge. Figure 17 shows how an interference fringe pattern is produced in the air wedge when a series of reflected light beams all converge at one point (point A). As the light beams con-

---

[6] Varian, model no. 980-4000.

verge, phase interference produces a fringe line which is transmitted through the Fizeau plate to a filar eyepiece for viewing as shown in Figure 18. The spacing and shape of the fringe lines can be interpreted to determine an extremely accurate contour of the specimen surface. Any two adjacent fringe lines are separated by half the wavelength of the monochromatic beam, $\lambda/2$. By adjusting the relative positions of the flats to form a wedge-shape air gap, the fringes can be made to run in straight lines perpendicular to the steps on the opaque film. The fringes show a displacement as they pass over the film step edge and give the film thickness. The film thickness can be calculated using the following equation:

$$\text{Film Thickness }(10^{-1}\text{nm}) = \frac{\text{Fringe Offset}}{\text{Fringe Spacing}} \quad \text{x294.6 nm} \quad (5)$$

The fringe offset and fringe spacing are measured with the filar eyepiece as shown in Figure 18.

Figure 17 also shows why a highly reflective specimen and Fizeau plate are required. Since the light beam is reflected many times before converging at point A, low reflectivity would reduce the total number of beams forming a fringe and would result in broader fringe lines and less accurate measurements.

3.7 Energy Dispersive Spectometry Analysis

A quantitative analysis of the sintered ceramic target and thin films was performed using an energy dispersive x-ray spectrometry (EDS) analyzer (Figure 19)[7] attached to a scanning electron microscope (SEM) (Figure 20)[9] available in the Department of Engineering Materials, University of Windsor. The analysis took place using an operating voltage of 15 keV and a counting time of 30 seconds at a magnification of 2,000 times. The SEM was used to observe the grain size of the powdered ceramics, the effectiveness of the sintering, and microstructural features of the ceramics. The specimens were coated with carbon to prevent an electrical charge build-up on the specimens.

3.8 Raman Spectroscopy

Raman spectroscopy depends on the frequency of the light scattered by molecules as they undergo rotations and vibrations. When a monochromatic light of frequency vo is directed at a cell containing a dust-free transparent substance, most of the light passes through it unaffected. However, some of the light (approximately 0.1 percent) is scattered by the sample molecules in all directions, as shown in Figure 21. The scattered radiation contains photons which

---

[7] EDS: Kevex, model no. 5100 XR ES

[9] SEM: SEMCO Nanolab 7

have the same frequency, vo, as the incident light (elastic

scattering which is often called the Rayleigh line), but, in

addition, the emergent radiation contains other frequencies

(due to inelastic scattering) such as $(vo - v_1)$ and $(vo +$

$v_1)$. This was observed by Raman [79,80] in 1928 (the Raman

shifts). Since, in thermal equilibrium, the population of

higher energy modes is less than that of lower energy modes

and falls off exponentially with the energy, Raman shifts

with a positive Δv (anti-Stokes lines) are less intense than

those with a negative Δv (Stokes lines), and the intensity

of the anti-Stokes lines falls off rapidly as Δv increases.

The phenomena of fluorescence and Raman scattering must

be distinguished. In fluorescence, the incident photon is

completely absorbed and the molecule concerned is thereby

raised to an excited electronic-level. After a certain

lifetime in this upper state, the molecule undergoes a down-

ward transition and thereby re-radiates light of a frequency

lower than that which it had absorbed [31]. This mechanism

is radically different from that of the Raman effect, in

which the photon as a whole is never absorbed, but rather

perturbs the molecule and induces it to undergo a vibration-

al or rotational transition (see Figure 22) [32]. Each

scattering species gives its own characteristic vibrational

Raman spectrum, which can be used for its qualitative iden-

tification.   The experimental set up is schematically shown
in Figure 23) [32].

Chapter IV

EXPERIMENTAL PROCEDURE

4.1 Fabrication of the Ceramic Sputtering Target

The ceramic sputtering targets were fabricated using high purity $BaCO_3$[9], SiO_2[10], and TiO_2[11] powders. The formation of B2TS2 is shown by the following reaction:

$$2BaCO_3 + TiO_2 + 2SiO_2 \longrightarrow Ba_2TiSi_2O_8 + CO_2 \quad (6)$$

Barium carbonate ($BaCO_3$) was used in place of BaO in this research to improve the mixing properties by avoiding the formation of $Ba(OH)_2$ agglomerates, when water is added to the oxide powder mixture.

The fabrication procedure used for this work was adopted from previous work performed on B2TS2 [50]. This procedure was a modification of the previous results, which, after careful analysis, were changed in areas of major emphasis due to difficulties encountered with the final product.

---

[9] Fisher Scientific Co., cat. no. B-30.

[10] Fisher Scientific Co., cat. no. T-345.

[11] Fisher Scientific Co., cat. no. S-662.

i.   STEP 1: The $BaCO_3$, TiO_2, and SiO_2 powders
      were each dried separately at 400°C for 4
      hours in an oven to remove any moisture.

ii.   STEP 2: After heating, the powders were
      immediately weighed to determine their
      stoichiometric weight. This procedure was
      repeated until the desired stoichiometric
      proportion of each oxide powder was
      obtained. The ratios of each powder can
      be seen in Table 4.

iii. STEP 3: The powders were mixed together.
      If more than 100 g of the oxides were
      being mixed, the powders were placed in a
      ball mill[12], along with distilled water
      and mixed for 24 hours. If less than 100
      g was involved, a mortar and pestle[13] was
      used to mix for 5 hours. Figure 24 shows
      the ball mill and mortar and pestle.

iv.   STEP 4: The mixture was dried on a hot
      plate for 10 hours at 200°C to remove any
      excess water.

---

[12] Norton Scientific Co., Canlab cat. no. C3700-1, C3750-4, C3775-1A

[13] Coors, cat. no. 60325 and 60326

v.   STEP 5:   The mixture was crushed for 2
hours by hand with a mortar and pestle.

vi. STEP 6: The powder was divided into 2.5 g
amounts and pressed at approximately 3.5
MPa into round discs.   These discs were
calcinated at 1000°C for 10 hours, in a
high temperature furnace (Figure 25)[14], to
remove any CO_2 from the mixture.   This
process is necessary in order to avoid the
formation of pores, due to the CO_2 gas,
during sintering. The purpose of pressing
the discs was to enhance diffusion between
the different oxides in the mixture, due
to its denser packing.

vii. STEP 7: The calcinated discs were crushed
by hand for 4 hours with a mortar and pes-
tle. A grain size as fine as possible was
desired because coarse grains reduce per-
mittivity by as much as 50% [33].   Also,
grain sizes smaller than 1 μm decrease the
dielectric constant rapidly. Therefore,
the best grain size is less than 1 μm.

---

[14] Lindberg furnace, model no.   51314-52314, and controller,
model no. 59246-82807t

viii. STEP 8:   5 wt.% of a high purity parafin
binder was disolved in chloroethene-VG[15] ,
a chlorine-based solvent. This liquid was
added to the powder and mixed in with a
mortar and pestle for 1/2 hour.   The mix-
ture was then heated at   100°C for 2 hours
to evaporate the chloroethene-VG, leaving
the parafin binder mixed in with the pow-
der.

ix.   STEP 9: The powder was separated into 3.0
g quantities and pressed for 1 minute at
approximately 3.5 MPa into discs.   Each
disc measured 25.4 mm in diameter and
approximately 2.0 mm in thickness.

x.   STEP 10: The discs were placed on an alu-
mina plate and sintered in the high temp-
erature furnace.   The following sintering
procedure was used:

1)   heat the discs at 400°C for 10 hours
to allow the parafin binder and any
moisture to evaporate out.

2)   increase the temperature to 700°C
for 1 hour.

---

[15] Dow Chemical Canada, cat. no. DC201-D776

3)   increase the temperature to 1000°C for 1 hour.

4)   increase the temperature 50°C/hour until the desired sintering temperature was attained (1275°C for B2TS2).

5)   hold for approximately 5 hours.

6)   cool the discs at a rate of 50°C/hour until 1000°C is reached and hold for 1 hour.

7)   decrease temperature to 700°C and hold for 1 hour.

8)   decrease temperature to 400°C and hold for 1 hour.

9)   decrease temperature to 0°C.

The optimum sintering temperature was determine by a differential thermal analysis (DTA) of the ceramic material.

4.2   Sputtering Target Preparation

Once the sputtering targets were fabricated, they were checked for flaws such as cracks, large pores, roughness, and warping.   Targets which contained any of these flaws were undesirable.   The desirable targets were then soldered with an electrically and thermally conductive silver epoxy[16]

---

[16] DYNALOY 336 A resin and 336 B hardener

to a copper target holder for maximum thermal and electrical
conduction and any excess epoxy was removed to minimize the
contamination of the thin film during sputtering. The tar-
get and holder were placed in a furnace for 1 hour at 125°C
to cure the glue. The target and holder were then cooled
and placed in the sputtering chamber for thin film fabrica-
tion. A round, aluminum confinement ring is placed over top
of the target and is adjusted to optimize the target-
electrode spacing. The inner ring hole diameter should be
less than 1.0 mm larger in diameter than the target diame-
ter. Clearance between the target and the insert ring
should be maintained around 0.5 mm and should not be touch-
ing underneath. A larger clearance gap will allow the plas-
ma gas to sputter the target holder and contaminate the
deposited film. Contact between the ring and target holder
will result in sputtering of the cover which will contami-
nate the film. A schematic illustration of the target area
and a top view of the target area can be seen in figures 3
and 26 respectively.

4.3 Substrate Preparation

Prior to sputtering, the substrates were cleaned and pre-
pared to allow for maximum adhesion and homogeneity between
the thin film and substrate. Highly polished (100) silicon

wafers approximately 0.5 mm in thickness, were cut into 12.5 mm x 12.5 mm or 25.4 mm x 25.4 mm sections, depending on the substrate holder, with a diamond tipped cutter. The substrates were then cleaned in an ultrasonic cleaner[17] with a 5% HF solution for 30 minutes to remove SiO_2 This process was then repeated with acetone for 30 minutes. The substrates were then washed off with distilled water and ethanol and blown dry. The substrates were placed in the desired substrate holder and immediately placed in the vacuum chamber as illustrated in Figure 3.

4.4 Operating Procedure of Sputter Deposition System

A detailed description of the operation procedure of the sputtering system is given.

1. START-UP PROCEDURE

    a. From Complete Shutdown

        i. Turn on the water supply to the diffusion pump by fully opening the water valve.

        ii. Close the 'Control Power' breaker.

        iii. Close the high vacuum valve.

        iv. Select 'Backing' on the combined Backing/Roughing (BRV) valve.

        v. Switch on the backing pump.

---

[17] Branson Cleaning Equipment Co., Bransonic 220, cat. no. 452B.

vi.   When the backing pressure reaches 100
       mTorr or less, turn on the diffusion pump.

vii.   The diffusion pump must warm up to oper-
       ating temperature.

2. PREPARATION_FOR_SPUTTERING

    a.   Hoist_Operation

          To raise the chamber lid, first make sure
    that the high vacuum valve is closed, the 3RV is
    at the 'Backing' position, and the chamber vent
    valve is open. Press the appropriate pushbut-
    ton. The lid may be swung away from the chamber
    by pulling the release ring at the back of the
    hoist head and pushing the lid.

          To close the lid, rotate the lid back to
    engage the release ring and press the appropri-
    ate pushbutton. As the lid nears the chamber,
    carefully guide it into the locating dowels in
    the top of the chamber.

    b.   Substrate_Loading

    i.   Always make sure the circuit breaker is
          off when working inside the chamber.

    ii.   Adjust the height of the substrate holder
          to the desired position

iii. Install the desired target into the source which will be powered.

iv. Close the lid as detailed above.

c. Chamber_Evacuation

i. Close the chamber vent valve and fully open the throttle value (variable orifice). Make sure that the 'pump ready' light is on.

ii. Select 'Roughing' on the BRV valve to rough down the chamber.

iii. When a system presure of 200 mTorr or better is reached, select 'Backing' on the BRV valve.

iv. Open the high vacuum valve slowly to avoid stalling the diffusion pump.

v. Evacuate the chamber to 10^{-6} Torr or less.

3. SPUTTERING_PROCEDURE

a. Throttle_valve_Operation

Repeatable diffustion pump throttling can be achieved with the micrometer stop. The valve can be fully opened or closed to the present condition by pressing the appropriate pushbutton.

b.   <u>Chamber Cooling</u>

If desired, open appropriate water valve for chamber cooling.

c.   <u>Sputtering Procedures</u>

   i.   <u>START-UP</u>:

     1)   Position substrate above covered target.

     2)   Fully open the water valve for target sources.

     3)   Select the appropriate argon valve and turn it counter-clockwise to open it.

     4)   Heat substrate to desired temperature.

     5)   Set Electron Emitter current, Plasma current knob to zero.

     6)   Turn on the 208V circuit breakers.

     7)   Turn on the PD/20 power supply by pressing the rocker switch upwards.

     8)   After 10-15 seconds, start turning the Electron Emitter Current knob until the plasma ignites, as indicated by a plasma reading of about 2 amperes.

9) Adjust the Electron Emitter Current knob clockwise until the plasma voltage drops from an open circuit voltage of about 85 volts to a reading of approximately 42 volts on the meter.

10) Slowly increase the Plasma Current while also adjusting the Electron Emitter Current to maintain the plasma voltage at about 42 volts.

11) If desired, open the oxygen valve.

12) Switch on the RF generator power supply circuit breaker and wait until the blue RF indicator is on.

13) Press the RF ON pushbutton.

14) Set the MULTIMETER function switch to the V3 IG position.

15) Turn the POWER control knob clockwise until the desired position is indicated on the Incident Power meter.

16) When ready for sputtering, open the shutter to allow the target atoms to reach the substrate.

17) When finished sputtering, re-cover the source with the shutter.

18) Reduce the substrate temperature.

ii.   **SHUTDOWN:**

1) Rotate the R.F. Power control knob fully counter-clockwise and switch off the generator circuit breaker.

2) Turn off the Electron Emitter Current and press the power rocker switch downwards.

3) Switch off the main 208V circuit breaker.

4) Turn off the water valve for the target source.

5) Close the high vacuum valve and check that the BRV valve is in the 'Backing' mode.

5) Open the air admittance valve.

d.   **Complete Shutdown Procedure**

If the system is not to be used for an extended period of time, then the system can be completely shut down.

1) Close the high vacuum valve and vent the chamber as above.

2)   Shut off the diffusion pump and allow it to cool, about 30 minutes.

3)   Switch the 3RV valve to the central position and quickly turn off the mechanical pump. The backing line will automatically vent.

4)   Close off all water and gas valves and shut off the control power at the panel.

Chapter V

RESULTS AND DISCUSSIONS

5.1 Ceramic Target Fabrication

Ceramic targets of $Ba_2TiSi_2O_8$ (B2TS2) were fabricated by
two methods: 1) following the procedure set out by a previ-
ous study [50] and shown in Appendix B and 2) following the
modified procedure set out in Section 4.1.

Sintered targets prepared by the first method (Figure 27)
were canary yellow in colour with greenish-blue agglomera-
tions appearing internally throughout the target. Attempts
to analyze these agglomerates proved fruitless because:

1.   the hardness of the ceramic target made fracture
      through one of the agglomerates near-impossible

2.   the area was lost, unless very carefully marked, when
      the sample was coated with carbon.

Most likely, the agglomerates are pores caused by a locali-
zation of voids, brought on by the heat, with a possible
colour enhancement due to contamination. The targets were
porous and cracked easily during the sintering and sputter-
ing processes. This was probably due to a nonuniformity in
the pressing procedure which in turn leads to nonuniform

thermal expansion during sintering and sputtering. Uneven distribution of the ceramic powder in the mold prior to pressing created higher densities in areas with more powder than areas with less powder. Thus fracture would occur due to localized stress between areas with different thermal expansion rates.

The sintered targets prepared by the second method (Figure 27) were tinted green in colour with no signs of agglomerations (or large pores) and appeared to be more smooth, less porous, and more compact.

Analysis of the ceramic targets was done to determine the optimum sintering temperature (DTA) and to measure the densities, composition (EDS) and phase relations (XRD) before and during sintering. Raman spectroscopy was also used to study the bonding states of the ceramics.

5.1.1 Differential Thermal Analysis

The optimum sintering temperature was determined from a Differential Thermal Analysis (DTA) obtained from a previous study [50] and is illustrated in Figure 28. This was the case because the departmental Harrop DTA was out of commission and attempts to obtain an analysis of this modified ceramic materials proved fruitless. The first reaction, occuring between 800-850°C is the calcination reaction of $BaCO_3$ (to remove the CO_2) during the reaction with the TiO_2

and the SiO_2, between 850-1000°, to form a variety of phases including 82TS2 (previously called 8STS). Between 1000-1240°C, the completion of the 82TS2 phase occurs due to the reaction of all the minor phases previously present. Finally, above 1300°C, the softening or partial melting of the ceramic begins. The optimum sintering temperature was determined to be 1275°C.

5.1.2   Ceramic Target Density

Density measurements were performed on both sets of discs and are tabulated in Table 5. From preliminary observations, the second set of targets appeared to be denser, however, when all the targets were measured, the discs fabricated using the previous study's method were found to be more dense. This could be attributed to the fact that this set of targets was pressed at a location external[19] to the University and an improper load (as much as 10 times higher than 3.5 MPa) may have been applied during pressing. This could also be the cause of the fracturing of the targets during the sintering and sputtering process, due to an enlarged nonuniform thermal expansion. The second set of targets were pressed in the Civil Engineering Department and the load (approximately 3.5 MPa) was carefully monitored so as not to be too high or low. No problems occured with

---

[19] GTE Valenite, Windsor, Ontario, Canada

these targets due to fracture during sintering or sputtering because the thermal expansion rate was relatively equal throughout the disc.

The thickness and diameter of the ceramic targets were measured over several areas and averaged out. The first set of discs had an average density of approximately 4.2 g/cm, or 94% of the theoretical density, as compared to the second modified set whose average density was approximately 3.3 g/cm, or 75% of the theoretical density. The theoretical density of B2TS2 is 4.45 g/cm [36]. However, the first set of targets had a volume decrease of approximately 39% after sintering as compared to the second set with approximately 26%. Thus small homogeneous voids prevent microcracks from growing and leading to fracture. It appears that the optimim sputtering target should have small grains and be moderately less dense (~25%) than the theoretical density of B2TS2.

5.1.3 Scanning Electron Microscope and Energy Dispersive Spectra Analysis

Scanning electron microscopy (SEM) micrographs of the two sets of sintered ceramic targets, provided in Figures 29 and 30, show quite a difference in structure. Targets fabricated using the previous method (Figure 29) show many small, rectangular-shaped grains on the disc surface and lesser

defined grains on the fracture surface. The second set of targets (Figure 30) have many small, rectangular-shaped grains on the fracture surface which are well sintered and well defined. The previous set of targets may have been affected by the previously mentioned increase in loading pressure. Evidence of melting is apparent indicating that the sintering temperature may be too high. There are also many pores throughout the target (which decrease the density).

Energy dispersive spectra (EDS) analysis of both sets of targets provided nearly identical patterns. Figures 31(a)-(f) show the actual spectra for both B2TS2 ceramic targets, using $BaTiO_3$ and silica gel as standards, along with the spectra of $BaCO_3$ and TiO_2. A superposition of $Si(K_\alpha)$ and $Si(K_\beta)$ peaks account for the peak positioned at 1.57 keV. The large peak occuring at 4.45 keV could be a combination of both Ba (4.47 keV) and Ti (4.50 keV). The next peak occuring approximately at 4.35 keV again could be a combination of Ba (4.83 keV) and Ti (4.33 keV). The last peak occuring around 5.16 keV is a product of Ba. Due to the severity of the Ba and Ti energy spectra overlap in the second and third peaks (shown in Figures 31(d)-(f)), it is not possible to positively identify the ceramic material as B2TS2, although all indications point to this. Thus, it is assumed to be B2TS2.

With the results obtained from the EDS analysis, a method was established to determine the weight and atomic percentages of each element in the ceramic target. Windows (or ranges) were set up for each of the peaks and their respective background interference (Table 6) and the integral values were calculated. These values were placed into a computer program which calculated the compositions. The results of two modified B2TS2 ceramic targets and the powder can be seen in Table 7. Again, due to the severity of the Ba and Ti energy spectra overlap and the estimation of the integrated areas of the peaks, an accurate quantitative analysis is very difficult to obtain.

5.1.4 X-Ray Diffraction

X-ray diffraction (XRD) patterns were obtained for both sets of ceramic targets and can be seen in Figures 32 and 33, respectively. Analysis and identification of each peak was performed and tabulated in Table 6. Identification was carried out using the JCPDS file cards listed in Table 3. Both sets of discs are nearly identical to the diffraction pattern of B2TS2. However, the ceramic targets fabricated using the previous procedure showed some additional weak peaks. Extra weak peaks at $2\theta=31.4°$ and $38.7°$ were attributed to $BaTiO_3$, at $2\theta=25.8°$, $30.2°$, and $65.2°$ to $BaSi_2O_5$, and at $2\theta=25.3°$ and $65.2°$ to $BaSiO_3$. This is an indication that full equilibrium of the material was not established.

The second set of targets showed no peaks other than for B2TS2 meaning a full equilibrium was obtained.

Thus, it was concluded that the modified procedure for B2TS2 ceramic target fabrication (Section 4.1) was the better method to use to obtain a crystalline B2TS2 target for sputtering.

5.1.5 Phase Analysis During Sintering

The phase relations of the B2TS2 compound occuring during the sintering process were studied.   100 grams of a ceramic powder with ratios Ba:Ti:Si equal to 2:1:2 was produced following steps 1-5 in Section 4.1. The powder was then heated for a minimum of 48 hours at temperatures varying from room temperature to 1300°C.   After each heating period, the powder was removed from the furnace, mixed and crushed for 1/2 hour, a small amount (~10 grams) removed, the remaining powder placed back in the furnace, and heated up to the next temperature level.   Each tempered powder was then subjected to XRD using $Cu(K_\alpha)$ radiation. The diffraction patterns were analyzed using the JCPDS data cards for all the possible phases present.   The JCPDS cards used in the analysis are listed in Table 3.

Figure 14 shows the XRD patterns of the ceramic powder mixture heated at the indicated temperatures.   The as-mixed powder shows peaks only from $BaCO_3$ and TiO_2 but not from

The second set of targets showed no peaks other than for B2TS2 meaning a full equilibrium was obtained.

Thus, it was concluded that the modified procedure for B2TS2 ceramic target fabrication (Section 4.1) was the better method to use to obtain a crystalline B2TS2 target for sputtering.

5.1.5   Phase_Analysis_During_Sintering

The phase relations of the B2TS2 compound occuring during the sintering process were studied.   100 grams of a ceramic powder with ratios Ba:Ti:Si equal to 2:1:2 was produced following steps 1-5 in Section 4.1.   The powder was then heated for a minimum of 48 hours at temperatures varying from room temperature to 1300°C.   After each heating period, the powder was removed from the furnace, mixed and crushed for 1/2 hour, a small amount (~10 grams) removed, the remaining powder placed back in the furnace, and heated up to the next temperature level.   Each tempered powder was then subjected to XRD using $Cu(K_\alpha)$ radiation.   The diffraction patterns were analyzed using the JCPDS data cards for all the possible phases present.   The JCPDS cards used in the analysis are listed in Table 3.

Figure 34 shows the XRD patterns of the ceramic powder mixture heated at the indicated temperatures.   The as-mixed powder shows peaks only from $BaCO_3$ and TiO_2 but not from

SiO_2, as the SiO_2 was in the form of amophous silica gel. At 850°C, the calcination of $BaCO_3$ appears to have been completed (confirming the DTA results) and the chemical reactions have begun with the formation of $BaTiO_3$ (henceforth BT3), $BaSiO_3$ (BS3), Ba_2SiO_4 (BS4), and possibly even a small amount of $BaSi_2O_5$ (BS5). In order to satisfy the law of mass conservation, SiO_2 must also coexist. The compound B2TS2 also begins to appear and may be the result of reactions of BT3 with BS3, BS4 or SiO_2. At 1000°C, all the previous phases still exist (with the possible exception of BS5), however, B2TS2 begins to appear as the predominant phase. At 1250°C and 1300°C, B2TS2 is the only phase which exists, with the possible exception of amorphous SiO_2, indicating that the ceramic material is in equilibrium at these temperatures.

The composition of this material determined by EDS analysis, using BT3 and silica gel as standards, is given in Table 9. This composition was near stoichiometric B2TS2. However, previous studies had found that B2TS2 ceramic targets fabricated in the same manner had less than the stoichiometric amount of Si, while the Ba:Ti ratio was unaltered, when analyzed by wavelength dispersive x-ray analysis. Experimental error of ±2.0 at.% made it impossible to verify if a decrease in the stoichiometric amount of

SiO_2 had occured in the ceramic powder. Errors in the SiO_2 content may be due to the absorptive character of silica gel, creating a problem during the initial heating and weighing of the powder, in spite of the special precautions taken in this procedure.

Thus, an oxide powder mixture with the Ba:Ti:Si ratios of 2:1:2 formed B2TS2 in an equilibrium state above 1250°C and an EDS analysis of the material indicated near-stoichiometry.

5.1.6   Raman Spectroscopy

The atomic bonding states of various standard materials along with a B2TS2 just-mixed powder, a sintered powder, and a sintered sputtering target were analyzed by Raman spectroscopy in the Department of Chemistry, University of Windsor. A laser beam producing a wavelength of 514.5 nm was used as the incident beam. The standard bulk powders of $BaCO_3$, TiO_2 (anatase), and silica gel were the same powders used to fabricate the ceramic sputtering targets. An x-ray analysis of all the standards was used to confirm their structures prior to Raman analysis. Figures 35(a)-(g) show the Raman spectroscopy results of the standard and B2TS2 ceramic materials, plotting the scattering intensity (I) against the wave number (Nw). Each specimen possesses specific peaks.

The lower wave numbered peaks which occur for $BaCO_3$ (Figure 35(a)) are due to lattice modes external to the material. Any carbonate peaks will occur above $Nw=800 cm^{-1}$ [34].

The only powder which produced any significant peaks was TiO_2 (anatase) in Figure 35(b). These peaks are in good agreement with a previous study performed on TiO_2 [35].

Figure 35(d) shows a powder just mixed in the Ba:Ti:Si ratios of 2:1:2. The only peaks which appear belong to the TiO_2 spectrum which has very strong phonon transitions. An x-ray analysis of the mixture (Figure 34(a)) did confirm the presence of $BaCO_3$ but not SiO_2, since it was amorphous.

After heating the powder mixture at 1300°C for 114 hours, a different vibrational transition pattern appeared (Figure 35(f)), which must correspond to B2TS2 since x-ray analysis of the material (Figure 34(e)) confirmed it to be B2TS2.

Raman analysis of a B2TS2 sputtering target (Figure 35(g)) provided an identical spectrum to that of the heated powder. These peaks were more distinct, although they were not as intense. This is believed to be the first Raman spectrum analysis of B2TS2 and thus no comparisons can be made.

5.2   Fabrication_of_B2TS2_Thin_Films

The foremost objective of this study was to obtain c-axis oriented thin films of B2TS2.   Previous studies [50,51] have observed slight indications of c-axis orientation for B2TS2 thin films heated, in-situ, at 650°C although no c-axis oriented thin films were obtained.   As previously stated, c-axis or (00n)   oriented B2TS2 thin..films are required to obtain a piezoelectric thin film.   Attempts to fabricate thin films above 650°C were hindered due to the limitations of the ceramic substrate heater used.   However, this problem was solved with the design of the Tantalum wire heater (Section 3.2).   Therefore, using B2TS2 ceramic targets fabricated following the procedure outlined in Section 4.1, thin films were deposited at temperatures, in-situ, above 650°C in an r.f. triode sputter deposition unit located in the Department of Engineering Materials, University of Windsor. The operating conditions for the sputter depositing of the thin films are listed in Table 10.

In order to enhance the possibility of obtaining c-axis oriented thin films, (100)Si wafers were used as the substrate material for the following reasons:

1.   (100)Si has a high melting point, compared to other substrate materials (i.e. glass, NaCl), which is needed to withstand the high substrate temperatures required to deposit c-axis oriented thin films

2. the lattice parameters of Si and B2TS2 in the (001) plane are 0.545 nm and 0.852 nm respectively. Thus, three units cells of Si, side by side, are almost the same length (~96%) as two unit cells of B2TS2, side by side (Figure 36). This near lattice matching makes possible the creation of an epitaxial-like effect between the (100)Si substrate and the (001) B2TS2 thin films.

3. the thermal expansion rate of Si is smaller than that of B2TS2 and the thin film would be under tension when cooled and would remain continuous rather than cracked and exfoliated like thin films deposited on NaCl, which has a higher thermal expansion rate [48,50,52].

Thin films were deposited at 650°C to verify the results from previous studies and to set a lower limit for the range of testing. An upper limit for the testing range was chosen at 800°C, due mainly to the fact that this was the maximum temperature attainable with the tantalum-wire heater. X-ray diffraction patterns and optical micrographs were used to analyze each thin film.

The amorphous structure of B2TS2 thin films deposited at 650°C on (100)Si was verified from the x-ray diffraction pattern in Figure 37. Two weak broad peaks occuring between 2θ 20° and 30° indicate an amorphous structure, which also

corresponds to the findings of a previous study performed on B2TS2 thin films using electron diffraction [52]. The previous study also found small amounts of crystalline B2TS2 present in the thin films. however, no such indications were found in the thin films fabricated in this study. The two peaks occuring at approximately $2\theta = 69.0°$ and $33.0°$ are attributed to the (100)Si substrate. The lower angled peak can be eliminated by reducing the power level of the monochromatic x-ray but this will also decrease the intensities of all the other peaks involved in the analysis. Besides, the lower angled peak can be used as a reference peak, when trying to determine the relative degree of orientation at various temperatures, since the Si substrate peak should remain constant in relative intensity. The thin film (Figure 38) appears to be a smooth, continuous layer (dark area) with small crystallite formations (light coloured islands) dispersed throughout the film. These formations would seem to confirm the previous study's results of crystalline B2TS2 found in electron diffraction pattern of the thin films. The dark area was determined to be the amorphous region since it occupied most of the area of this near-amorphous structure and because it is very similar in colour and texture to an amorphous film deposited at a temperature below 200°C for 24 hours (Figure 39).

At 300°C, the X-ray diffraction pattern of the B2TS2 thin film (Figure 40) portrays a polycrystalline structure. All the peaks which occur in this pattern correspond to the most intense peaks of crystalline B2TS2, with the exception of the (400)Si peaks discussed previously. These peaks most likely occur due to the thinness of the films. The monochromatic x-rays beams penetrates through the film and into the Si substrate before reflecting back. Another possibility is reflection from the area surrounding the thin films which is not coated. Figure 41 shows a random mosaic pattern of minute grains for the thin film, which is indicative of a polycrystalline material. The differently shaded grains are due to light reflecting off the surface of the randomly oriented grains.

Since the oriented structure occurs between the amorphous and polycrystalline morphologies, c-axis oriented B2TS2 thin films are produced, for in-situ heating, somewhere between 650°C and 800°C. To further narrow down this region, B2TS2 thin films were sputter deposited at 25°C intervals beginning at 675°C, for anywhere between 6 and 8 hours. The structure of each thin film was determined by analyzing their x-ray diffraction patterns and optical micrographs. The composition of the B2TS2 thin films were measured using EDS. Raman spectroscropy was used to identify phases included in the thin films.

Film thickness measurements were also performed on each of these thin films. Table 11 lists the thermal conditions of each thin film analyzed in this study.

5.2.1 \X-Ray Diffraction

The XRD patterns of the thin films fabricated at substrate temperatures, in-situ, between 675° and 775° are shown in Figures 42(a)- (e). With the help of Mr. Li Yi, the inverse pole figures of various samples were determined (Figures 43(a)-(f)) using Harris' method [78]. Figure 43(a) shows the stereo-projection figure of the diffracted crystal planes listed in the JCPDS file for B2TS2 (card no. 22-513). A randomly- oriented XRD spectrum of a 32TS2 thin film,used for a reference standard, was obtained from a thin film sputter deposited at 430°C and annealed at 725°C for 10 hours by R. J. White et al.[51]

Sample 2, deposited at 675°C for 6 hours, still possesses an amorphous structure (Figure 42(a)) but with a lower degree of intensity than sample 1 (650°C). Only the lower angled halo located between 2θ = 20.0° and 23.0° can be seen. The peaks belonging to (400) Si still appear.

Sample 3, deposited at 700°C for 6 hours, shows peaks (in Figure 42(b)) at approximately 17.1°, 34.5° and faintly at 52.7° which correspond to the (00n) planes, where n=1,2,3, respectively. These are the peaks required for c-axis ori-

entation. The amorphous halo at around 22.0° still exists, along with the peaks related to (400) Si. These peaks are not as intense, indicating the predominating effect of the oriented thin film. The inverse pole figure for the B2TS2 thin film is shown in Figure 43(b). From the diagram, the pole density at (001) was determined to be 7.60 with a slight concentration of the contour lines. There are no other peaks appearing which implies that the optimum temperature for sputtering preferentially oriented thin films is close at hand.

Figure 42(c), which represents sample 4 deposited at 725°C for 7 hours, has the oriented peaks growing in intensity, compared to the other peaks, and shows the likelihood that this thin film was fabricated using close to the ideal parameters for c-axis orientation. However, the amorphous halo still exists which means the film is not fully crystalline. The peak occuring at 36.2° is most likely due to contamination. The inverse pole figure of this thin film, illustrated in Figure 43(c), shows that the (001) pole density has grown to 13.35 and the contour lines have become even more concentrated. Again, no other non-(00n) oriented planes appear and upon comparison with the previous results from 700°C, this temperature appears to be more favourable for preferentially-oriented thin films.

At 750°C, the (400)Si peak occuring at 33.0° is filtered out while the (00n) peaks still predominate and grow in size (Figure 42(d)). However, a polycrystalline mophology begins to transform with identifiable peaks occuring at 21.6°, 27.0°, 29.0°, 41.8°, 48.5°, and 58.4°, which correspond to the most intense peaks of 32TS2. This increased temperature has lowered the pole density of (001) to 9.56 and has introduced the pole densities of several non-(00n) oriented peaks (Figure 43(d)). This suggests a shift away from a preferentially oriented thin film. Again this temperature has concentrated the contour lines even more towards (001).

The thin film deposited at 775°C for 8 hours, shown in Figure 42(e), has the non-(00n) peaks growing rapidly in intensity, compared to the (00n) peaks, while the (400)Si substrate peak at 69.0° is still decreasing in intensity. More peaks are beginning to appear which indicates a transformation towards a polycrystalline morphology from a c-axis oriented one appears imminent. The inverse pole figure, shown in Figure 43(e), has a decrease in the pole density of the (001) peak to 3.92 while the pole density increases for the non-(001) peaks surrounding the (001) point.

Figure 43(f) shows, at 800°C, the pole density of the (001) direction decreasing further to 0.30, while many other planes have an increase in density. Thus, this temperature

is too high for the fabrication of c-axis oriented B2TS2 thin films and is proven by the polycrystalline structure of the B2TS2 thin film deposited at 300°C as previously mentioned.

5.2.2 Optical Microscopy

Each of the thin films listed in Table 11 were observed under an optical microscope at approximately 400 times magnification. As previously mentioned, the thin film deposited at 650°C was mostly amorphous (dark area) with islands of crystallites beginning to form (Figure 33).

The thin film deposited at 675°C shows (in Figure 44) that the crystallite islands have grown in size but the amorphous structure still predominates. It is possible that these islands are amorphous (the darker ones) and are in the process of transforming to a crystalline morphology.

At 700°C, the thin film structure appears to have completely transformed into a crystalline structure with the large grains coalescing (Figure 45). The formation of smaller grains appears to be taking place.

The thin film at 725°C shows a very distinct, almost circular, small grain pattern (Figure 45). This is probably what is necessary to obtain a c-axis oriented thin film and correlates with the (00n) oriented findings of the x-ray diffraction pattern of this film. The large white pits or

volcanoes (cannot be distinguished on the optical micro-
scope) which appear could be either due to fracturing of the
film during cooling or contaminants deposited on the film.

Large grains reappear at 750°C (Figure 47) with the
smaller grains dispersed between the grain boundaries.
These larger grains are polycrystalline and are responsible
for the non-(00n) peaks appearing in the x-ray diffraction
pattern. These grains also enhance the (00n) peaks because
these planes are part of the polycrystalline morphology.

At 775°C, Figure 48 shows the large grains transforming
into a smaller randomly oriented grain pattern. This is in
step with the x-ray diffraction pattern showing the poly-
crystalline morphology taking over.

At 800°C, as previously mentioned, the thin film is a
continuous layer of small randomly oriented crystalline
grains (Figure 41).

5.2.3   Fabrication_of_c-axis_Oriented_B2TS2_Thin_Films

From the above results, it is obvious that thin films
deposited in the range of 700°to 725°C, approximately, gives
the best results for the fabrication of c-axis oriented
B2TS2 thin films. Hence, thin films were fabricated at
700°C and 725°C for extended periods of time with the inten-
tion of obtaining thicker more highly (00n) oriented films
while removing the effects of the amorphous and (400)Si
structure.

A B2TS2 thin film was deposited at 700°C for 8 hours. The x-ray diffraction pattern (Figure 49) showed signs of a polycrystalline structure beginning to form. The surface of the thin film (Figure 50) showed many large, light-coloured grains forming and regions (dark areas) of smaller grains either coalescing to form large grains or vice versa. The x-ray diffraction pattern would indicate a transformation to the large polycrystalline grains due to the appearance of the non-(00n) peaks.

The same results were obtained, but with more peaks involved, for a B2TS2 thin film deposited at 725°C for 13 hours (Figure 51). Figure 52 of the thin film surface appears to have larger grains beginning to form at the expense of the oriented grains. There is also the possibility that the larger grains are forming on top of the oriented layer and slowly filtering it out. The thickness of the film was determined to be between 400.0 nm and 500.0 nm.

Due to the greater intensity of the (00n) peaks at 725°C compared to 700°C, the ideal fabrication temperature for c-axis oriented B2TS2 thin films is closer to 725°C. Thus, 725°C was chosen for the fabrication of thin films. However, thin film fabrication at a constant temperature is not suitable for obtaining a highly oriented film, as indicated above. Private communications with H. Yamauchi suggested,

decreasing the temperature after a set time to preserve the orientation. Therefore, the next step was to determine the length of sputtering time at 725°C and the amount of the temperature decrease.

A B2TS thin film deposited at 725°C for 2 hours indicated a very slight peak at $2\theta = 34.3°((002))$ in Figure 53, but due to the shortness of the deposition time, the oriented film was not thick enough to assert its epitaxial effect. A film deposited at 725°C for 3.5 hours gave a very strong display of epitaxial-like orientation (Figure 54) and observations of the surface (Figure 55) show the initial stages of c-axis oriented grains. The larger grains, which appeared at the lower temperature are almost completely transformed into smaller (00n) oriented grains which are beginning to fuse into the slightly larger oriented grains. At 5.5 hours, the thin films deposited at 725°C begins the coalescing of its smaller oriented grains into the larger grains which form between the crystalline and polycrystalline morphology of this material (Figure 56). The XRD pattern of this thin film, illustrated in Figure 57, confirms that the transition to a polycrystalline structure has begun, with the (211) peak and other less intense peaks appearing.

By process of elimination the time at which a temperature variation should be applied is within a range around 3.5 hours. Since the XRD pattern for the thin film sputtered for 3.5 hours still had signs of the amorphous halo at 22.0°, it was decided to sputter for a longer period of time in the hope of removing this morphology prior to the temperature variation. Thus, the B2TS2 thin films were sputter deposited at 725°C for 4 hours before the temperature was decreased slightly to increase the likelihood of obtaining a highly oriented film.

Initially, the substrate temperature was decreased by 25°C to 700°C after 4 hours where it remained for another 6 hours. XRD data indicated (in Figure 58) that this temperature drop was not enough, as a polycrystalline morphology still existed. Surface observations produced a variety of structures consisting mainly of the smaller oriented grains along with the larger polycrystalline grains (Figures 59(a) and (b)). Next the substrate was subjected to a 50°C decrease in temperature after 4 hours and this again resulted in a polycrystalline thin film (Figure 60). However, the intensity of the non-(00n) peaks was far less for this temperature decrease than reported for the previous decrease. Surface observations (Figure 61) portrayed a very complex deposition pattern, although the feature which is of most

interest is the "speckles" of the oriented small grains. A further decrease in temperature will be required. although not as drastic (~10°C), to obtain a highly oriented B2TS2 thin film.

5.2.4 Film_Thickness_Measurements

The B2TS2 thin films sputter deposited on (100)Si at the various temperatures were measured for thickness. The thin films produced were smooth and continuous which is good for measuring, however, there were some fluctuations in the thickness. This is due to the varying distances between the target and different points on the substrate surface. Usually, the centre of the film is the thickest, because it has the shortest target-to-substrate distance, and the thickness decreases as the edge of the film is approached. Thus, the thin film thickness was measured at various points around the film edges and an average range was taken. Also, because of the low reflectivity of B2TS2 thin films, the films had to be coated with aluminum prior to measuring. The results of various thin films are listed in Table 11.

The average thickness is between 100 nm and 200 nm (0.1-0.2 μm), for thin films sputter deposited between 5 and 3 hours, which is far less than the desired 10.0 μm required for the proper study of the electronic properties of the thin films. Much thicker films were obtained for B2TS2

sputtered at 725°C for 13 hours (0.35-0.55 pm) and a thin film sputtered at less than 200°C for 24 hours (0.70-0.35 μm). Due to the short lifetime of the tantalum-wire heater and sputtering source filament along with the fragility of the B2TS2 sputtering target, the fabrication of thicker films will not be attainable until a solution to these problems is found.

5.2.5 Energy Dispersive Spectrometry

An energy dispersive spectra (EDS) analysis of the B2TS2 thin films revealed a pattern almost identical to the ceramic material although not as intense (Figure 62). Again the spectra determined using $BaTiO_3$ and silica gel as the standards. $Si(K_\alpha)$ and $Si(K_\beta)$ account for the peaks appearing at 1.67 keV, while the peaks occuring at 4.45 keV and 4.85 keV are a combination of both Ba and Ti peaks, much like before. The last peak, which occured at 5.16 keV (Ba) in the B2TS2 ceramic, is almost negligible here and is lost in the background interference.

The weight and atomic percentages were determined for B2TS2 thin films deposited at 200°C for 24 hours and is listed in Table 7. Due to severe energy spectra overlap of Ba and Ti peaks and also interference from the Si substrate, an accurate qualitative analysis is very difficult to obtain. Even so, the off-stoichiometric thin film still

consisted primarily of B2TS2, along with another unknown phase (in a minor amount) to satisfy the law of mass conservation.

5.2.6 Raman Spectroscopy

The atomic bonding states of the (100)Si substrate and several B2TS2 thin films, fabricated at various temperatures, were studied by Raman spectroscropy in the Department of Chemistry, University of Windsor. In all cases, a laser beam producing a wavelength of 514.5 nm was used as the incident beam. The bulk samples of $BaCO_3$, TiO_2 and SiO_2 analyzed previously for the ceramic target standards were used again along with the results of the B2TS2 ceramic target. The thin films were initially analyzed by x-ray diffractometry to confirm that samples with an amorphous, crystalline (preferentially oriented) and polycrystalline morphology were each analyzed. The results of this analysis are shown in Figures 63(a)-(d) and plot the scattering intensity (I) versus the wave number (Nw).

The Raman analysis of the (100)Si substrate (Figure 63(a)) produced a very distinct peak at $Nw=520$ cm^{-1}, which is a characteristic peak of crystalline Si [86].

The results of the Raman spectroscopy analysis for all the B2TS2 thin films (Figure 63(b)-(d)) gave no indication of any phase existence, through bond frequencies. The only

peak which was obtained was the same peak produced for the
(100)Si substrate spectra. The possible reasons why no
peaks appeared include:

1. the phase(s) present in the B2TS2 thin film may not be
   Raman active.

2. the dynamic range of the photon detector is limited
   which leads to problems when measuring weak peaks on
   intense background (ie. Si).

3. the B2TS2 ceramic, being randomly oriented, produces a
   spectra no matter what angle the incident laser beam
   hits the sample at. However, the thin films have a
   layered structure, when deposited, and do not allow
   the incident beam to penetrate. Thus the bonds cannot
   be reached to be excited.

4. although the thin films show signs of crystallinity,
   when analyzed by x-ray diffraction, some portion of
   the film remains amorphous and thus the atomic posi-
   tions of the totally disordered region filters out the
   bond vibrations of the crystalline region.

   If situation (1) or (2) are the problem, the samples
should be analyzed by infrared (IR) spectroscopy, since it
is analogous to, but not identical with Raman spectroscopy.
Situation (3) can possibly be solved by angling the thin
films (~60°) which may allow the incident laser beam to pen-
etrate and determine the bond frequency spectra.

Chapter VI

SUMMARY

6.1 B2TS2 Ceramic Targets

1. Ceramic targets were fabricated by two different meth-
ods for the r.f. sputter deposition of B2TS2 thin
films. The second method (Section 4.1) produced a
better quality (smaller grained, modererately porous)
target which did not fracture during the sintering or
sputtering process. This is probably due to a more
uniform pressing procedure.

2. The optimum sintering temperature was previously
determined to be 1275°C. However, indications of
melting are apparent in the target suggesting that
this temperature is too high. 1250°C may be good
enough.

3. An x-ray diffraction analysis of B2TS2 targets pro-
duced by the first method (Appendix B) showed the
B2TS2 phase coexisting with $BaTiO_3$, Ba_2SiO_4, and
$BaSiO_3$. This non-equilibrium could be due to an off-
stoichiometric mixture of $BaCO_3$, TiO_2 and silica gel
or to the mixture not being properly mixed long
enough. An x-ray diffraction analysis of the targets

- 78 -

produced by the modified procedure showed a full equilibrium of B2TS2 was obtained.

4. A phase analysis during sintering was performed on the B2TS2 ceramic. At 350°C, the calcination of BaCO° appeared to be completed and a variety of phases coexisted in this non-equilibrated state. At 1000°C, B2TS2 begins to appear and coexists with all the phases present at 350°C. Above 1250°C, the B2TS2 material is in equilibrium, with the existence of only the single phase. EDS analysis of this material indicated near-stoichiometry.

5. EDS anaylsis of the modified ceramic powder and targets provided a spectrum which is assumed to be B2TS2, due to a severe overlap of Ba and Ti energy peaks. From this spectrum, a correction factor was derived and applied to determine the relative amounts of Ba, Ti, Si, and O in the composition of the targets.

6. The atomic bonding states of B2TS2 were analyzed by Raman Spectroscopy.

6.2 B2TS2 Thin Films

1. Thin films of B2TS2 were fabricated by means of r.f. triode sputtering on (100)Si substrates.

2.   The substrate temperature was varied between 650°C and
     800°C, at 25°C intervals, to determine the optimum
     temperature range for (00n) oriented thin films. The
     amorphous-to-oriented transition temperature occurred
     betweeen 675°C and -700°C while the oriented-to-
     randomly oriented transition temperature begins in the
     range of 750°C to 800°C. X-ray diffraction analysis
     and inverse pole figures indicated a more preferred
     orientation in the range of 700 to 750°C for thin film
     deposition, although the highest pole density for the
     (001) peak was obtained around 725°C.

3.   Longer sputtering times in the crystalline (preferred
     orientation) range produced polycrystalline thin
     films. Thus, a temperature drop must occur during
     sputtering to maintain a preferrentially oriented thin
     film. Analysis of various sputtering times at 725°C
     suggested a temperature drop at approximately 4 hours
     after sputtering commences.

4.   Temperature drops of 25°C and 50°C after 4 hours of
     sputtering still produced a polycrystalline thin film,
     although the preferred orientation ((00n)) was more
     predominant after the latter experimental drop. Thus
     a further decrease is required, but not as much, to
     produce a preferrentially oriented thin film.

5.   Thin films of between 0.1 and 0.2 μm thickness were
      produced after sputtering for between 6 and 8 hours.
      This is far less than the necessary 10.0 μm needed for
      the study . of the electronic properties.   Sputtering
      times of greater than 24 hours will be required to
      produce films thick enough for proper measuring.

6.   With the fragility of the B2TS2 targets no longer a
      problem, the short lifetime of the Ta wire heater and
      sputtering source filament, at high temperatures, will
      have to be solved before thicker films will be attai-
      nable.

7.   EDS analysis of the B2TS2 thin films provided a spec-
      tra identical to that   of the ceramic material,
      although not as intense.   This could be due to the
      secondary effects of the x-rays not being a factor, as
      they are in the ceramics,   because of the thin layers
      being analyzed.   Although   the thin film was off-
      stoichiometric, B2TS2 was still produced along with a
      very minimal amount of another phase, which has no
      effect on the oriented thin film.

8.   Raman Spectroscopy analysis of the B2TS2 thin film
      gave no indications of any bond states being produced.
      This is most likely due to the phases present in the
      thin film not being Raman active.

Chapter VII

CONCLUSIONS

1. A single phase B2TS2 ceramic target was successfully fabricated for r.f. sputter deposition. A smaller grained, moderately less porous target is better suited and more durable for the thermal conditions characteristic to sputtering.

2. A phase analysis during sintering indicated that the B2TS2 target was in a fully equillibrated state above 1250°C.

3. The atomic bonding states of B2TS2 were analysed by Raman Spectroscopy for what is believed to be the first time.

4. Smooth, continuous thin films of Ba-Si-Ti-O, in a preferentially oriented ((00n)) state were produced by r.f. triode sputtering in the range of 700-750° although the best results, as determined by x-ray diffraction and inverse pole figures were obtained at approximately 725°C.

5. Variations in the sputtering time at 725°C suggest that a temperature drop of slightly larger than 50°C

must occur approximately 4 hours after sputtering is initiated to maintain a preferred orientation.

6. A sputtering time of greater than 24 hours is required to obtain a film thick enough for electronic studies.

7. EDS analysis of the thin films produced a spectra almost identical to the ceramic target. Compositional analysis showed an off-stoichiometric thin film consisting of B2TS2 along with a minimal amount of an unknown phase which had no effect on the orientation effect of the film.

3. Raman Spectroscopy analysis of the films showed no energy spectra for the atomic bonding states of the phase(s) present and should be looked at in more detail.

Chapter VIII

RECOMMENDATIONS FOR FUTURE RESEARCH

1. Further research is required to fabricate a B2TS2 thin films with a preferential orientation, for longer periods of time (>24 hours) in order to get the thicker films required for electronic studies.

2. Modifications to the Ta-Wire heater are required to prolong the deposition time. Kanthal wire as a possible replacement of Ta should be studied because of its higher wear resistance in oxide atmospheres.

3. Modifications to the Ta sputtering source filament are required to prolong the deposition time. Thus, positively charged ions must be prohibited from sputtering the filament. This can be attained by reducing the applied voltage between the filament and the anode while increasing the filament current so as not to reduce the plasma generating efficiency.

4. The sputtering of metallic targets should be looked at more closely because of their larger sputtering rate, compared to ceramic targets.

5. TEM analysis of B2TS2 thin films deposited on (001)Si and fused quartz is recommended to study the structure.

6. The atomic bonding states of the B2TS2 thin films should be studied further by Raman Spectroscopy to determine their characteristic vibrational spectrum.

REFERENCES

1. N. F. Foster, "Ultra-High Frequency Cadmium-Sulphide Transducers", IEEE Trans. Sonics and Ultrason., SU-11, 63-68 (1964)

2. N. F. Foster and G. A. Rozgonyi, "Zinc Oxide Film Transducers", Appl. Phys. Lett., 8 (9), 221-223 (1966)

3. N. F. Foster, G. A. Coquin, G.A. Rozgonyi and F.A. Vannatta, "Cadmium Sulphide and Zinc Oxide Thin Film Transducers", IEEE Trans. Sonics and Ultrason., Su-15, 28-40 (1968)

4. N. F. Foster, "Crystallographic Orientation of Zinc Oxide Films Deposited by Triode Sputtering", J. Appl. Phys., 40 (1), 111-114 (1969)

5. F. S. Hickernell, "dc Triode Sputtered Zinc Oxide Surface Elastic Wave Transducers", J. Appl. Phys., 44 (3), 1061-1071 (1973)

6. F. S. Hickernell, "MIcrostructure of ZnO Films used for Acoustic Surface-Wave Generation", J. Vac. Sci. Technol., 12 (4), 879-883 (1975)

7. T. Mitsuyu, S. Ono, and K. Wasa, "Structures and SAW properties of rf-Sputtered Singe-Crystal Films of ZnO on Sapphire", J. Appl. Phys., 51 (5), 2464-2470 (1980)

8. T. Yamamoto, T. Shiosaki and A. Kawabata, "Characteri-
    zation of ZnO Piezoelectric Films Prepared by rf
    Planar- Magnetron Sputtering", J. Appl. Phys., 51 (6),
    3113-3120 (1980)

9. T. Hata, E. Noda, O. Morimoto and T. Hada, "High Rate
    Deposition of Thick Piezoelectric ZnO Films Using a New
    Magnetron Sputtering Techinique", Appl. Phys. Lett., 37
    (7), 633-635 (1980)

10. T. Shiosaki, T. Yamamoto, M. Yagi and A. Kawabata,
    "Plasma-Enhanced Metalorganic Chemical Vapour Deposi-
    tion of c-Axis Oriented and Epitaxial Films of ZnO at
    Low Substrate Temperatures", Appl. Phys. Lett., 39
    (5), 399-401 (1981)

11. T. Shiosaki and A. Kawabata, "Piezoelectric Thin Films
    for SAW Applications", Ferroelectrics, 42, 219-232
    (1982)

12. T. Mitsuyu, O. Yamazaki, K. Ohji and K. Wasa, "Piezoe-
    lectric Thin Films of Zinc Oxide for SAW Devices", Fer-
    roelectrics, 42, 233-240 (1982)

13. J. S. Wang and K. M Lakin, "c-Axis Inclined ZnO Piezoe-
    lectric Shear Wave Films", Appl. Phys. Lett., 42 (4),
    352-354 (1983)

14. F. Takeda, T. Shiosaki, and A. Kawabata, "High Coupling
    and High Velocity Surface Acoustic Waves Using c-Axis

Oriented ZnO Films on Translucent Al_2O_3 Ceramics", Appl Phys. Lett., 43 (1), 51-53 (1983)

15. K. Kushida and H. Takeuchi, "Crystalline Properties of rf-Sputtered ZnO Film on Gold Film on Fused Quartz", J. Appl. Phys., 56 (4), 1133-1135 (1984)

16. M. T. Wauk and D. K. Winslow, "Vacuum Deposition of AlN Acoustic Transducers", Appl. Phy. Lett., 13 (8), 286-288 (1968)

17. A. J. Shuskus, T. M. Reeder and E. L. Paradis "rf-Sputtered Aluminum Nitride Films On Sapphire", Appl. Phys. Lett. 24 (4) 155-156 (1974)

18. T. Shiosaki, T. Yamamoto, T. Oda and A. Kawabata, "Low Temperature Growth of Piezoelectric AlN Film by rf Reactive Planar Magnetron Sputtering", Appl. Phys. Lett., 36 (8), 643-645 (1980)

19. S. Onishi, M. Eschwei, S. Bielaczy and W. C. Wang, "Colorless, Transparent, c-Oriented Aluminum Nitride Films Grown at Low Temperature by a Modified Sputter Gun", Appl Phys. Lett., 39 (8), 643-645 (1981)

20. Y. Nakagawa and Y. Gomi, "New Piezoelectric Ta_2O_5 Thin Films", Appl. Phys. Lett., 46 (2), 139-140 (1985)

21. N. F. Foster, "The Deposition and Piezoelectric Characteristics of Sputtered Lithium Niobate Films", J. Appl. Phys., 40 (2), 420-421 (1969)

22. M. Kitabatake, T. Mitsuyu and K. Wasa, "Structure and Dielectric Properties of Amorphous $LiNbO_3$ Thin Films Prepared by a Sputtering Deposition", J. Appl. Phys., 56 (6), 1780-1784 (1984)

23. D. J. McClure and J. R. Crowe, "Charactierization of Amorphous Barium Titanate Films Prepared by rf Sputtering", J. Vac. Sci. Technol., 16 (2), 311-314 (1979)

24. J. K. G. Panitz, "Radio-Frequency-Sputtered Tetragonal Barium Titanate Films on Silicon", J. Vac. Sci. Technol., 16 (2), 315-318 (1979)

25. V. S. Dharmadhikari and W. W. Grannemann, "Photovoltaic Properties of Ferroelectric $BaTiO_3$ Thin Films rf Sputter Deposited on Silicon", J. Appl. Phys. 53 (12), 8988-8992 (1982)

26. Y. Matsui, M. Okuyama, N. Fujita and Y. Hamakawa, "Laser Annealing to Produce Ferroelectric-Phase $PbTiO_3$ Thin Films", J. Appl. Phys., 52 (3), 5107-5111 (1981)

27. M. Kitabatake, T. Mitsuyu and K. Wasa, "Structure and Electrical Properties of Amorphous $PbTiO_3$ Thin Films Sputtered On Cooled Substrates", J. Non-Crystal. Sol., 53, 1-10 (1982)

28. K. Kushida and H. Takeuchi, "Piezoelectricity of c-Axis Oriented $PbTiO_3$ Thin Films", Appl. Phys. Lett., 50 (25), 1800-1801 (1987)

29. A. Okada, "Some Electrical and Optical Properties of Ferroelectric Lead- Zirconate-Lead-Titanate Thin Films", J. Appl Phys., 43 (7), 2905-2909 (1977)

30. S. B. Krupanidhi, N. Maffei, M. Sayer and K. El-Assal, "rf Planar Magnetron Sputtering and Characterization of Ferroelectric Pb(Zr,Ti)O$_3$ Films", J. Appl. Phys., 54 (11), 6601-6609 (1983)

31. L. L. Blyler, J. R., G. E. Johnson and N. M Hylton, "Characterization of Biaxially-Oriented Polyvinylidene Fluoride Film For Transducer Applications", Ferroelectrics, 28, 303-306 (1980)

32. M. A. Marcus, "Ferroelectric Polymers and Their Applications", Ferroelectrics, 40, 29-41 (1982)

33. E. Hausler, W. Kaufmann, J. Petermann, and L. Stein, "Microstructure and Piezoelectric Properties of PVDF Films", Ferroelectrics, 60, 45-50 (1984)

34. B. Gross, R. Gerhard-Multhaupt, A. Berraissoul and G. M. Sessler, "Electron-Beam Poling of Piezoelectric Polymer Electrets", J. Appl. Phys., 62 (4), 1429-1432 (1987)

35. J. T. Alfors, M. C. Stinson and R. A. Matthews, "Seven New Barium Minerals From Eastern Fresno County, California", Amer. Minerologist, 50, 314-340 (1965)

36. R. Masse, J. C. Grenier, and A. Durif, "Structure Crus-
talline de la Fresnoite", Bull. Soc. Franc. Miner.
Crist., 90, 20-23 (1967)

37. P. B. Moore and J. Louisnathan, "Fresnoite: Unusual
Titanium Cooordination", Science, 156, 1361-1362 (1967)

38. L. D. Calvert and J. Trotter, "Fresnoite", Structure
Reports, 32A, 442-443 (1967)

39. G. Blasse, "Fluorescence of Compounds with Fresnoite
($Ba_2TiSi_2O_8$) Structure", J. Inorg. Nucl. Chem., 30,
2283-2284 (1968)

40. C. R. Robbins, "Synthesis and Growth of Fresnoite
($Ba_2TiSi_2O_8$) From a TiO_2 Flux and its Relation to the
System $BaTiO_3- SiO_2$", J. Research of NBS-A. Phys.
Chem., 74A (2), 229-232 (1970)

41. M. Kimura, Y. Fujino and T. Kawamura, "New Piezoelec-
tric Crystal: Synthetic Frenoite ($Ba_2Si_2TiO_8$)", Appl.
Phys. Lett., 29 (4), 227-228 (1976)

42. J. Eckstein, K. Recker and F. Wallrafen, "Zuchtung von
Fresnoite, $Ba_2TiSi_2O_8$", Naturwissenschaften, 63, 435
(1976)

43. M. Kimura, "Elastic and Piezoelectric Properties of
$Ba_2Si_2TiO_8$", J. Appl. Phys., 43 (7), 2350-2356 (1977)

44. S. Haussuhl, J. Eckstein, K. Recker and F. Wallrafen,
"Growth and Physical Properties of Fresnoite
$Ba_2TiSi_2O_8$", J. Cryst. Growth, 40, 200-204 (1977)

45. J. Melngailis, J. F. Vetelino, A. Jhunjhunwala, T. B. Reed, R.E. Fahey and E. Stern "Surface Acoustic Wave Properties of Fresnoite $Ba_2Si_2TiO_8$", Appl. Phys. Lett., 32 (4), 203-205 (1978)

46. H. Yamauchi, "Surface-Acoustic_Wave Characteristics of Frenoite ($Ba_2Si_2TiO_8$) Single Crystal", J. Appl Phys., 49 (2), 6162-6164 (1978)

47. H. Yamauchi, K. Yamashita and H. Takeuchi, "$Ba_2Si_2TiO_8$ For Surface-Acoustic-Wave Devices", J. Appl. Phys., 50 (5), 3160-3167 (1979)

48. M. Ayukawa, "$Ba_2Si_2TiO_8$ Thin Films", M. A. Sc. Thesis, University of Windsor, Windsor, Ontario, Canada (1983)

49. T. C. Murray, "The Determination of the Amorphous to Crystalline Transition Range of Annealed $Ba_2Si_2TiO_8$ Thin Films", B. A. Sc. Thesis, University of Windsor, Windsor, Ontario, Canada (1984)

50. R. J. White, "Fresnoite Ceramics and Thin Films", M. A. Sc. Thesis, University of Windsor, Windsor, Ontario, Canada (1986)

51. R. J. White, M. Ayukawa, G. Demaggio, J. W. Robinson and H. Yamauchi, "Thin Films r.f. Sputtered From $Ba_2Si_2TiO_8$ Ceramic Targets", High Ceramics, edited by P. Vincenzini (Elsevier, Amsterdam), 657-666 (1987)

52. H. Yamauchi, R. J. White, M. Ayukawa, T. C. Murray and J. W. Robinson, "The Structure of Thin Films Sputter Deposited From a $Ba_2Si_2TiO_8$ Ceramic Target," J. Mater. Res., 8 (1), 105-111 (1988)

53. C. Kittel, "Introduction to Solid State Physics", 6th Ed., John Wiley and Sons Ltd., New York. 385-390 (1986)

54. T. Ikeda, "Fundamentals of Piezoelectric Materials Science", (Atsuden Jairyo Gaku no Kiso), Ohmu-sha, tokyo (1984)

55. M. C. Lovell, A. J. Avery, and M. W. Vernon, "Physical Properties of Materials", Van Nostrand Reinhold Co., New York, 168-173 (1976)

56. G. S. Kino and J. Shaw, "Acoustic Surface Waves", Scientific Amer., 227 (4), 50-68 (1972)

57. T. L. Szabo and A. J. Slobodnik, Jr., "The Effect of Diffraction on the Design of Acoustic Surface Wave Devices", IEEE Trans. Sonics and Ultrason., Su-20 (3), 240-251 (1973)

58. A. J. Slobodnik, Jr., E. O. Conway and K. T. Delmonico, USAF Cambridge Res-Labs. Report No. AFCRL-73-0597, 1A (1973) unpublished.

59. P. H. Carr and L. R. M. O'Connell, Proceedings of the 30th Annual Symposium on Frequency Control, p.129 (1976) unpublished

60. I. Ueda and S. Ikegami "Piezoelectric Properties of Modified $PbTiO_3$ Ceramics", Jap. J. Appl. Phys., 7 (3), 236-242 (1968)

61. Y. Ito, H. Takeuchi, S. Jyomura, K. Nagatsuma and S. Ashhida, "Temperature-Compensated $PbTiO_3$ Ceramics for Surface Acoustic Wave Applications", Appl. Phys., Lett., 35 (3), 595-597 (1979)

62. T. Tanaka "Piezoelectric Devices in Japan", Ferroelectrics, 40, 167-187 (1982)

63. A. Halliyall, A. S. Bhalla, R. E. Newnham and L. E. Cross, "$Ba_2TiGe_2O_8$ and $Ba_2TiSi_2O_8$ Pyroelectric Glass-Ceramics", J. Mater. Science, 16, 1023-1028 (1981)

64. A. Halliyal, A. Safari, A. S. Bhalla, R. E. Newnham and L. E. Cross, "Grain-Oriented Glass-Ceramics for Piezoelectric Devices", J. Amer. Cer. Soc., 67 (5), 331-335 (1984)

65. G. R. Barsh And R. E. Newnham, USAF Report No. AFCRL-TR-75-0163 (1975) unpublished

66. D. E. Rase and R. Roy, "Phase Equilibria in the System $BaTiO_3-SiO_2$", J. Amer. Ceram. Soc., 38 (11), 389-395 (1955)

67. M. Kimura, K. Doi, S. Nanamatsu, T. Kawamura, "A New Piezoelectric Crystal: $Ba_2Ge_2TiO_8$", Appl. Phys. Lett., 23 (10), 531-532 (1973)

68. S. A. Markgraf, A. Halliyal, A. S. Bhalla, R. E. Newnham, and C. T. Prewitt, "X-Ray Structure Refinement and Pyroelectric Investigation of Fresnoite, $Ba_2TiSi_2O_8$", Ferroelectrics, 1-10 (1985) to be published

69. A. Halliyal, A. S. Bhalla, S. A. Markgraf, L. E. Cross, and R. E. Newnham, "Unusual Pyroelectric and Piezoelectric Properties of Fresnoite ($Ba_2TiSi_2O_8$) Single Crystal and Polar Glass-Ceramics", Ferroelectrics, 62, 27-33 (1985).

70. Y. Ito, K. Nagatsuma, and S. Ashida, "Surface Acoustic Wave Characteristics of $(Ba_{1-x}Srx)TiSi_2O_8$ Crystals", Appl. Phys. Lett., 37 (11), 894-895 (1980)

71. J. A. Thornton, "Sputter-Coating-Its Principles and Potential", SAE Trans., 82, 1737-1305 (1974)

72. W. R. Grove, "On the Electr-Chemical Polarity of Gases", Trans. Royal Soc., 142, 37 (1852)

73. J. E. Greene, "Crystal Growth by Sputtering", Handbook of Semiconductors, 3, North-Holland Publ. Co., New York, 499-530 (1980)

74. G. M. McCracken, "The Behaviour Of Surfaces Under Ion Bombardment", Rep. Prog. Phys., 33, 241-327 (1975)

75. B. D. Cullity, "Elements of X-Ray Diffraction", 2nd ed., Addison-Wesley Pub. Co., Inc., 281-323 (1978)

76. S. Li, "Analytical Technique of X-Ray Diffraction and Electron Microscope for Metal Materials", Metallurgy Industry Press, China, 63 (1980)

77. G. B. Harris, "Quantitative Measurement of Preferred Orientation in Rolled Uranium Bars", Philosophical Mag., 43 (7), 113 (1952)

78. X. Pan, "X-Ray Metallurgy", Mechanical Industry Press, China, 207 (1980)

79. C. V. Raman, Indian J. Phys., 2, 337 (1928)

80. C. V. Raman and K. S. Krishnan, Indian J. Phys., 2, 399 (1928)

81. W. J. Moore, "Physical Chemistry", Prentice-Hall, New Jersey, Section 17 (1972)

82. T. R. Gilson and P. J. Hendra, "Laser Raman Spectroscopy", Wiley-Interscience (1970)

83. G. Arlt, D. Hennings, and G. Dewith, "Dielectric Properties of Fine-Grained Barium Titanate Ceramics", J. Appl. Phys., 58 (4), 1619-1625 (1935)

84. R. Aroca, Dept. of Chemistry, University of Windsor, private communications

85. G. J. Exarhos, J. Chem. Phys., 81, 5211 (1984)

86. B. Chao, Energy Conversion Devices Inc., Troy, Michigan, private communications

Appendix A

The phase relations at the composition of "BaTiSiO$_5$" (henceforth BTS5) in the BaO - TiO$_2$ - SiO$_2$ ternary system were studied. A recent study [51] found that the compositions of thin films sputter-deposited from a B2TS2 ceramic target were significantly shifted to compositions close to that of "BTS5". D.E. Rase et al.[66], in their study of the BaTiO$_3$ - SiO$_2$ binary system included the compound phase BTS5 (figure 6A) and its powder diffraction data was listed in the JCPDS file (card no. 11-150). In order to analyse the structure of thin films sputter-deposited from B2TS2 targets, an understanding of the phase relations in the vicinity of the composition BTS5 in the BaO - TiO$_2$ - SiO$_2$ ternary system is necessary. The phase relations of B2TS2 were also studied and discussed in Section 5.1.5.

C.R. Robbins [40] successfully synthesized B2TS2 but was unseccessful in synthesizing the compound BTS5, and therefore concluded that the x-ray powder diffraction data previously reported for the compound BTS5 was that of the B2TS2

and that the $BaTiO_3$ – SiO_2 system was not binary. Although the JCPDS data of B2TS2 and BTS5 are very similar, as demonstrated in Figures 65(a) and 65(b), they are not exactly the same. Robbins did not provide an explanation for the non-common diffraction peaks occuring in the two sets of data. In this work, Robbins' conclusions are critically examined by:

1.   calculating the diffraction pattern of B2TS2 using detailed data for the structure of this compound [36], and

2.   carefull analysis of the x-ray diffraction patterns obtained from mixtures of fine powders of $BaCO_3$, TiO_2, and SiO_2 with cation ratios (Ba:Ti:Si) of 1:1:1 heated to various temperatures.

Analysis of the JCPDS data for B2TS2 and BTS5, as illustrated in Figures 65(a) and 65(b), show essentially identical patterns as stated by Robbins. However, the peaks at diffraction angles $2\theta = 14.7°$ and $29.7°$ for B2TS2 and those at $2\theta = 47.3°$, $47.7°$ and $57.3°$ for BTS5 do not appear in the diffraction pattern of the other material (Note that the 332 peak of B2TS2 at $2\theta = 57.99°$ and the 511 peak of BTS5 at $2\theta = 57.97°$ are assumed to be superimposed). Previously [51], the peaks at $2\theta = 14.7°$ and $29.7°$ together with all the common peaks were used to identify the B2TS2 phase and those at

$2\theta = 47.4°$ and $47.7°$ were employed to confirm the compound BTS5. Unless the JCPDS data for both materials were highly reliable, this procedure would be completely misleading. The following information leads us to suspect this reliability:

1. in both cases, all the included peaks have relative intensities of greater than 10% (and interplanar distances larger than 0.158 nm), and

2. among the five noncommon peaks, only the peak at $2\theta = 47.3°$ for BTS5 has an intensity larger than 10%. Thus, the establishment of reliable diffraction patterns for these materials is urgently desired.

Calculation of the diffraction pattern for B2TS2 was performed using the coordinates of each ion in the unit cell determined by R. Masse et al.[36]. These coordinates along the atomic scattering factors listed by B.D. Cullity [75] were used to calculate the structure factor, F_{hkl}, for all combinations of integers h, k, l, that satisfy the relation:

$$(h^2 + k^2)/a^2 + l^2/c^2 < (2/\lambda)^2$$

λ is the wavelength of the CuK_α radiation since the atomic scattering factors for Ba^{2+} are not given in Cullity's list, it was assumed that $f_{Ba}^{2+} = f_{Xe}$ for $(\sin \theta/\lambda) \leq 0.01$ nm^{-1}, and $f_{Ba}^{2+} = f_{Ba}$ for $(\sin \theta/\lambda) > 0.01$ nm^{-1}. The intensity, I_{hkl}, was defined by a product of $|F_{hkl}|^2$, the multiplicity factor for the set of indices hkl and the Lorentz-polarization fac-

tor for the diffraction angle $2\theta_{hkl}$. In this calculation, no absorption factors were taken into account. The calculated x-ray diffraction pattern for B2TS2 is shown in Figure 65(c). Diffraction peaks with mutual diffraction-angle differences less than 0.07° are represented by a single peak. Among multiple sets of indices for a single peak, the foregoing set of indices corresponds to the diffraction peak of the higher intensity. Note that the peaks at $2\theta = 47.3°$ and 56.9° are now singly indexed while they are a multiple index in Figure 65(b) and that the peak at $2\theta = 58.0°$ is now a multiple index. On observation, the calculated pattern (Figure 65(c)) is nothing but a superimposition of the JCPDS patterns given in Figures 65(a) and 65(b) with the addition of some weak peaks with relative intensities less than 5%.

Experimentally, a sample with Ba:Ti:Si ratios of 1:1:1 were prepared following the procedure outlined in section 4.1 (steps 1 to 5). Small amounts of the mixed powder were then heated seperately at temperatures varying from room temperature to 1250° for at least 48 hours. The mixture was then crushed and x-ray diffraction patterns of each sample were taken using CuK_{α} radiation. The diffraction patterns were analyzed using JCPDS data for all the possible phases (listed in Table 3). The x-ray difraction patterns of the material at varying temperatures are shown in Figure 66. The

diffraction pattern of the as-mixed sample includes only the peaks from $BaCO_3$ and TiO_2 but not from SiO_2, as the SiO_2 was in the form of amorphous silica gel. At 850°C, the only peaks which appear, belong to $BaTiO_3$ indicating that the calcination of the $BaCO_3$ was complete and SiO_2 was still in the form of the amorphous gel (for the sake of mass conservation). This identifies the tie-line as the $BaTiO_3 - SiO_2$ line in the $BaO - TiO_2 - SiO_2$ Gibbs triangle (Figure 67). Thus the assumption of D. Rase et al. that the $BaTiO_3 - SiO_2$ system is a binary or quasi-binary system is valid at 850°C. At 1000°C, the B2ST2 phase has formed as a result of the reaction of $BaTiO_3$ with SiO_2. Excess Ba cations formed in this reaction seemed to produce $BaTi_4O_9$ and small amounts of $BaSi_2O_5$. Note that this stage is in nonequilibrium since there are five phases coexisting, including SiO_2 At 1200°C, the same situation exists but with the B2TS2 peaks becoming more intense. At 1250°C, the phase relations have significantly changed with peaks only from B2TS2 and $BaTi_4O_9$ appearing. All the peaks from the calculated B2TS2 diffraction pattern (with the exception of $2\theta = 42.4°$) are among them. Thus, at 1250°C, this material contains B2TS2 and $BaTi_4O_9$, just as Robins found [40]. Two small unknown peaks remain which may be attributed to $BaSi_2O_5$. If this material was near equilibrium after heating at 1250°C, it should have

consisted of at least three phases: B2TS2, BaTi$_4$O$_9$, and either BaSi$_2$O$_5$ or SiO$_2$ as shown on the Gibbs triangle in Figure 67. Energy dispersive x-ray analysis determined the actual composition to be very close to stoichimetric BTS5 as shown in Table 9. Thus, it is concluded that BTS5 is not a single phase but either:

"BTS5" = 54.3 mol % B2TS2 + 27.9 mol% BaTi$_4$O$_9$ + 17.6 mol% BaSi$_2$O$_5$ or

"BTS5" = 70.7 mol% B2TS2 + 23.9 mol% BaTi$_4$O$_9$ + 5.4 mol% SiO$_2$ (amorph)
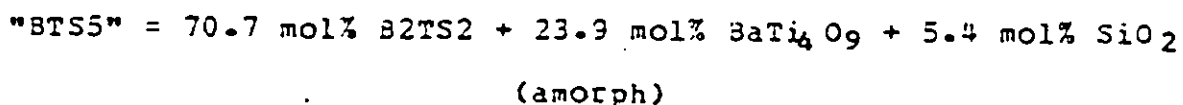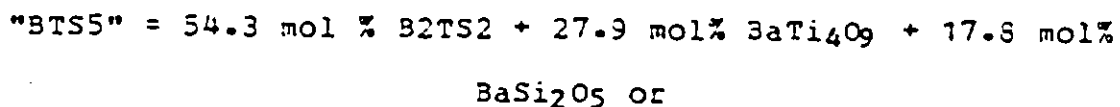
according to the lever rule applied to Figure 67. Case (2) seems more probable than (1) when the relative intensities of the diffraction peaks are compared (see Figure 65(e)). Therefore, at 1250°C, the BaTiO$_3$ − SiO$_2$ line in the BaO − TiO$_2$ − SiO$_2$ Gibbs triangle does not represent the tie line through the composition of "BTS5", and thus the BaTiO$_3$ − SiO$_2$ system is not quasi-binary at 1250°C (above 1250°C the ceramic material melted). In the temperature range of room temperature to 1250°C, no experimental evidence was found for the existence of a single phase compound of BTS5.

Appendix B

C.1   Ceramic Sputtering Target Fabrication

The ceramic sputtering targets used throughout this work were fabricated by mixing high purity (>99.95% pure) $BaCO_3$, SiO_2 and TiO_2 oxide powders according to the formula,

$$2BaCO_2 + 2SiO_2 + TiO_2 ---> Ba_2Si_2TiO_8 + 2CO_2$$
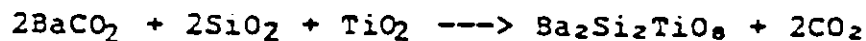
The fabrication procedure is outlined below. It was adopted from a procedure developed by the Hitachi Central Research Laboratory.

1. $BaCO_3$[19], SiO_2[20], and TiO_2[21] oxide powders were dried on a hot plate at 150°C for two hours. This removed any moisture absorbed by the powders.

2.   Immediately after they were baked, the powders were weighed to the desired proportions.

---

[19] Fisher Scientific Co., cat. no. B-30.

[20] Fisher Scientific Co., cat. no. S-662.

[21] Fisher Scientific Co., cat. no. T-315.

[22] Norton Scientific Co., Canlab cat. no.   C8700-1, C8750-4, C8775-1A.

3.   The powders were placed in a ball mill[22] and distilled water was added. They were then mixed for 24 hours.

4.   The powder was dried on a hot plate until all the water had evaporated. This took approximately 10 hours.

5.   The powder was crushed by a mortar and pestle[23] for about 2 hours.

6.   The powder was placed in an alumina crucible and heated for 10 hours at 1000°C in a high temperature furnace[24]. At this temperature, the barium carbonate is calcinated to remove any CO_2.

7.   The powder was crushed and mixed by the mortar and pestle.

8.   5 wt% of high purity paraffin was dissolved in a chlorine-based solvent[25]. The liquid was mixed into the powder with the mortar and pestle. The powder was put on a hot plate and baked at 100°C for about 2 hours. This evaporated the chloroethene VG and left the wax, which acted as a binder, behind.

---

[23] Coors: Canlab cat. no. M9001-5, M9002-5.

[24] Linberg 51314-52314 (furnace) and 59246-828074 (controller)

[25] Dow Chemical Co., Chloroethene VG.

9. The powder was pressed into discs 2.8 cm in diameter
(1.1 in) and between 0.15 and 0.20 cm thick. Each
disc weighed about 3.0 grams. The pressing pressure
was about 3.5 MPa.

10. The discs were sintered on Al_2O_3 plates in the high
temperature furnace. They were held at 400°C for 10
hours to allow the binder and any absorbed moisture to
evaporate. The furnace temperature was then increased
at a rate of 50°C/hour until the sintering temperature
(1245-1275°C depending on the composition) was
reached. The discs were sintered for 5 hours. The
temperature was decreased at a rate of 50°C/hour down
to 700°C, and then they were allowed to cool more
quickly.

VITA AUCTORIS

The author was born in Windsor, Ontario, Canada on May 31, 1961.

EDUCATION: Secondary School Diploma,
obtained at the Hon. W.C. Kennedy Collegiate,
Windsor, Ontario, Canada
1980

B.A.Sc. in Engineering Materials,
obtained at the University of Windsor,
Windsor, Ontario, Canada
1985

Accepted into the Faculty of
Graduate Studies and Research through
the Department of Engineering Materials,
University of Windsor,
Windsor, Ontario, Canada
as a candidate for the degree of M.A.Sc.
in Engineering Materials

TABLE 1

Applications of Piezoelectric Materials[55,62]

APPLICATION	MATERIAL
Accelerometers	PZT ceramics $BaTiO_3$
Filters: Quartz (narrow band)	Quartz
Mechanical (low frequency)	PZT ceramic (Cr-doped)
Ceramic	piezoelectric ceramics
High Voltage Generation (gas lighters, piezoelectric transformers.	$BaTiO_3$ PZT ceramics
Gramophone Pick-ups	Rochelle salt $BaTiO_3$ PZT ceramics
Measurement Devices (pressure and vibrational measurement devices)	$BaTiO_3$ PZT ceramics
Resonators (for frequency control)	Quartz
SAW Devices (high frequency filters, delay lines, amplifiers, oscillators)	Quartz ZnO $LiNbO_3$ AlN $LiTaO_3$ PZT ceramics
Transducers: Air (ear phones, hearing aids, microphones)	Rochelle salt
Audio (underwater sonar, piezoelectric buzzers and speakers)	$BaTiO_3$ PZT ceramics
Ultrasonic (ultrasonic cleaners, processing machines and medical diagnosis machines, fish finders, alarm systems)	$BaTiO_3$ PZT ceramics AlN ZnO

TABLE 2

Physical and Chemical Properties of Fresnoite

		References
Chemical Formula	$Ba_2TiSi_2O_8$	35
Unit Cell Content	$2\ [Ba_2TiSi_2O_8]$	35
Crystal Structure	Noncentrosymmetric Tetragonal	35
Space Group	P4bm	35
Lattice Constants	a=b= 0.852 ± 0.001 nm c= 0.521 ± 0.0005 nm	35
Density	4.45 g/cm^3	36
Melting Point	1445 ± 5°C	42
Solvents	hot: 1:1 H Cl cold: glacial acetic acid	35
Linear Thermal Expansion Coefficient (0°C)	$\alpha_a = 8.7 \times 10^{-6}/°C$	44
	$\alpha_c = 9.3 \times 10^{-6}/°C$	44
Electromechanical Coupling Coefficient	(x-cut y-prop.)K = 0.25 (Z-cut x-prop.)K = 0.10	69 43
Temperature Coefficient of delay	(x-cut y-prop.) 38 ppm/°C (z-cut x-prop.) 51 ppm/°C	43 45
Dielectric Constant (10 MHz ; 20°C)	$\epsilon_{11} = 12.5$ $\epsilon_{33} = 8.55$	44
Piezoelectric Constant	(x-cut y-prop.) $|d| = 18 \times 10^{-12}$(C/N) (z-cut x-prop.) $|d| = 2.7 \times 10^{-12}$ (C/N)	43 43

TABLE 3

Symbols and JCPDS File Numbers of Compounds
Appearing in Diffraction Patterns

SYMBOL	CHEMICAL FORMULA	JCPDS File No.
B	$BaCO_3$	5-0378
C (BT3)	$BaTiO_3$	5-0626
D (BS4)	Ba_2SiO_4	26-1403
E (BS3)	$BaSiO_3$	6-0247
F (BTS8)	$Ba_2TiSi_2O_8$	22-513
G ((BS5)	$BaSi_2O_5$	26-176
H (BT9)	$BaTi_4O_9$	34-70
T	TiO_2 (anatase)	21-1272
?	Unidentified	-----

TABLE 4

Molecular Weights and Stoichiometric Amounts

For Fabricating 100 gms of Fresnoite

MATERIAL	MOLECULAR WEIGHT	STOICHIOMETRIC AMOUNTS (g)
$2BaCO_3$	394.70	66.36
TiO_2	79.90	13.44
$2SiO_2$	120.172	20.20
$Ba_2TiSi_2O_8$	506.752	100.00

TABLE 5

Density and Volume Measurements of B2TS2 Targets

METHOD	SAMPLE	THICKNESS (cm)		DIAMETER (cm)		VOLUME (cm³)			WEIGHT (g)		DENSITY (g/cm³)		
		INITIAL	FINAL	INITIAL	FINAL	INITIAL	FINAL	% DECREASED	INITIAL	FINAL	INITIAL	FINAL	% DECREASED
1	T1	0.201	0.183	2.794	2.300	1.232	0.760	38.31	3.5009	3.2013	2.842	4.212	94.75
	T2	0.168	0.149	2.794	2.310	1.030	0.624	39.42	3.0013	2.6004	2.914	4.167	93.64
	T3	0.187	0.177	2.540	2.260	0.948	0.710	25.11	2.5190	2.3850	2.658	3.359	74.48
2	T4	0.167	0.151	2.540	2.260	0.846	0.606	28.35	2.1047	1.9951	2.488	3.292	74.00
	T5	0.197	0.179	2.540	2.240	0.998	0.705	29.36	2.4965	2.3782	2.502	3.373	75.80

TABLE 6

Operating Parameters and Window Settings for EDS Analysis

Accelerating Voltage	15 KV
Emission Current	100 μA
Counting Time	30 seconds
Magnification	2,000 X
Standards Used	$BaTiO_3$; silica gel

Windows: (KEV)

I	Si	1.52 - 1.82
II	BKg	2.00 - 2.30
III	BKg	3.50 - 3.80
IV	Ti + Ba	4.30 - 4.60
V	Ba	5.00 - 5.30
VI	BKg	5.50 - 5.80

TABLE 7

Calculated wt% and at% of B2TS2 Samples

Using Results of EDS Analysis

SAMPLE	Ba wt%	at%	Ti wt%	at%	Si wt%	at%	O wt%	at%
Ceramic Powder	40.83	9.50	18.42	12.29	3.74	4.26	37.01	73.94
Target 1	42.11	8.97	10.43	6.37	2.74	2.85	44.72	81.80
Target 2	36.63	7.01	8.25	4.53	2.91	2.72	52.21	85.75
Thin Film	38.51	8.61	13.57	8.70	11.23	12.27	36.69	70.42
Ideal Composition		15.38		7.69		13.38		61.54

TABLE 8

X-Rays Diffraction Peaks of B2TS2 Ceramic Targets Fabricated by (a) Previous Method (Figure 32), (b) Modified Method (Figure 33) and (c) JCPDS Standard Diffraction (card no. 22-513)

(a) PREVIOUS 2θ	d	TARGET I/Io	(b) MODIFIED 2θ	d	TARGET I/Io	(c) JCPDS 2θ	d	STANDARD I/Io
14.5	6.11	5	14.5	6.07	-5	14.68	6.03	5
16.8	5.28	10	16.8	5.25	-30	16.97	5.22	14
20.6	4.31	5	20.7	4.29	-10	20.79	4.27	8
22.2	4.00	10	22.4	3.97	-20	22.49	3.95	12
23.1	3.85	30	23.2	3.84	-30	23.27	3.82	20
25.8	3.45	1				BS4,BS3		
26.7	3.34	60	26.9	3.31	-70	27.00	3.30	45
28.8	3.10	100	28.8	3.10	-100	28.97	3.08	100
29.4	3.04	20	29.5	3.03	-20	29.55	3.02	10
30.2	2.96	3				BS4		
31.4	2.85	3				BT3		
33.2	2.70	40	33.2	2.71	-50	33.19	2.697	25
34.1	2.63	30	34.2	2.62	-40	34.37	2.607	20
37.3	2.41	10	37.4	2.40	-20	37.52	2.395	8
37.8	2.38	3	38.0	2.37	-5	38.03	2.364	2
38.7	2.33	1				BT3		
40.2	2.24	7	40.3	2.24	-10	40.55	2.223	6
41.6	2.17	30	41.8	2.16	-40	41.97	2.151	20
42.2	2.14	1	42.3	2.13	-5	42.34	2.133	4
43.5	2.08	25	43.7	2.08	-30	43.71	2.069	16
44.9	2.02	20	45.0	2.01	-20	45.09	2.009	10
45.7	1.99	7	45.8	1.981	-15	46.01	1.971	6
47.0	1.93	25	47.1	1.929	-30	47.25	1.922	15

TABLE 8 (continued).

(a)			(b)			(c)		
PREVIOUS		TARGET	MODIFIED		TARGET	JCPDS		STANDARD
2θ	d	I/Io	2θ	d	I/Io	2θ	d	I/Io
47.4	1.92	7	47.6	1.910	-10	47.65	1.907	6
48.2	1.89	35	48.4	1.88	-50	48.54	1.874	20
51.9	1.79	3	52.1	1.76	7	52.16	1.752	2
52.1	1.76	5	52.4	1.75	5	52.62	1.738	3
55.2	1.66	3	54.8	1.68	-4	55.01	1.668	1
55.8	1.65	1	55.5	1.656	-3	55.66	1.650	2
56.3	1.63	10	56.6	1.62	20	56.78	1.620	9
						57.21	1.609	5
57.7	1.60	20	57.8	1.60	30	57.90	1.5913	11
			58.0	1.59	30	58.34	1.5804	11
59.6	1.55	3	60.0	1.54	5	60.08	1.5387	2
60.7	1.53	7	61.1	1.52	10	61.10	1.5154	6
						61.46	1.5074	5
63.1	1.47	5	63.6	1.47	5	63.57	1.4624	3
65.2	1.43	5				BS4,BS3		
65.4	1.43	5	65.6	1.43	5	65.61	1.4218	3
66.0	1.42	5	66.3	1.41	5	66.33	1.4081	3
			66.5	1.41		66.66	1.4019	2
68.0	1.38	3	68.3	1.37	3	68.32	1.3718	2
68.9	1.36	3	69.3	1.36	3	69.37	1.3546	2
70.2	1.34	7	70.6	1.33	10	70.75	1.3305	5

TABLE 9

Composition of Fabricated Materials used for Phase Analysis

From Energy Dispersive X-Ray Analyses

SAMPLE	Ba:Ti:Si Ratios		Composition (at .%)		
			Ba	Ti	Si
A	2:1:2	Experimental	37±2	26±2	38±2
		Theoretical	40.0	20.0	40.0
B	1:1:1	Experimental	34±1	34±1	32±1
		Theoretical	33.33	33.33	33.33

TABLE 10

Operating Conditions Applied for R.F. Triode Sputtering

Deposition of B2TS2 Thin Films

R.F. Power	Incident	50 W
	Reflected	$\sim$1.0 W
Plasma Current		$\sim$2.0 A
Plasma Voltage		$\sim$42.0 V
Electron Emitter Current		22$\sim$28 A
Sputtering Gas		Argon
Sputtering Gas Pressure		$\sim$240 mTorr
Target - Substrate Distance		$\sim$72 mm
Target Diameter		$\sim$22.5 m
Substrate Temperature		650° - 800°C
Sputtering Time		6 - 24 hrs.
Substate Material		(100) Si

TABLE 11

Thermal Conditions and Observations of B2TS2 Thin Films

SAMPLE	SUBSTRATE TEMPERATURE (°C)	SPUTTERING TIME (hrs)	THICKNESS (Å)	X-RAY DIFFRACTION MORPHOLOGY	COMMENTS
1	650	6	-----	amorphous	-appears to be amorphous with crystalline islands forming
2	675	6	1100 – 1500	amorphous	-crystallite islands growing with possible orientation inside islands
3	700	6	1500 – 2000	crystalline with signs of poly-crystalline structure	-amorphous region disappears -large island coalesce and smaller grains begin to form
4	725	7	1000 – 1300	highly oriented crystalline structure	-tiny round grains appear throughout -pits or volcano-shaped regions appear -signs of cracking
5	750	7	-----	polycrystalline	-(00n) peaks still dominant, but a mixed structure -small grains again coalesce into large grains, but still appear in grain boundaries
6	775	8	-----	polycrystalline	-large grains begin to transform into smaller grains

TABLE 11 (continued)

SAMPLE	SUBSTRATE TEMPERATURE (°C)	SPUTTERING TIME (hrs)	THICKNESS (Å)	X-RAY DIFFRACTION MORPHOLOGY	COMMENTS
7	800	5	-----	polycrystalline	-complete transformation into a random mosaic orientation of small grains
8	700	8	------	crystalline, polycrystalline, amorphous	-preferentially oriented peak predominate with other, polycrystalline peak beginning to form -amorphous region still exists -small, round grains appear throughout the darkened (amorphous?) region with larger grains (polycrystalline) beginning to form
9	725	13	4000 - 5000	polycrystalline	-diffraction pattern shows a polycrystalline morphology, although, the (00n) oriented peaks are still predominant -smaller grains appear to be coalescing or even being covered over with larger grains
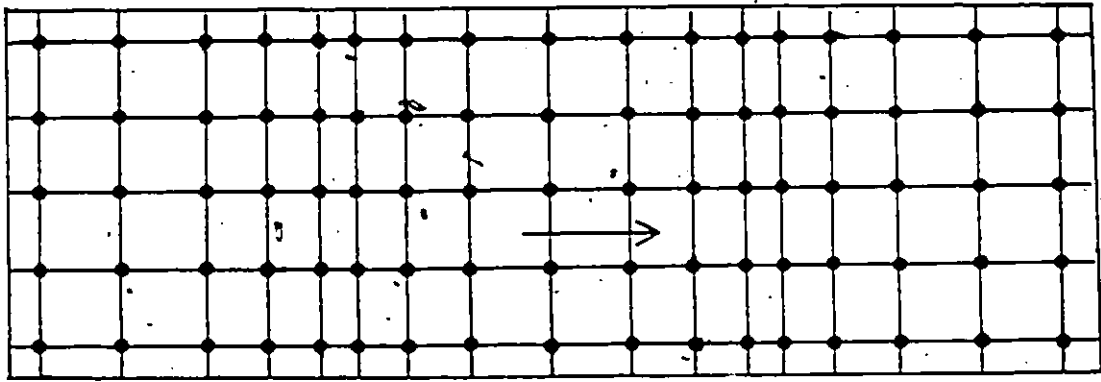
(a)
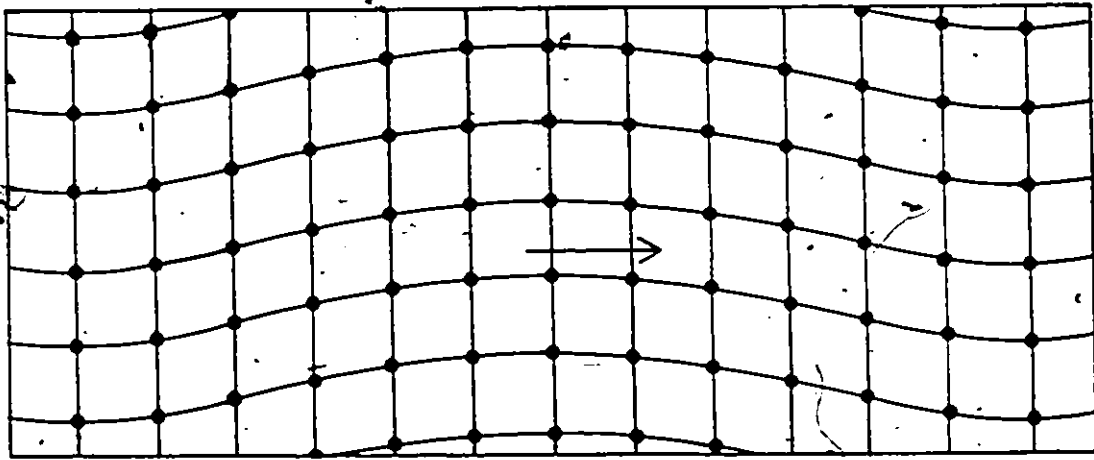
(b)
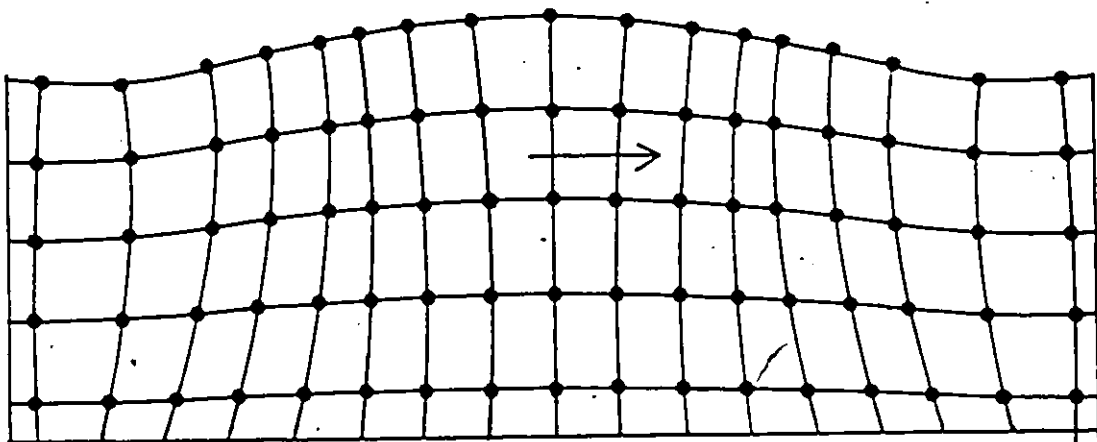
(c)

Figure 1: Types of acoustic waves which travel through solids
include: a) Longitudinal waves, b) Transverse waves,
and c) Rayleigh waves [56,57].
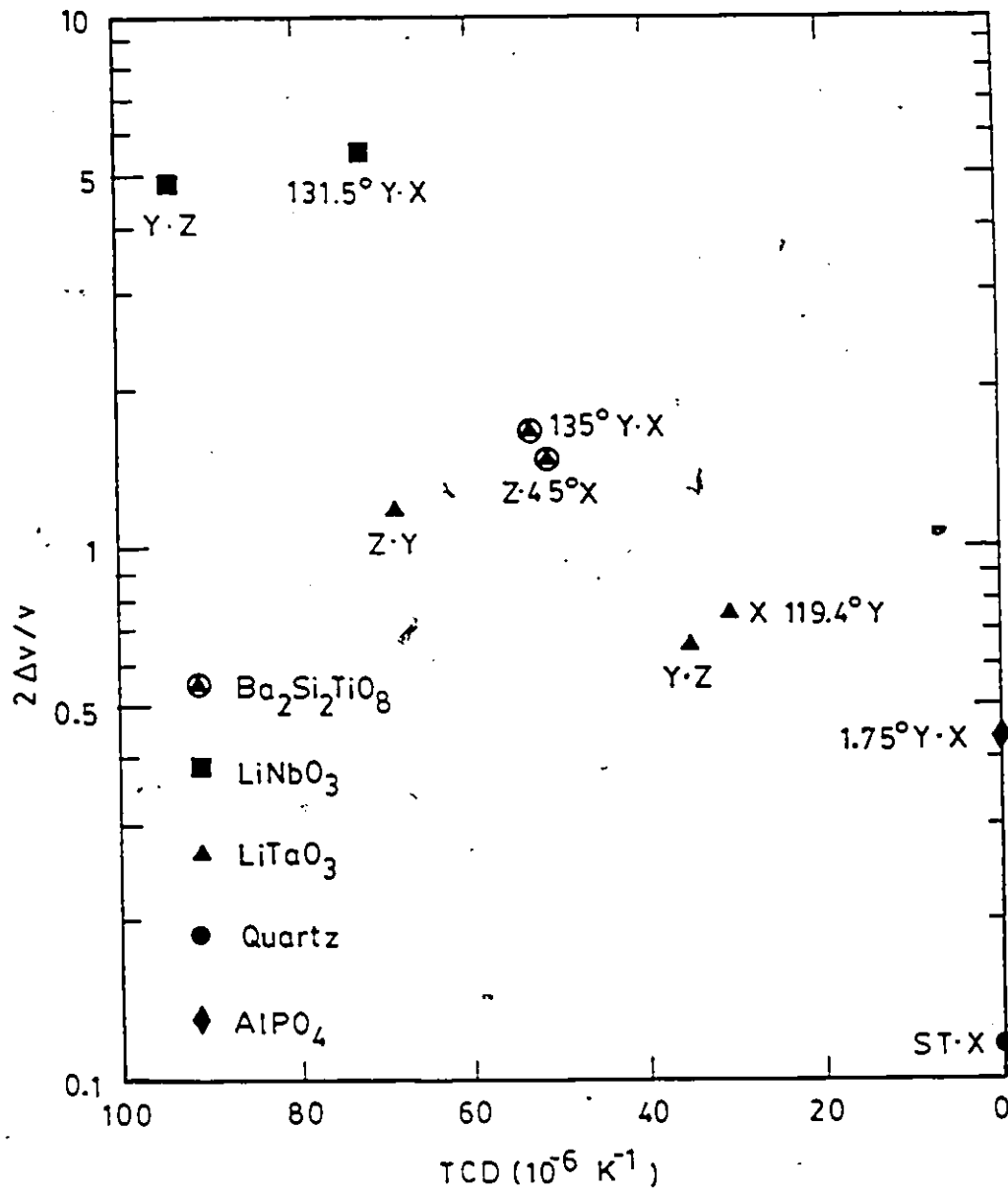
Figure 2: Electromechanical coupling factor, 2 Δv/v, vs. temperature coefficient of delay, TCD, for sets of SAW propagation planes and directions in piezoelectric single crystals [47].

c-axis ↑

a-axis →

BST
Columnar
Grain

Substrate

$\overline{\qquad}$
0.25 μm
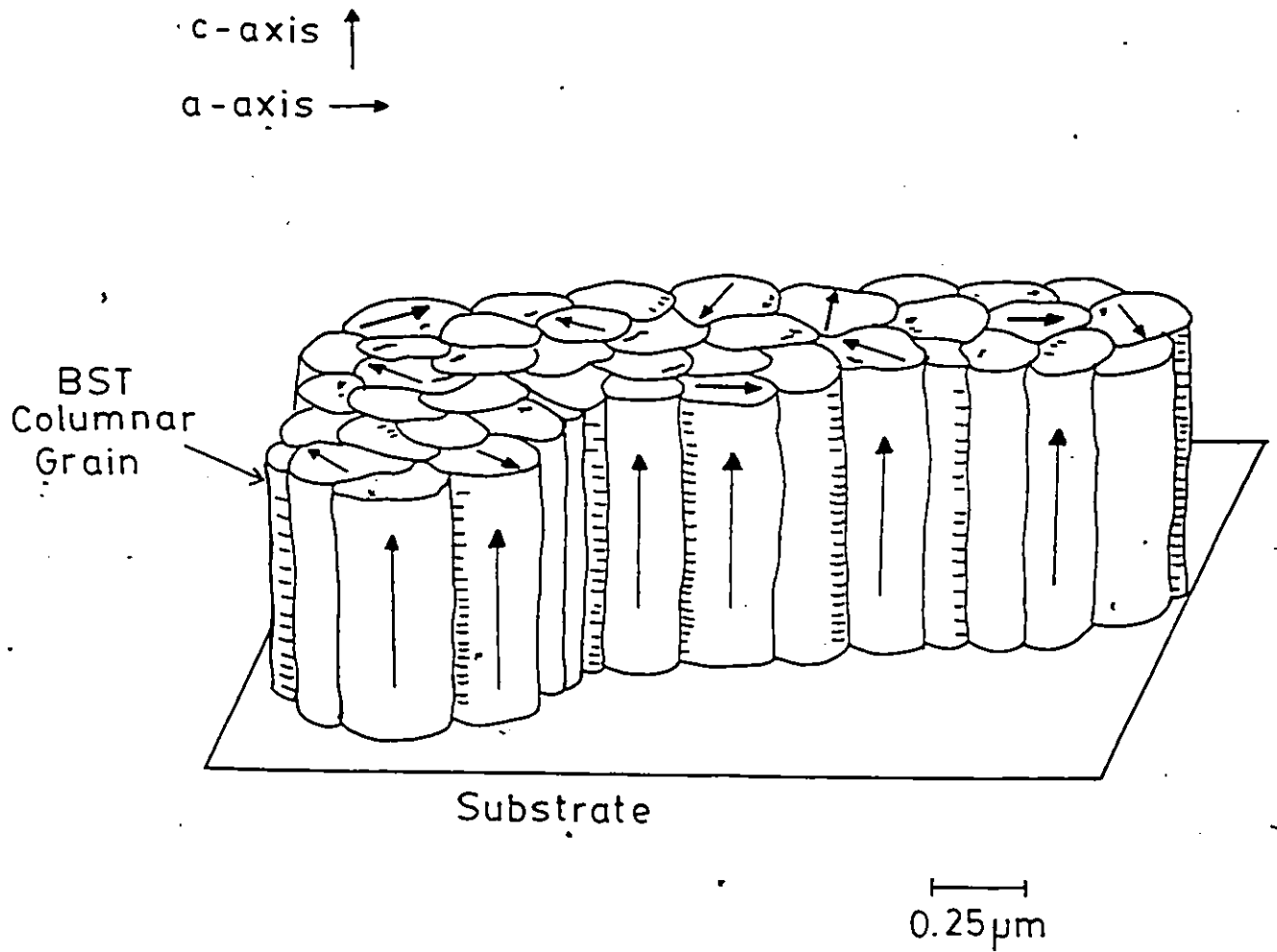
Figure 3: Schematic illustration of a c-axis columnar
oriented thin film structure.
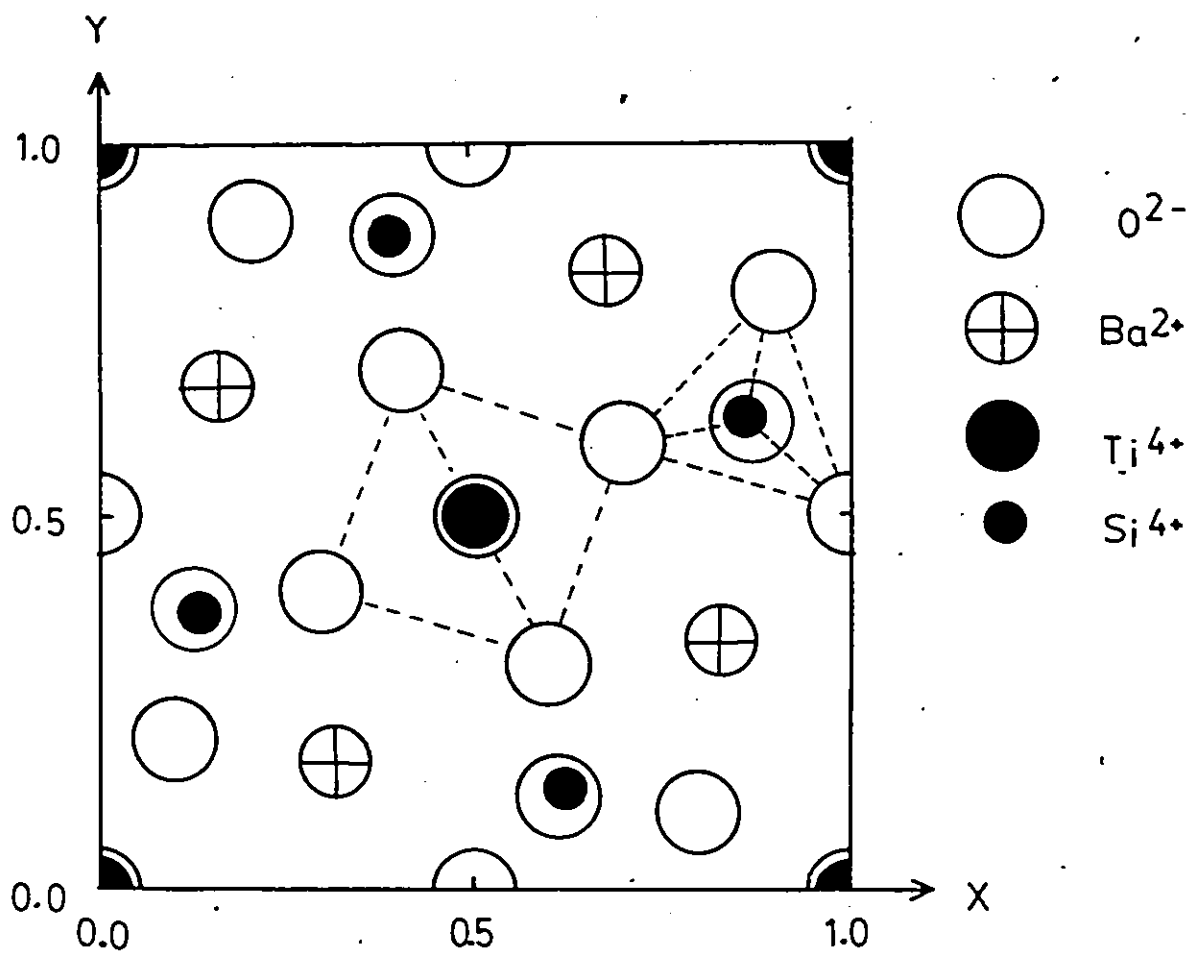
Figure 4: Crystalline structure of $Ba_2TiSi_2O_8$ projected on the X-Y plane [36].
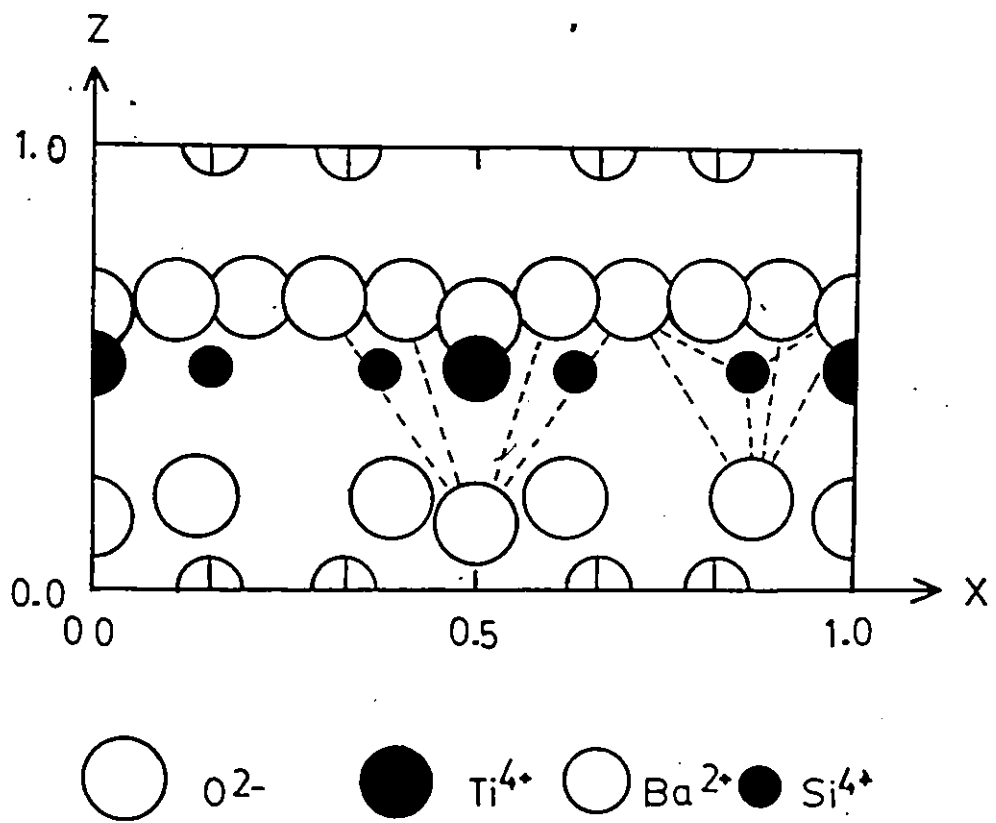
Figure 5: Crystalline structure of $Ba_2TiSi_2O_8$ projected on the X-Z plane [36].
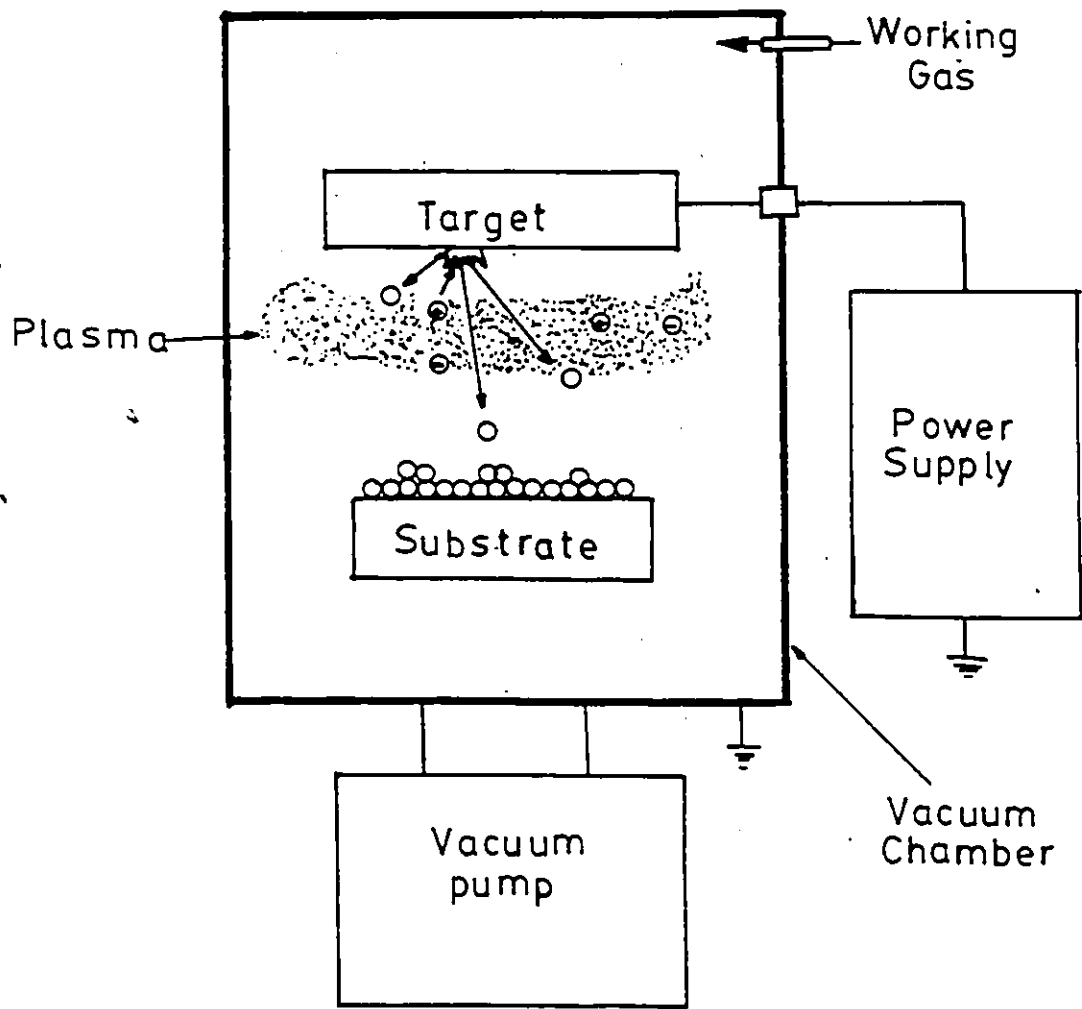
Figure 6: Schematic diagram of sputtering system.
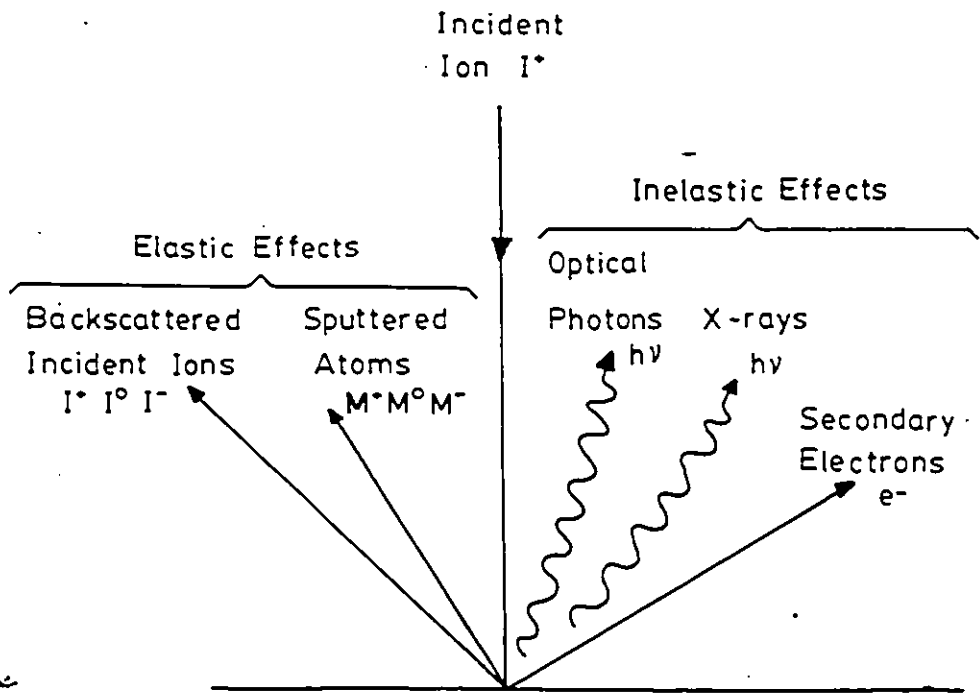
Figure 7: Schematic diagram of ion-surface interactions.

Substrate

Filament Shield

Magnet

Ar Gas Flow

Target

Filament

Anode

Confinement Ring

Target Module

−

+

Filament Module

Plasma Discharge Module

+

−

Igniter Module
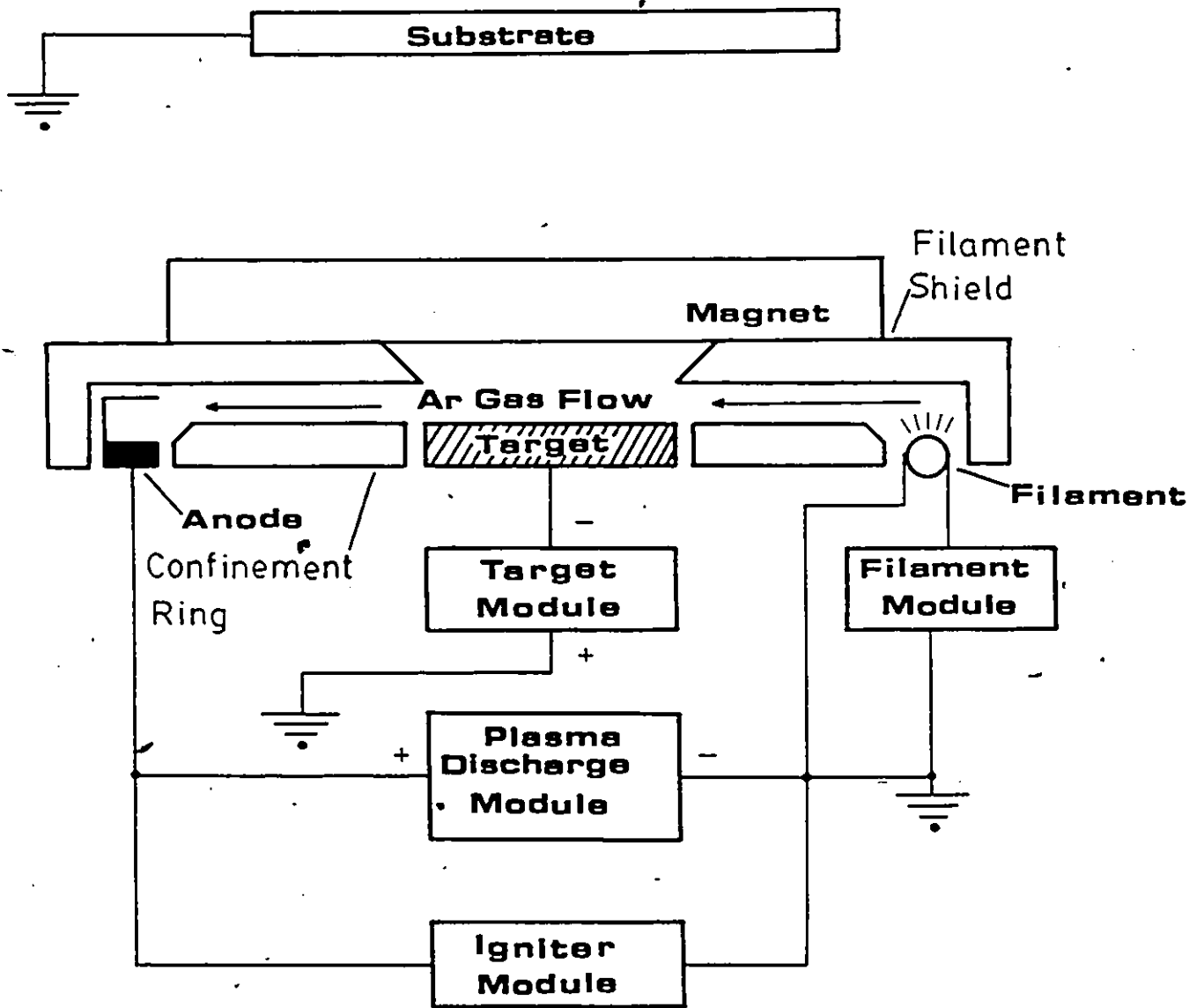
Figure 8: Schematic illustration of the target area.

DC. Power Supply

R.F. Power Supply

Vacuum Gages

High Vacuum Valve

Electric Power Code

BRV Valve

Chamber Lid

Chamber

Liquid Nitrogen Trap

Diffusion Pump

Mechanical Pump
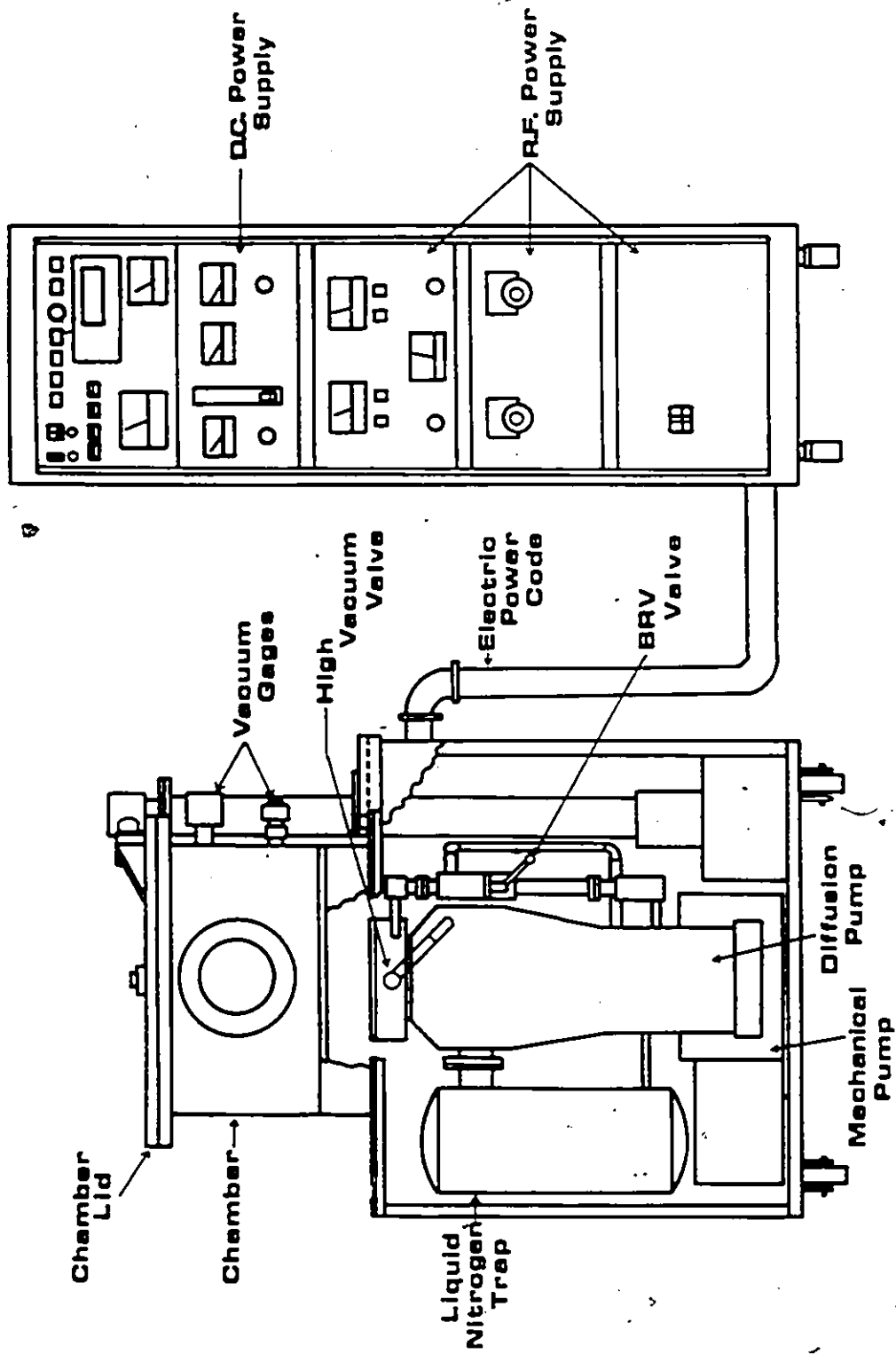
Figure 9 a): Schematic illustration of the r.f. triode sputter deposition system.
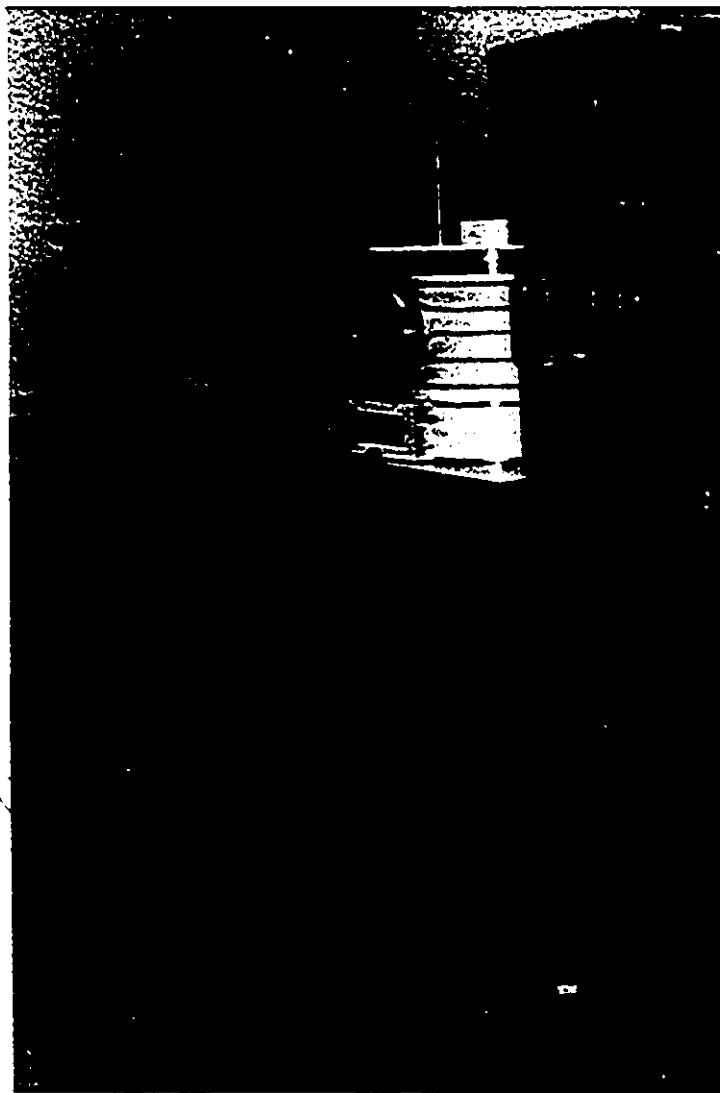
Figure 9 b): Overall view of the r.f. triode sputter deposition unit.
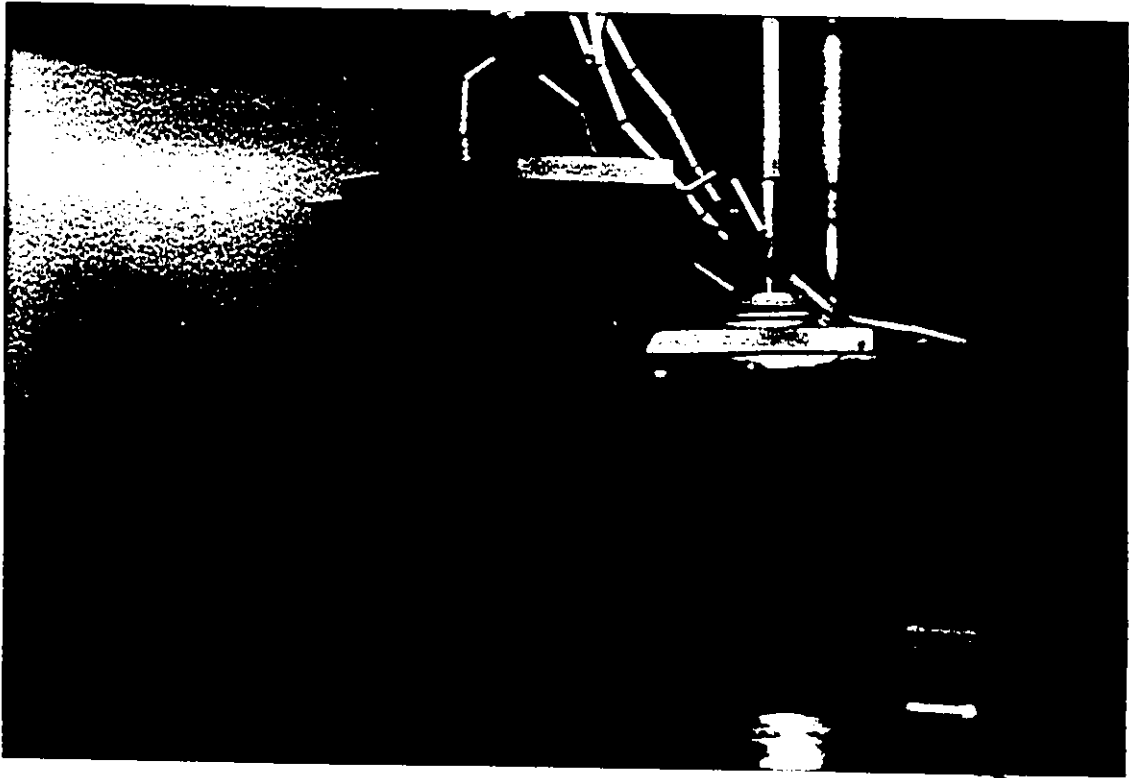
Figure 10: Tantalum wire heater used to heat substrate.
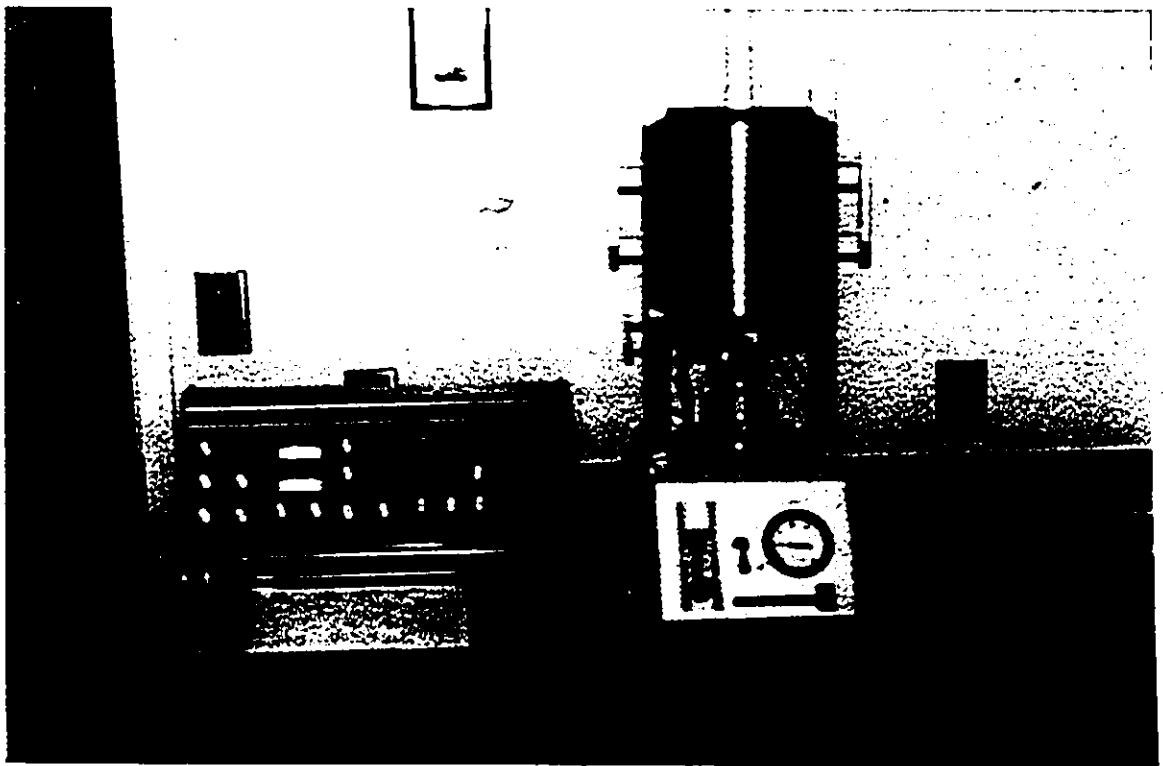
Figure 11:   Differential Thermal Analyzer.
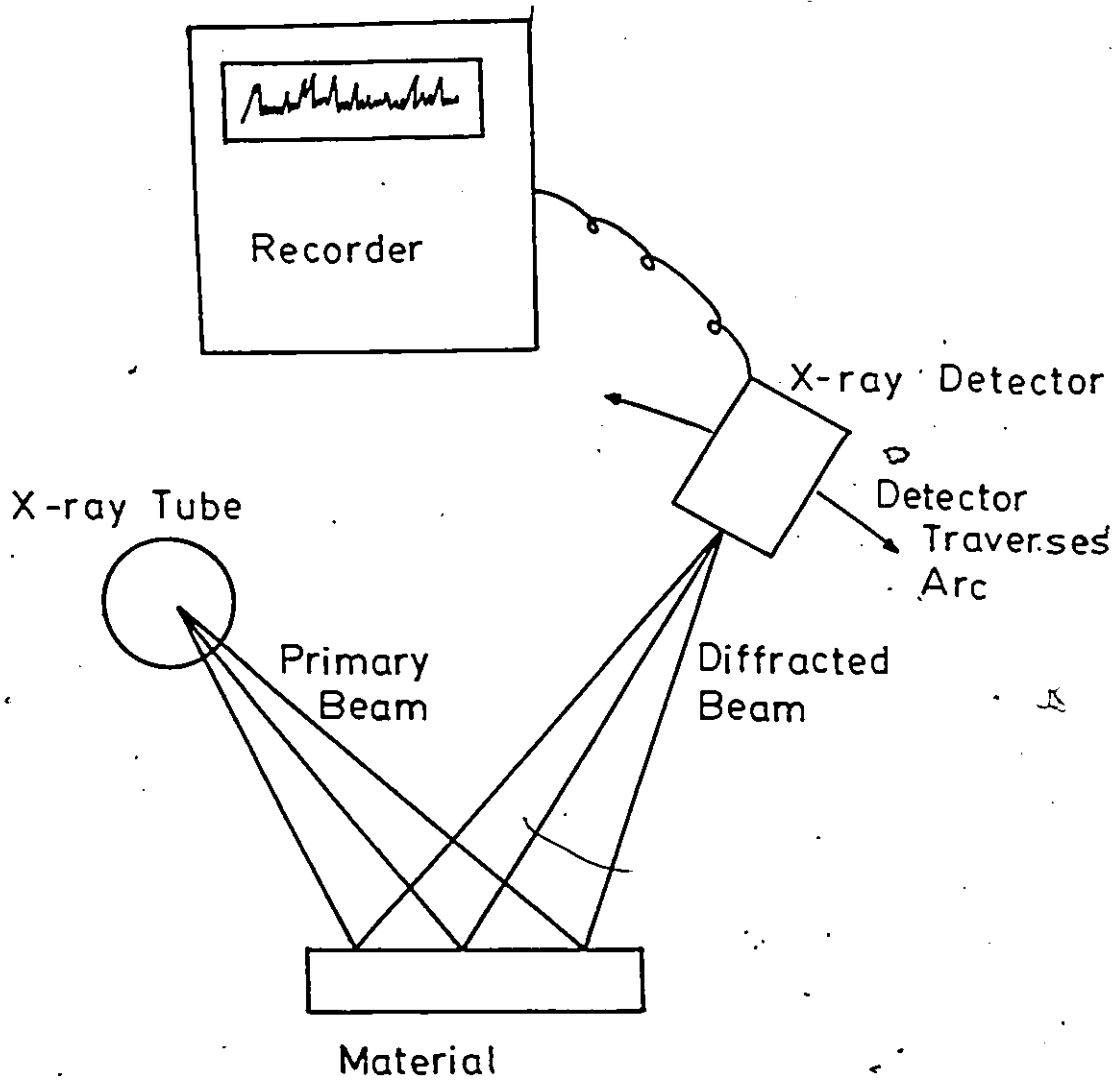
Figure 12: Schematic diagram of x-ray diffraction process.
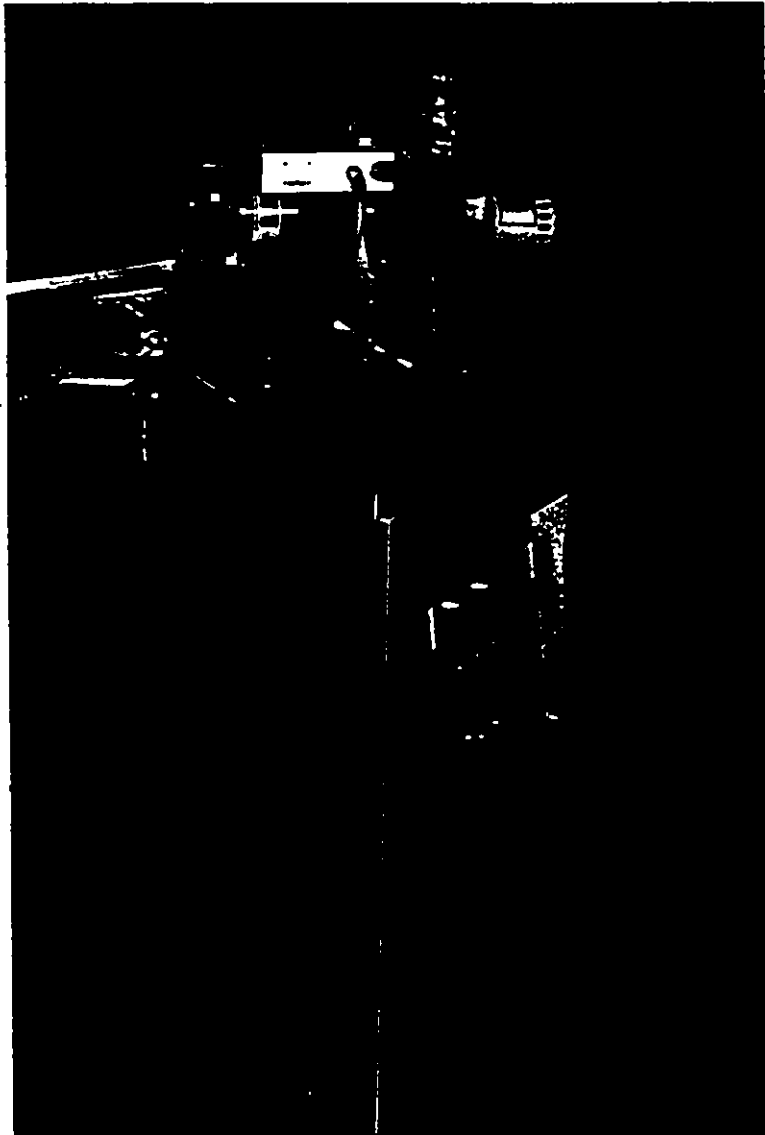
Figure 13: X-ray diffractometer.
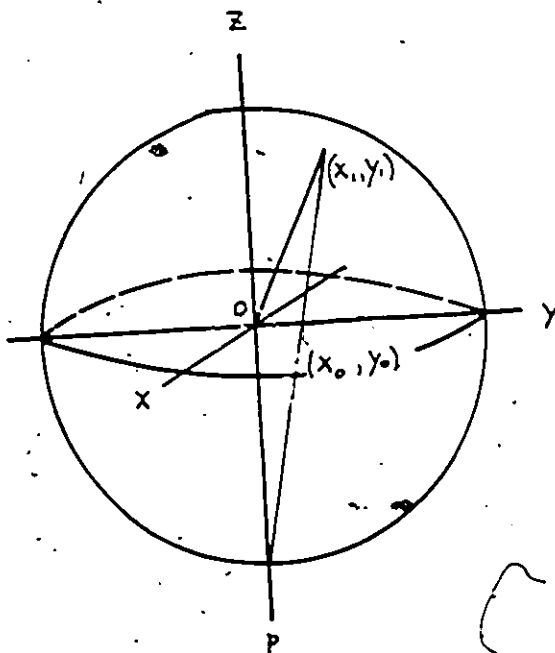
Figure 14:   Schematic designation of a stereo
projection figure.
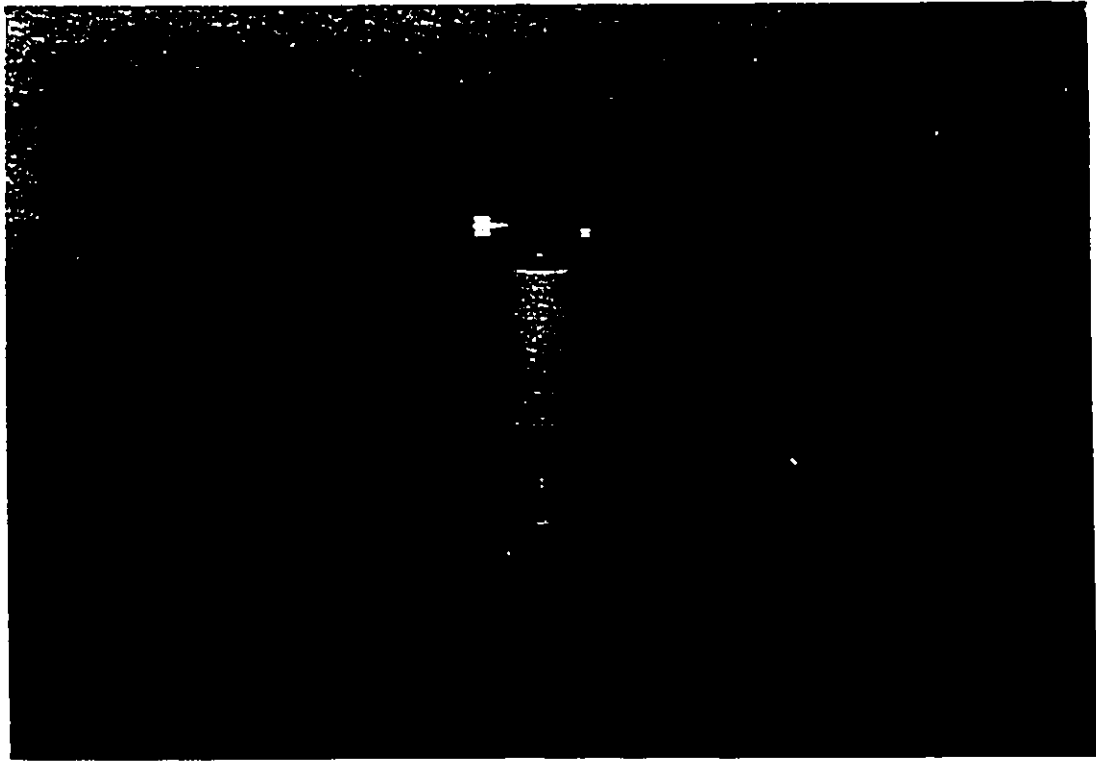
Figure 15: Multiple beam interferometer used to
measure thin film thickness.

OBJECTIVE OF MICROSCOPE,
EYE, OR GENERAL IMAGE
FORMING SYSTEM

COLLIMATED
MONOCHROMATIC
LIGHT

HALF-SILVERED MIRROR

PARTIALLY TRANSPARENT,
HIGHLY REFLECTIVE
COATING ON PLANAR
REFERENCE PLATE
(FIZEAU PLATE)

B   B'

A   A'

EVAPORATED, OPAQUE
HIGHLY REFLECTIVE
COATING

SUBSTRATE

SAMPLE FILM WITH
CHANNEL

B   B'

RESULTING
INTERFEROGRAM

A   A'
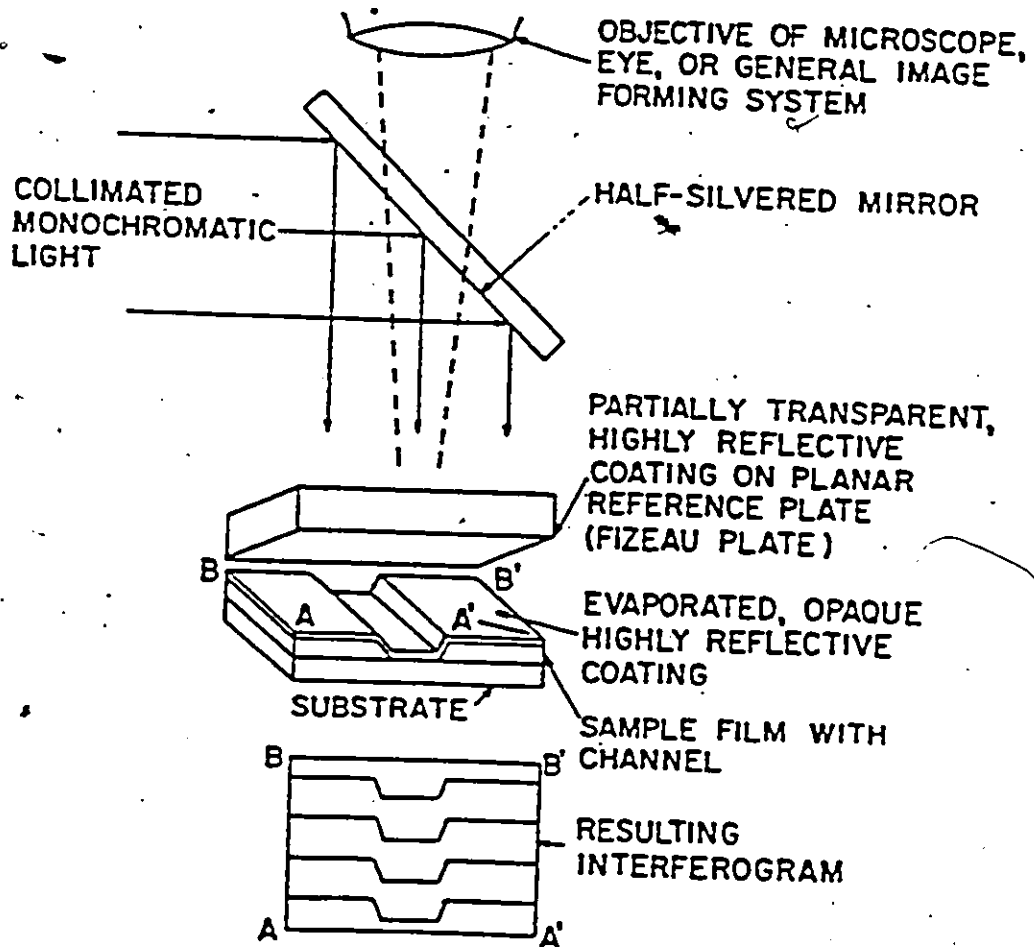
Figure 16:   Schematic of optical elements.
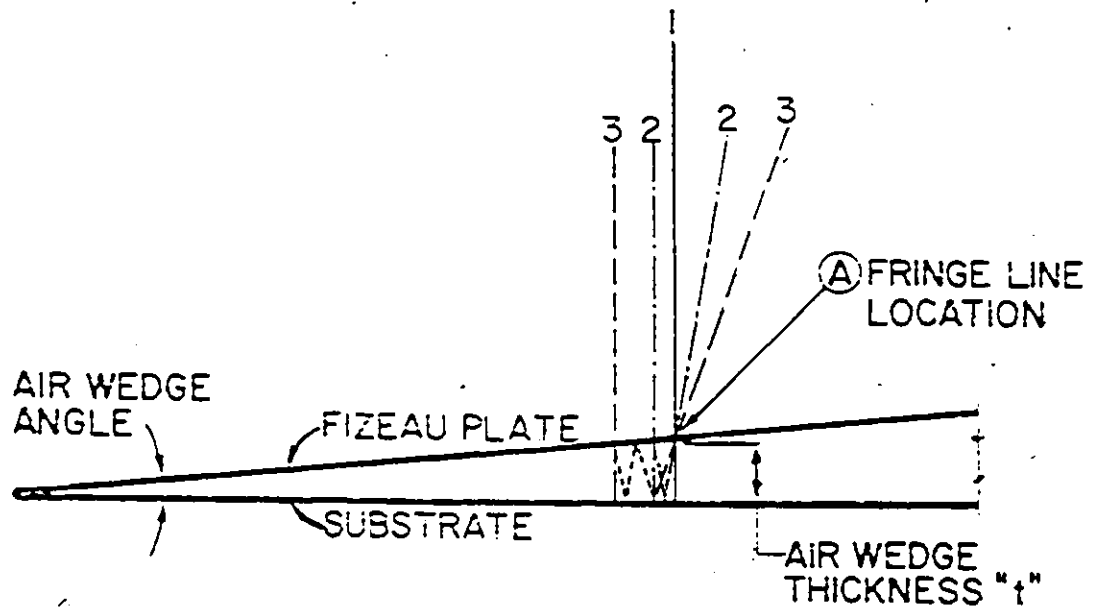
Figure 17: Forming interference fringe patterns.
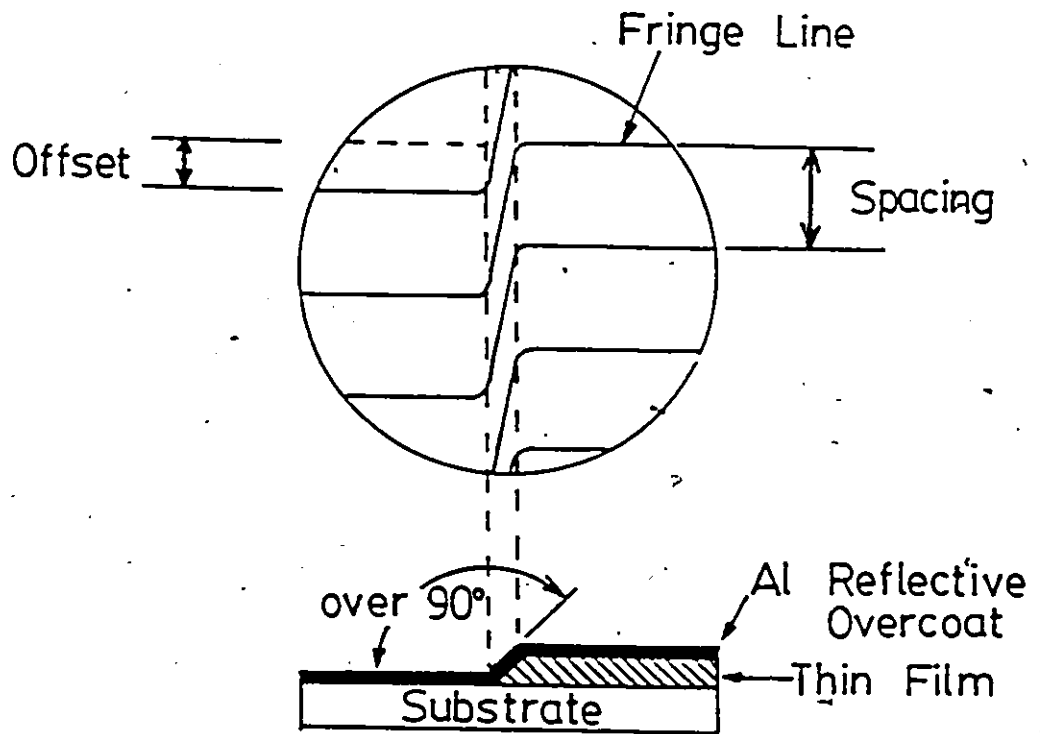
$$\text{Film Thickness (nm)} = \frac{\text{Offset (filar units)}}{\text{Spacing (filar units)}} \times 294.6 \text{ (nm)}$$

Figure 18: Fringe patterns produced from a thin film.
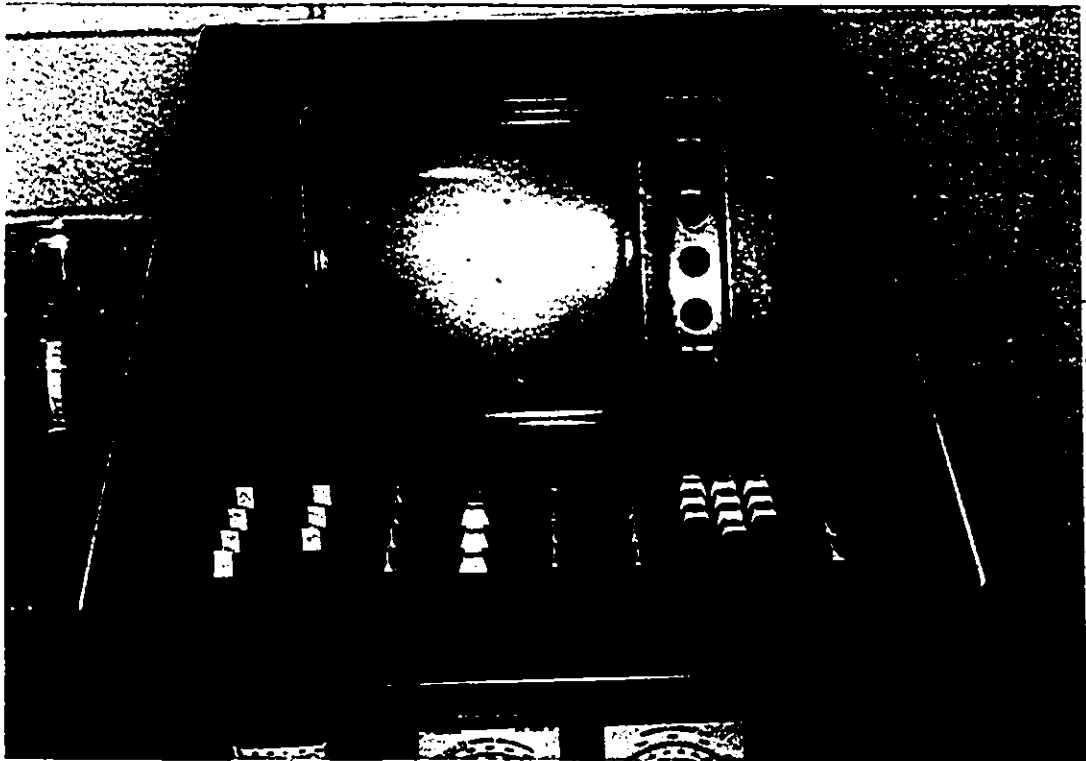
Figure 19: Energy dispersive x-ray analyzer.
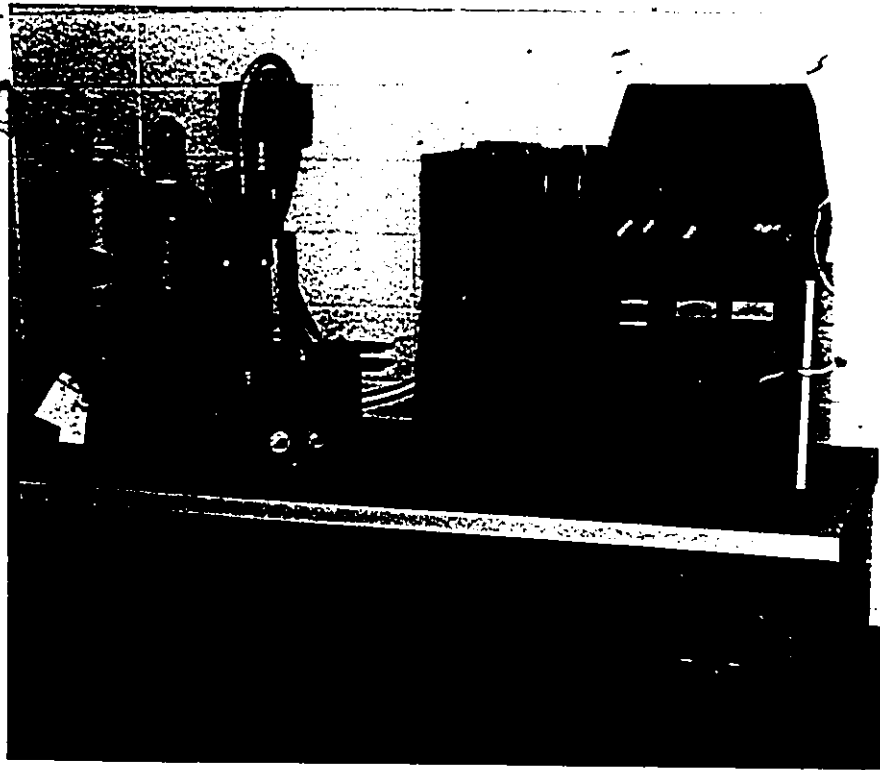
Figure 20: Scanning electron microscope.

$$\nu_0 , (\nu_0 - \nu_1), (\nu_0 + \nu_1)$$
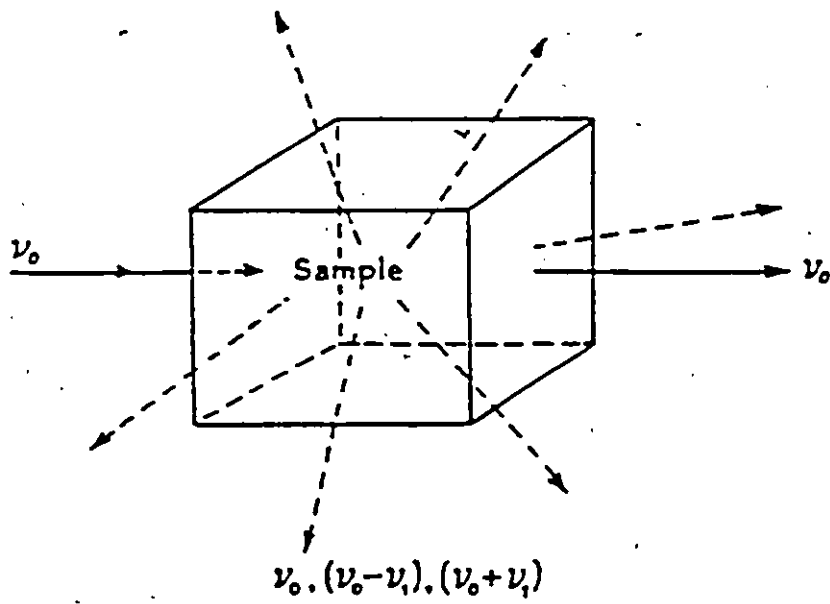
Figure 21: Effect of light passing through a substance.
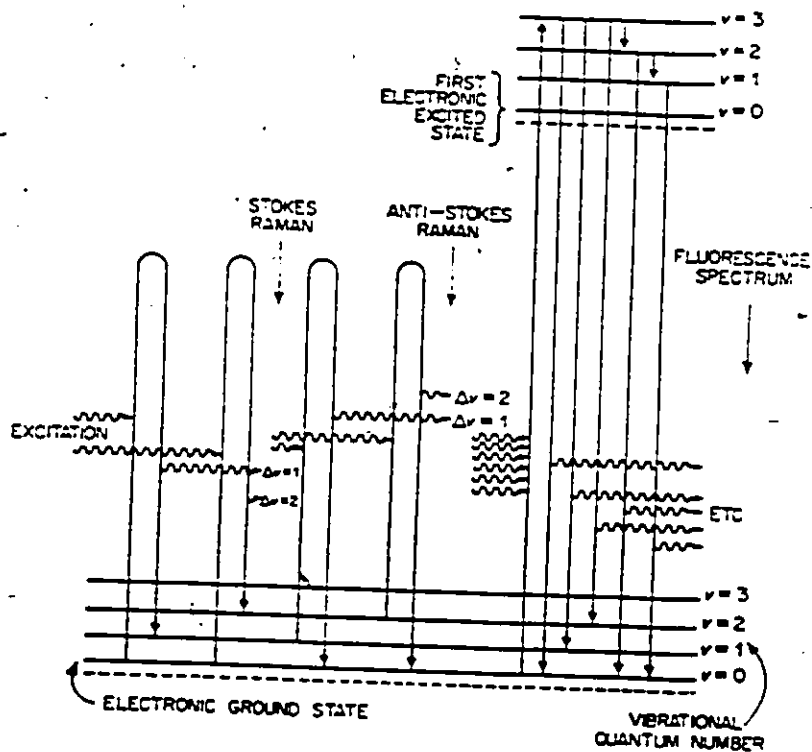
Figure 22: Energy level diagram showing resonant absorption, nonresonant absorption and fluorescence processes.
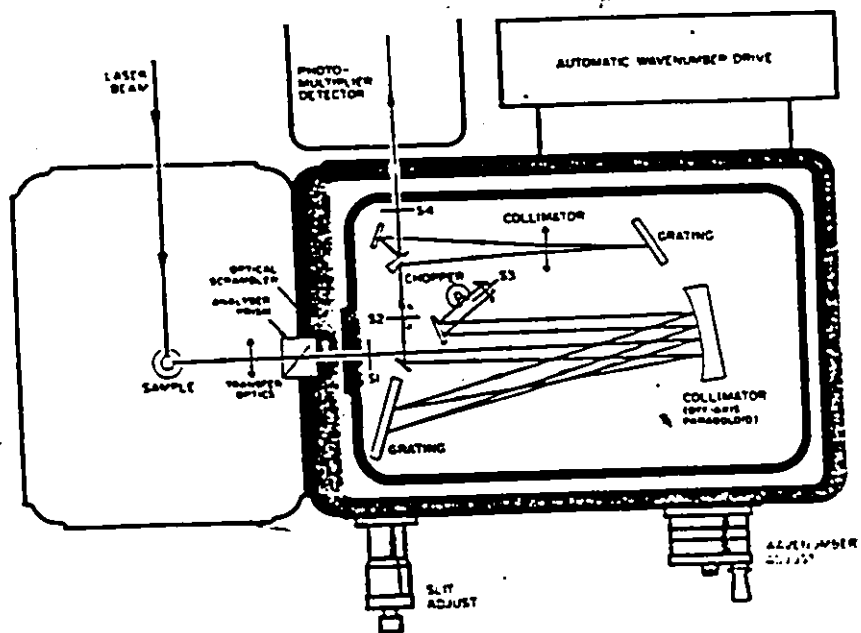
Figure 23: Schematic diagram of a Raman spectrometer.
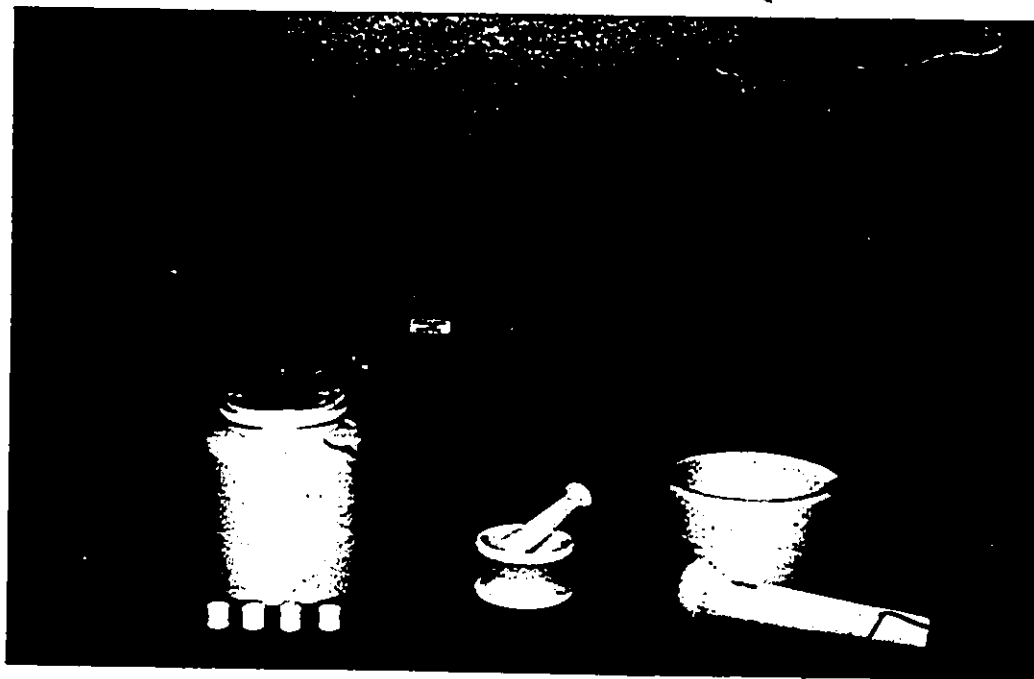
Figure 24: Ball mill and mortar and pestle used for mixing and crushing.
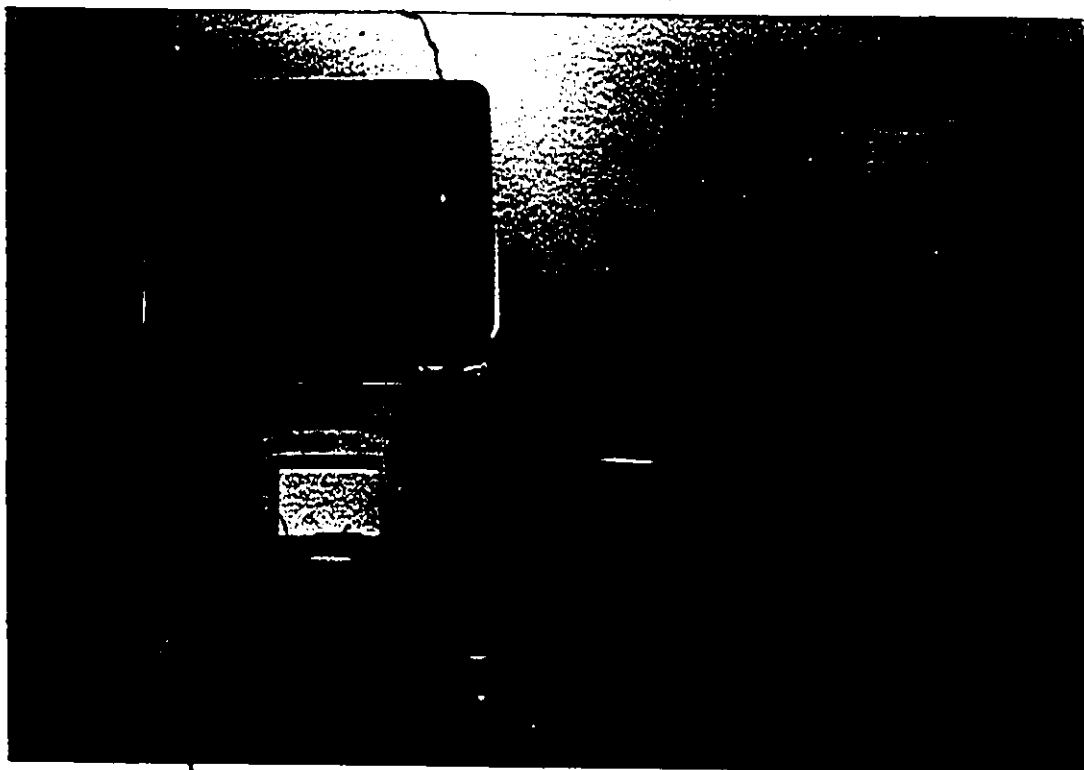
Figure 25: High temperature furnace used to calcinate and sinter ceramic.
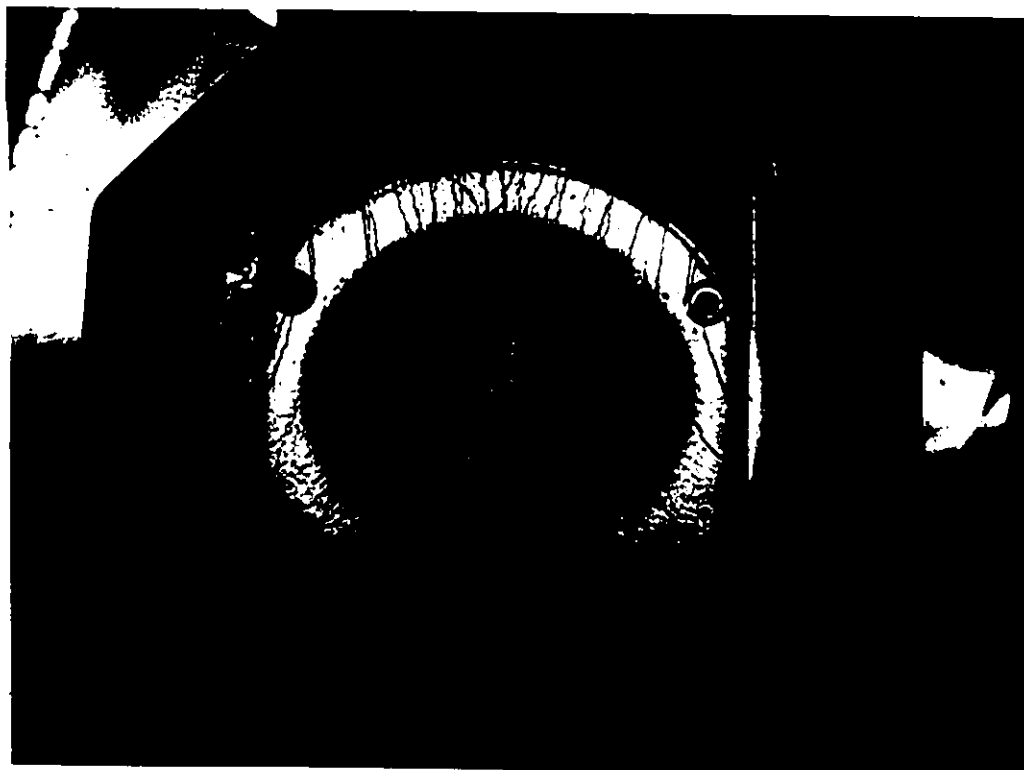
Figure 26: Top view of target area with target in position.
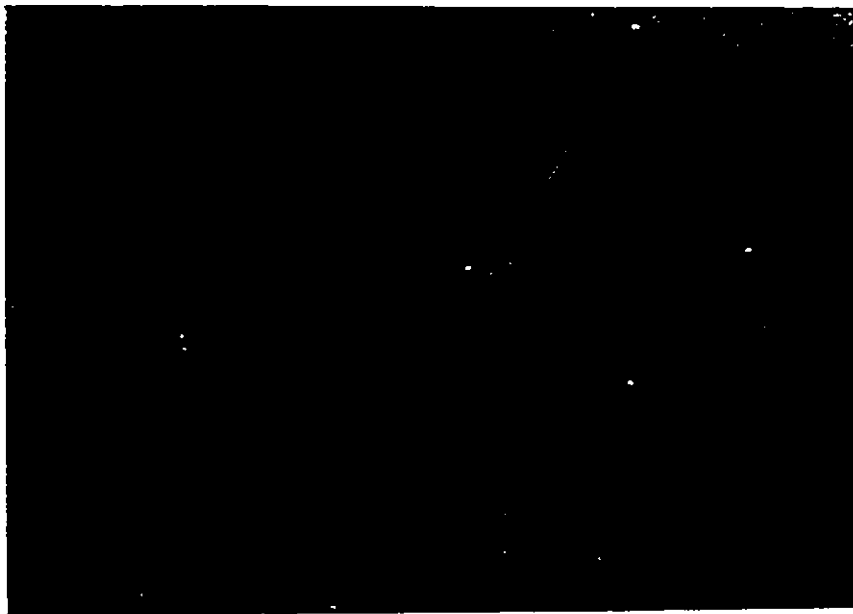
Figure 27: Sintered B2TS2 targets prepared by previous method (left) and modified method (right).
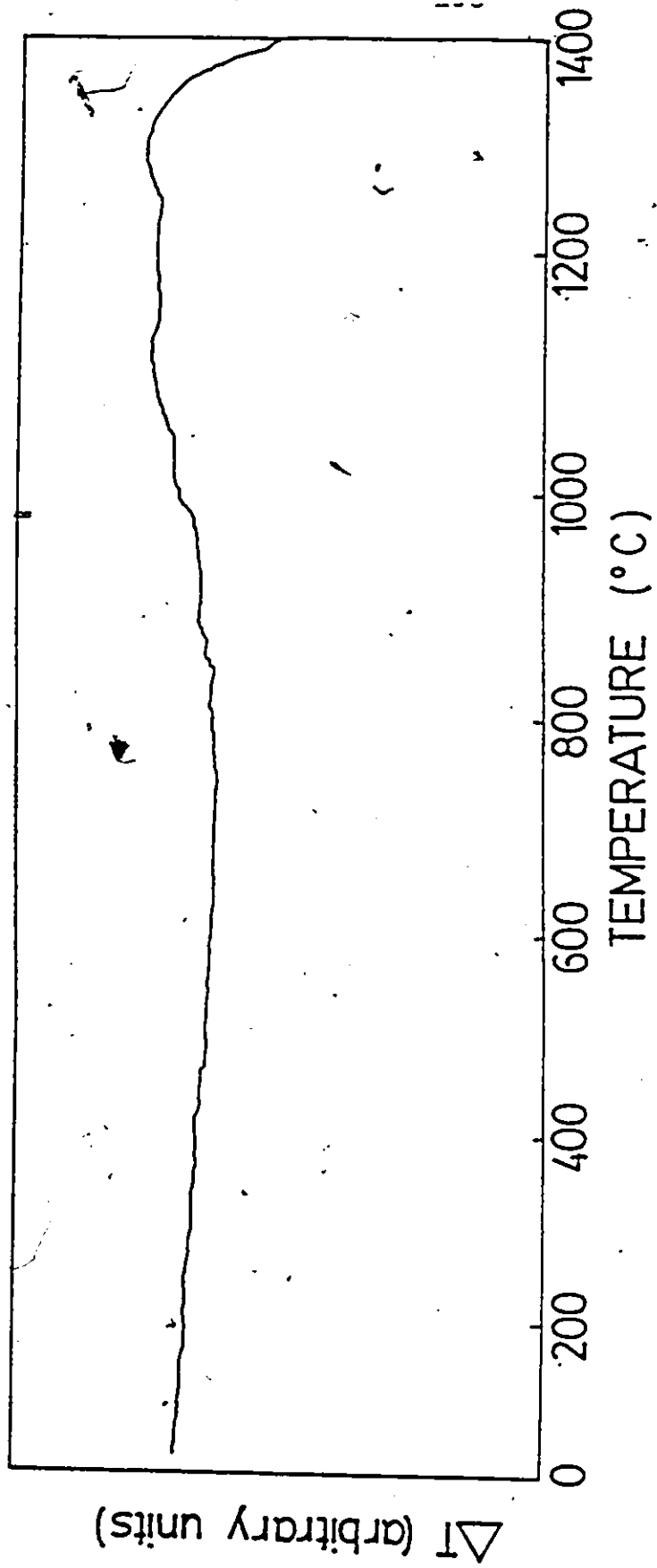
Figure 28: Differential thermal analysis of B2TS2 [50].

(a)

180 μm

(b)

33 μm
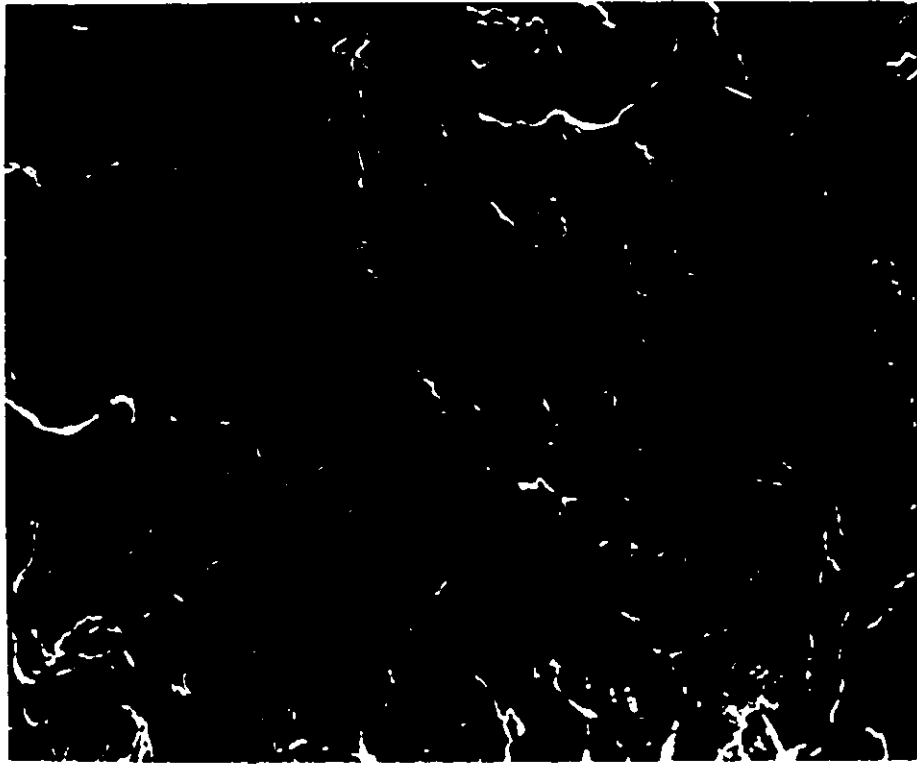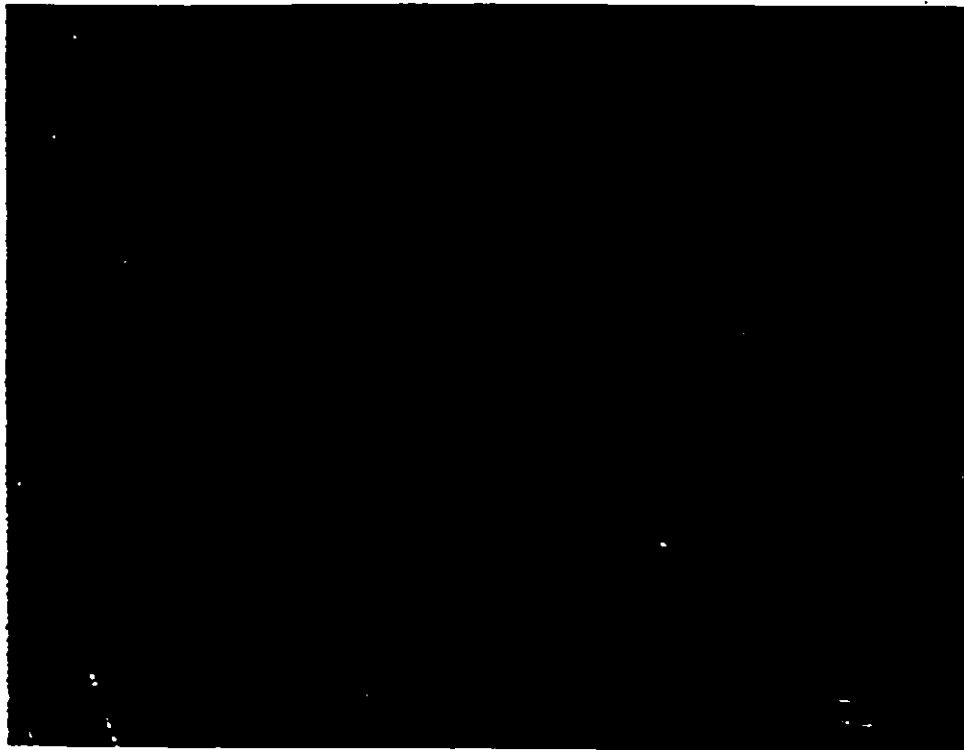
Figure 29: Scanning electron micrographs of B2TS2 ceramics target a) disc surface (550X) and b) fracture surface (3000X) fabricated from previous method.

(a)

180 μm

33 μm
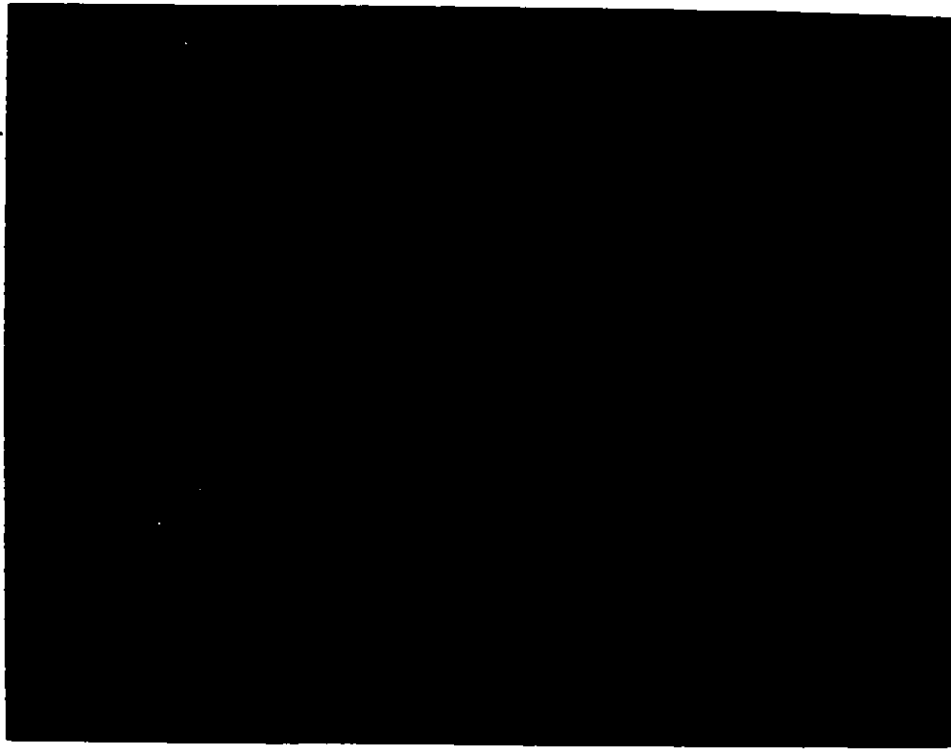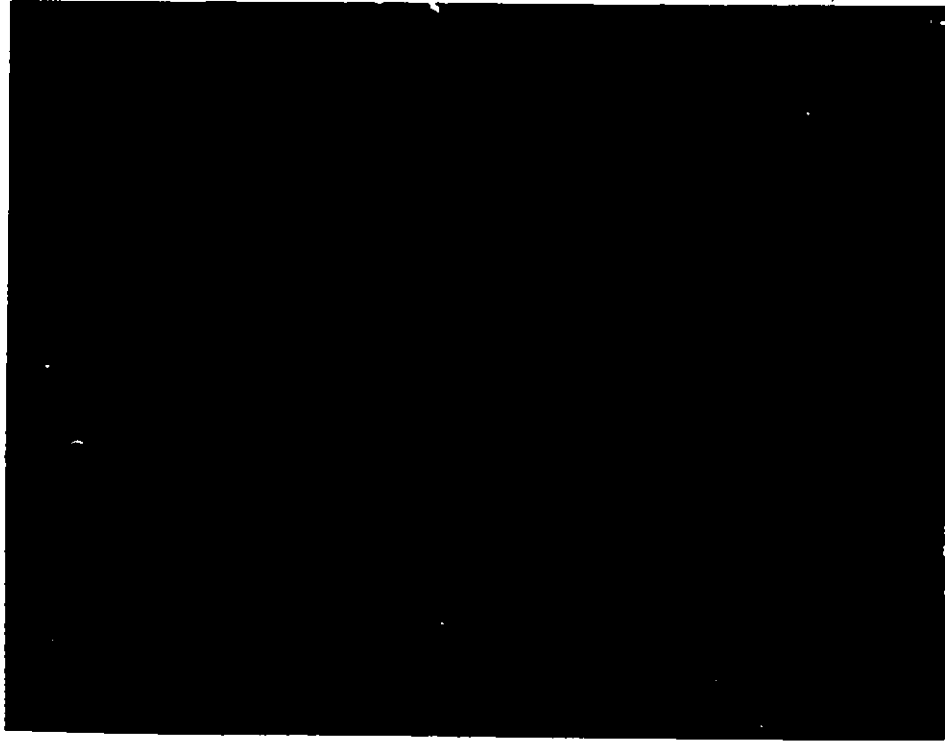
(b)

Figure 30: SEM of modified ceramic target a) disc surface (550X)
and b) fracture surface (3000X) fabricated from the
previous method.
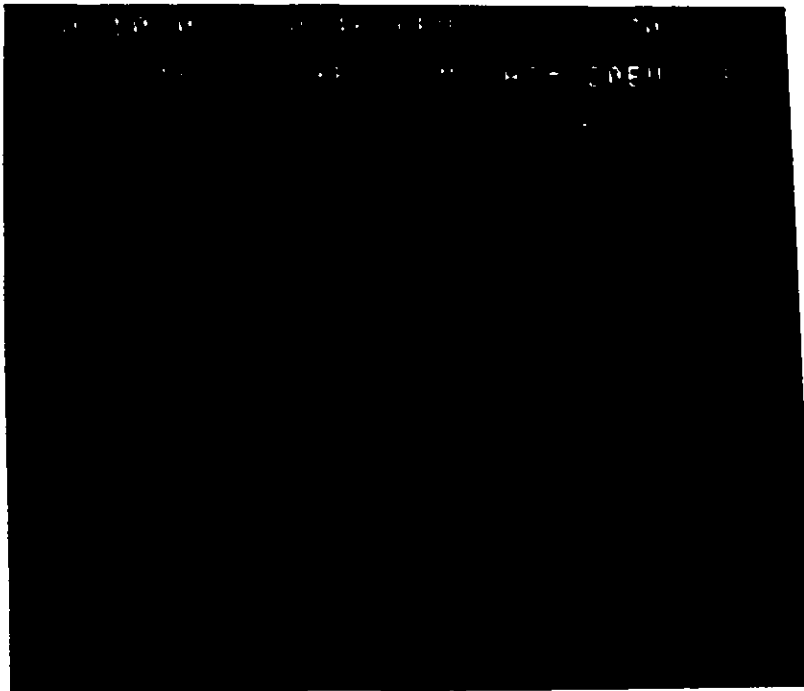
(a)
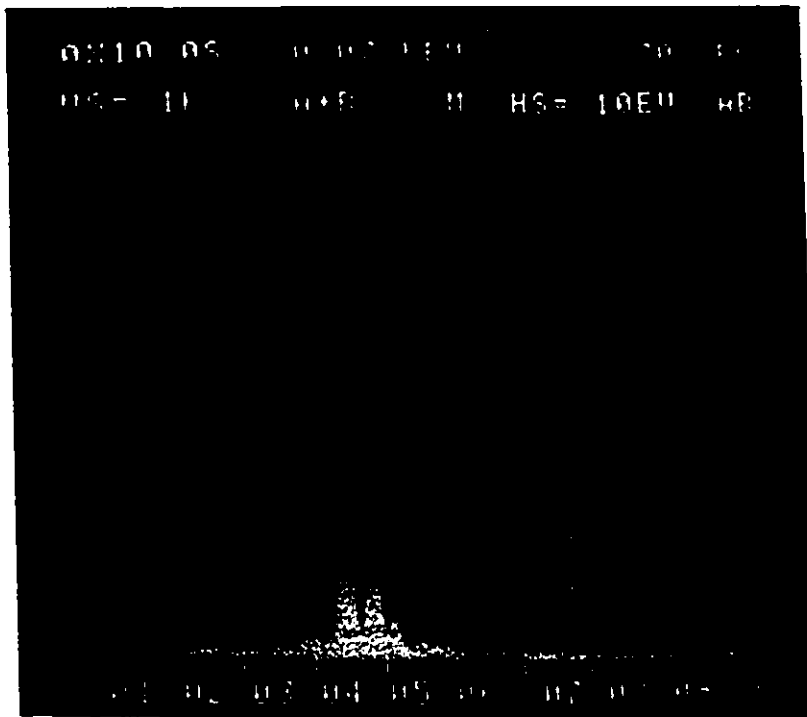
(b)

Figure 31: EDS analysis of a) B2TS2 ceramic target fabricated
by previous method [50] b) B2TS2 ceramic target
fabricated by modified method c) SiO_2 standard
d) $BaTiO_3$ standard e) TiO_2 standard and f) $BaCO_3$
standard.
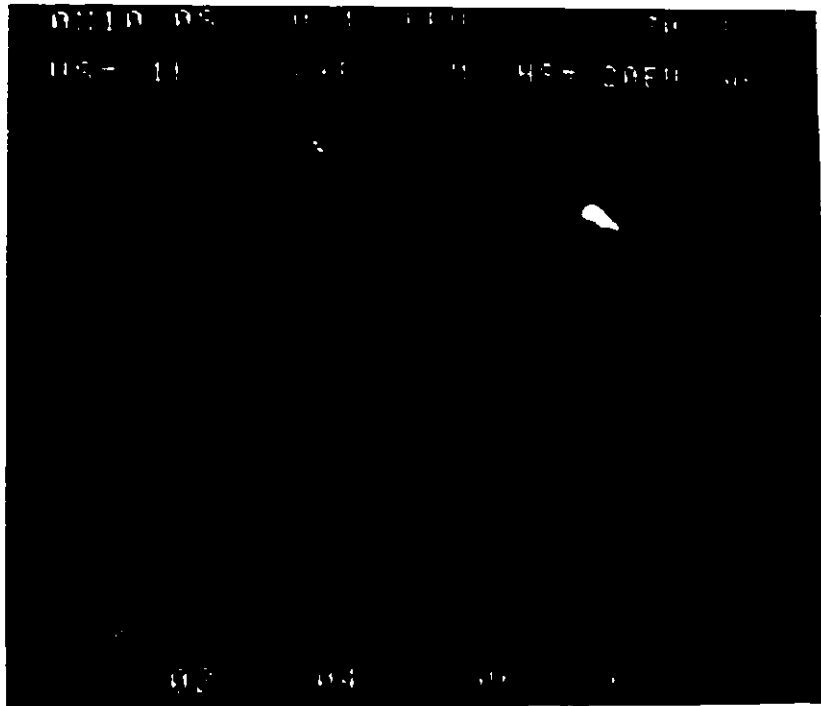
(c)
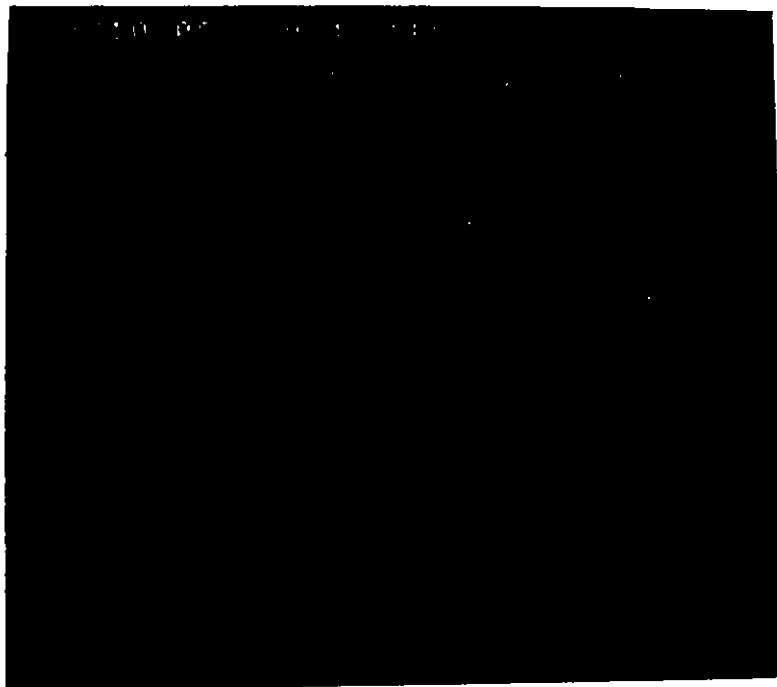
(d)
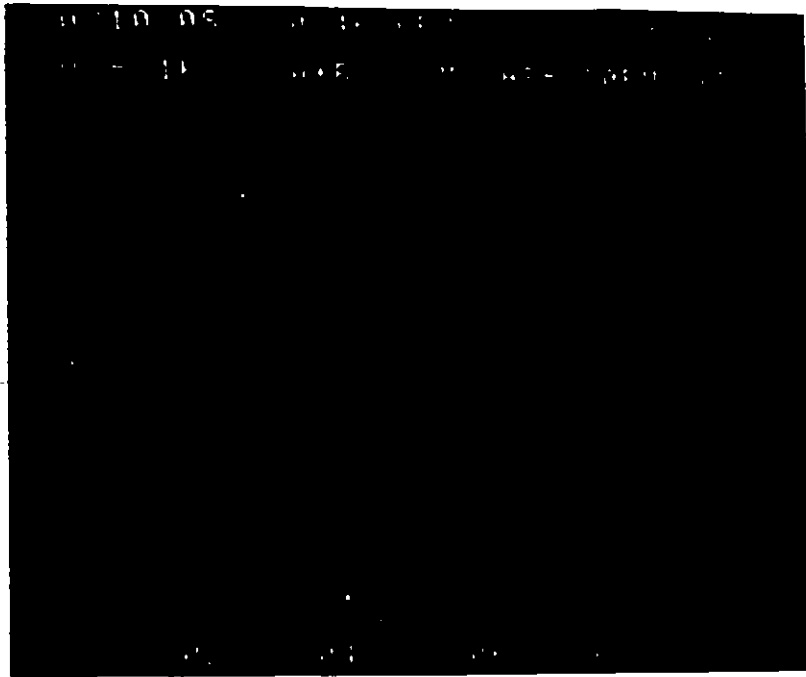
(e)
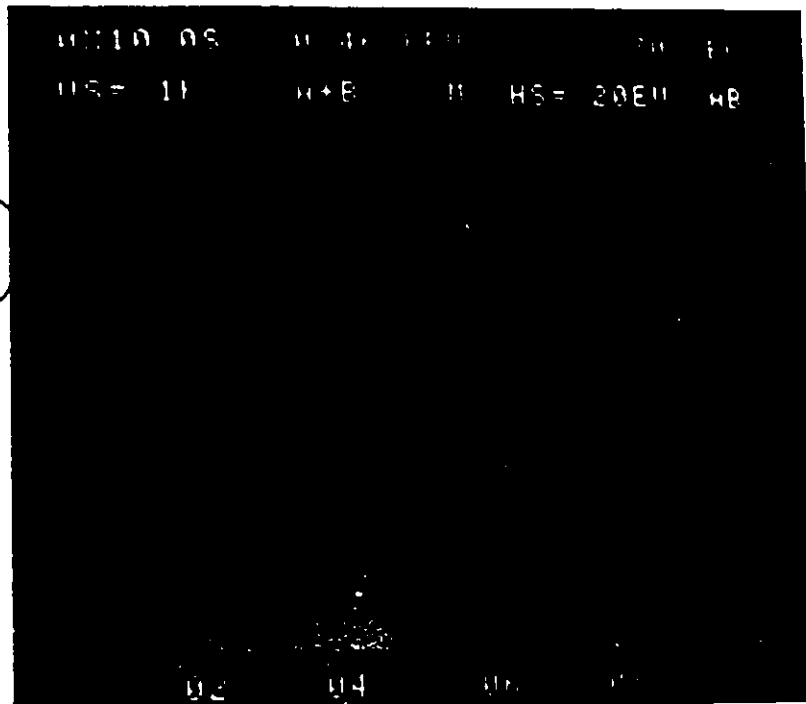
. (f)
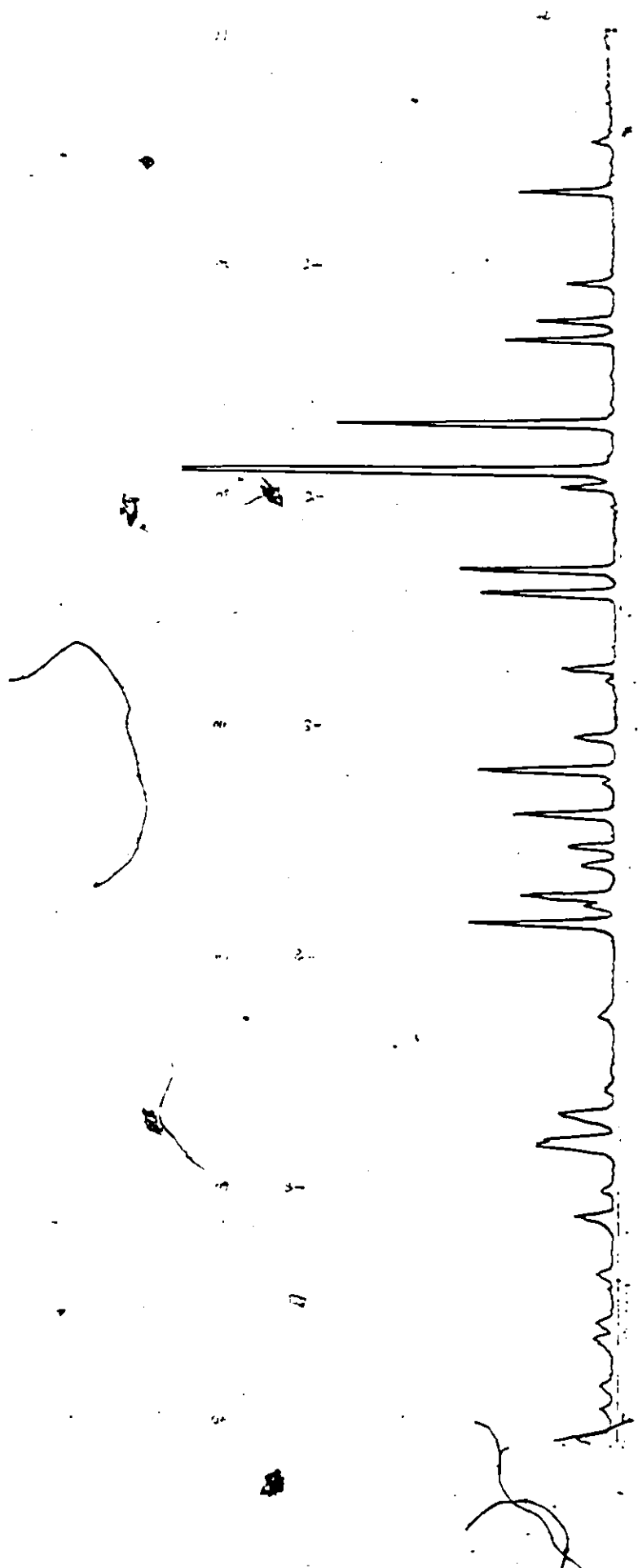
Figure 32: XRD pattern of B2TS2 ceramic target fabricated using the previous method (Appendix B).
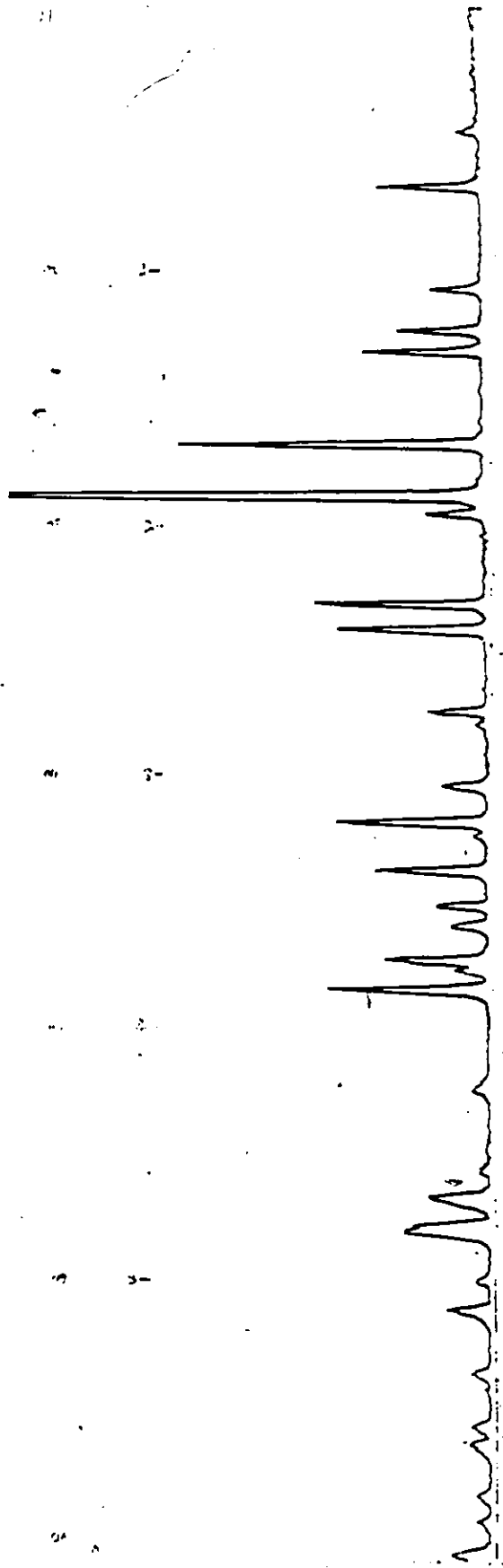
Figure 33: XRD pattern of B2TS2 ceramic target fabricated using the modified method (Section 4.1).
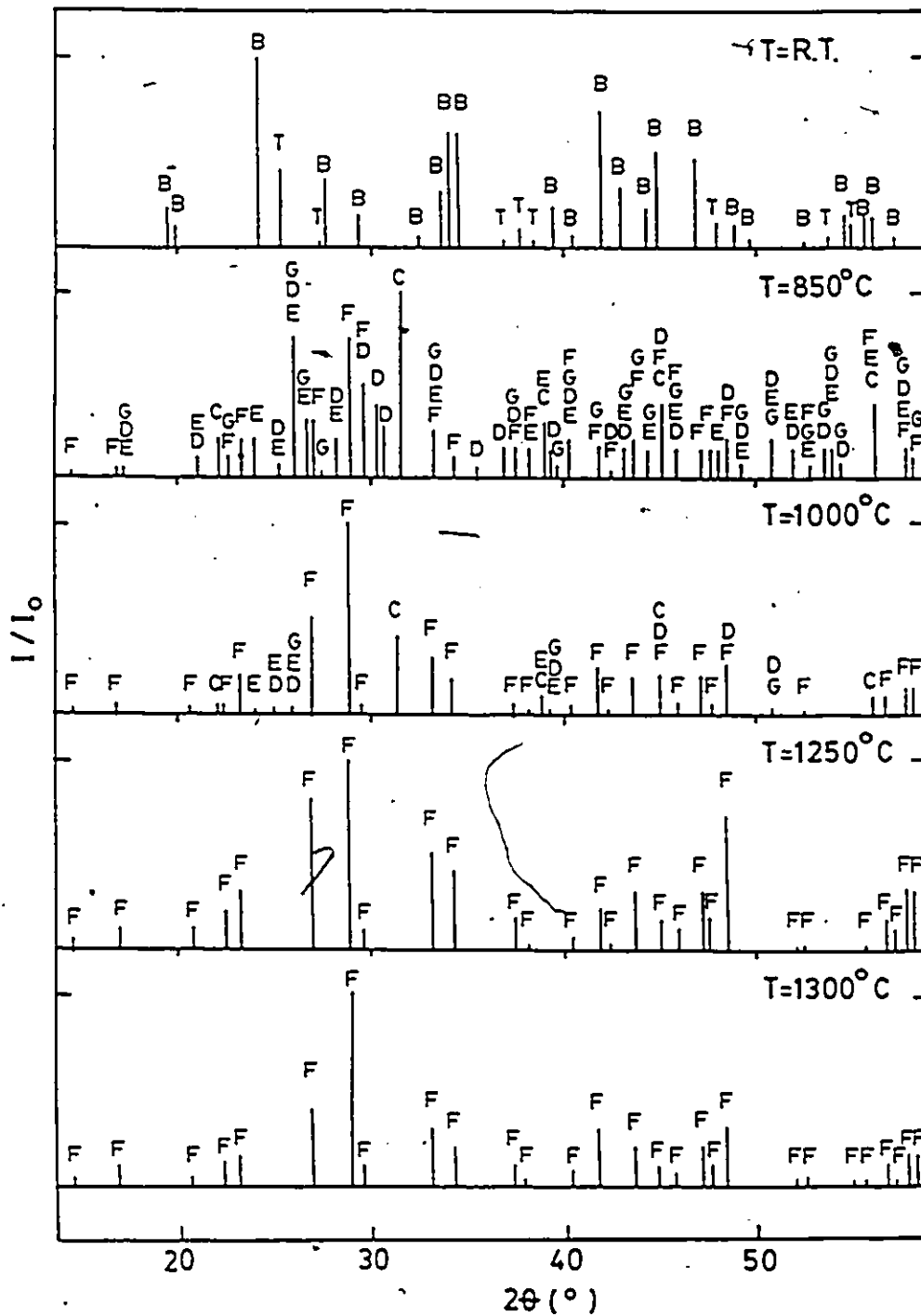
Figure 34: X-ray diffraction patterns, when CuK$_\alpha$ radiation was utilized of the mixture of fine powders of BaCO$_3$, TiO$_2$ and SiO$_2$ with Ba:Ti:Si ratios of 2:1:2 which were heated as indicated.
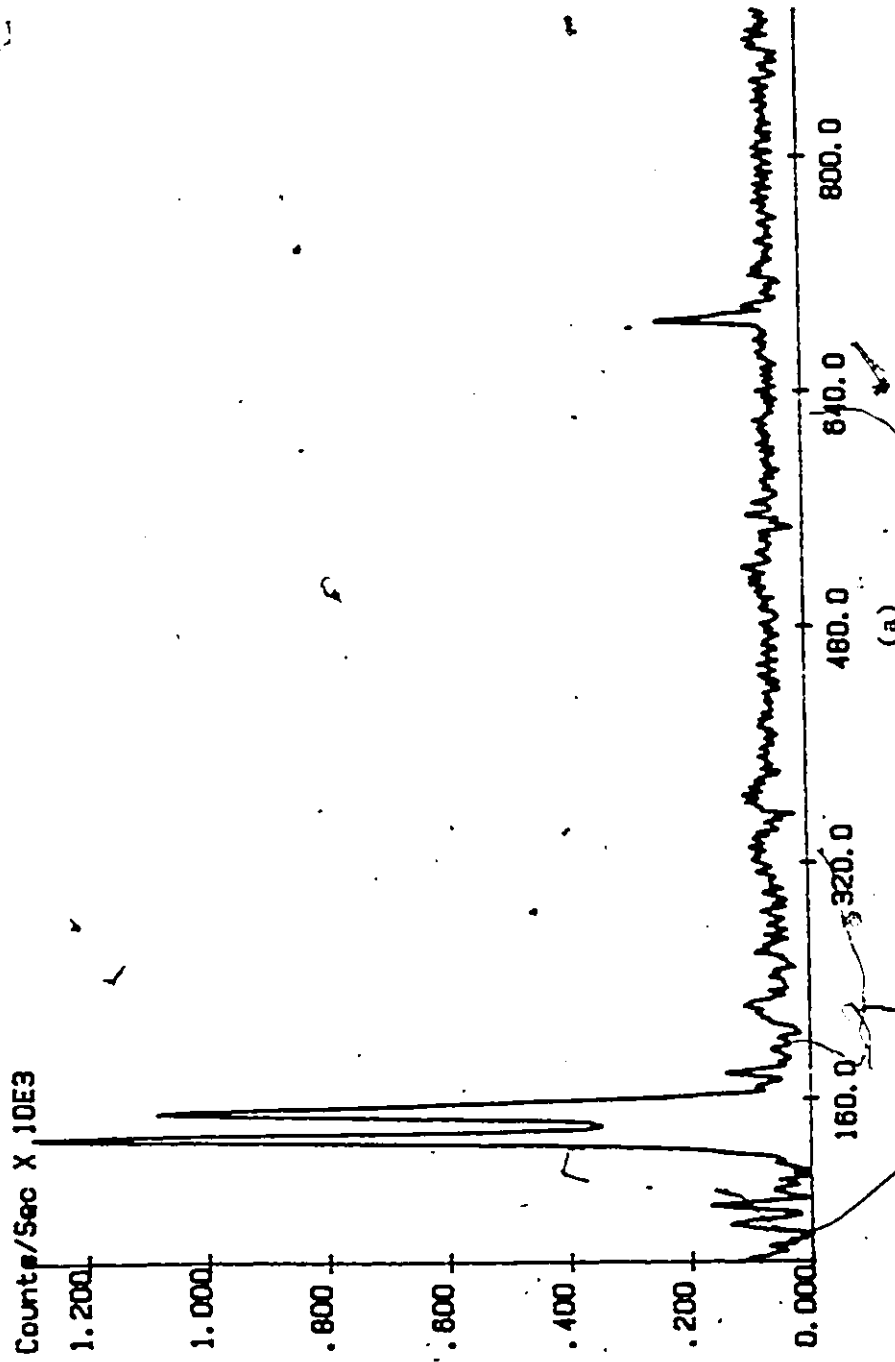
Figure 35: Raman spectroscopy results of a) Ba(l)$_3$ b) TiO$_2$ (anatase) [87]
c) silica gel d) BaO, and ceramic powder (Ba:Ti:Si of 2:1:2)
e) just mixed f) 1300°C for 114 hours g)sputtering target.

(b)

Counts/Sec X 10E2

2.400

2.200

2.000

1.800

1.600

1.400

160.0   320.0   480.0   640.0   800.0

(c)

Counts/Sec X 10E3

(d)

(e)

(f)

Counts/Sec X 10E2

(B)
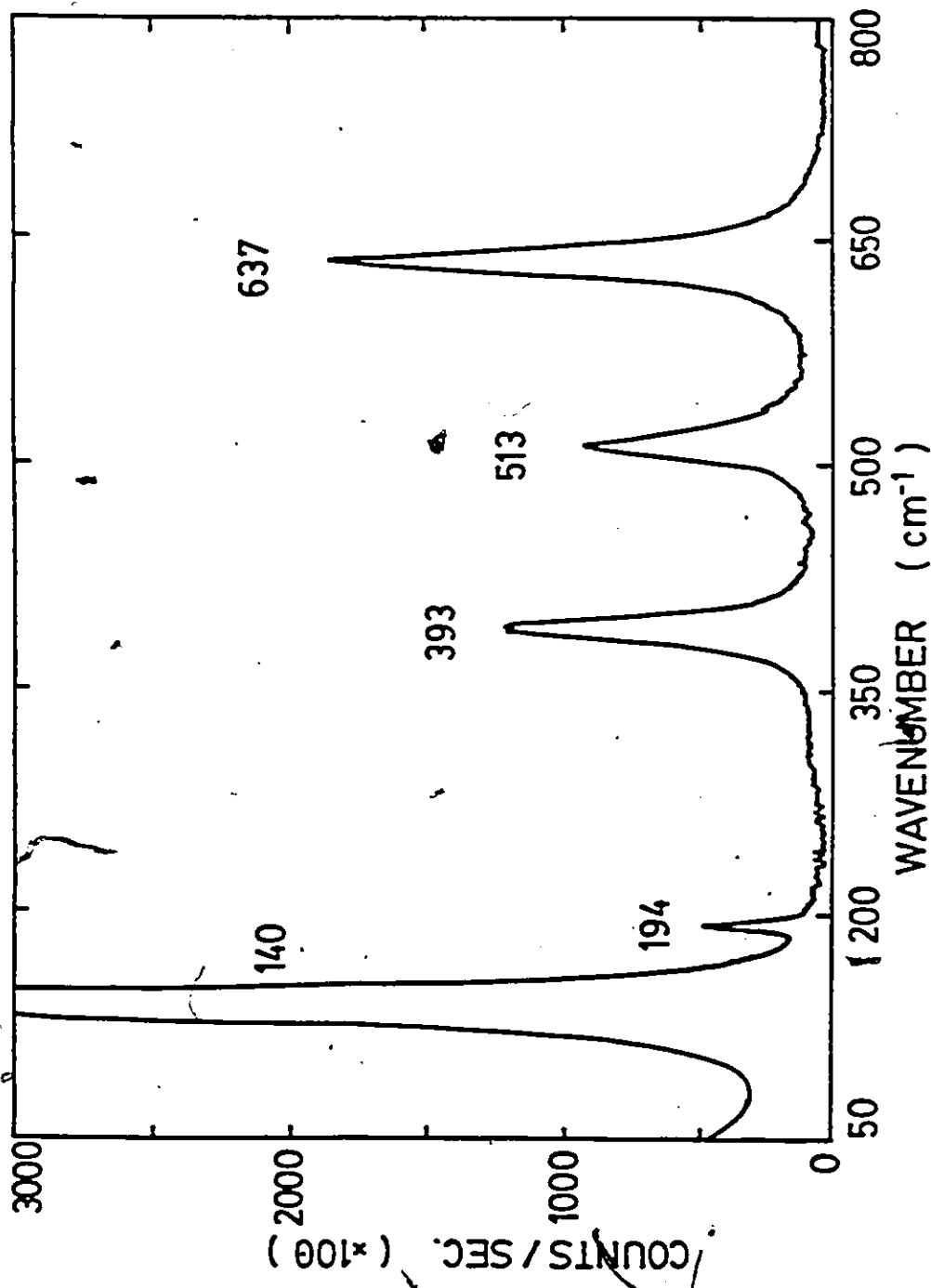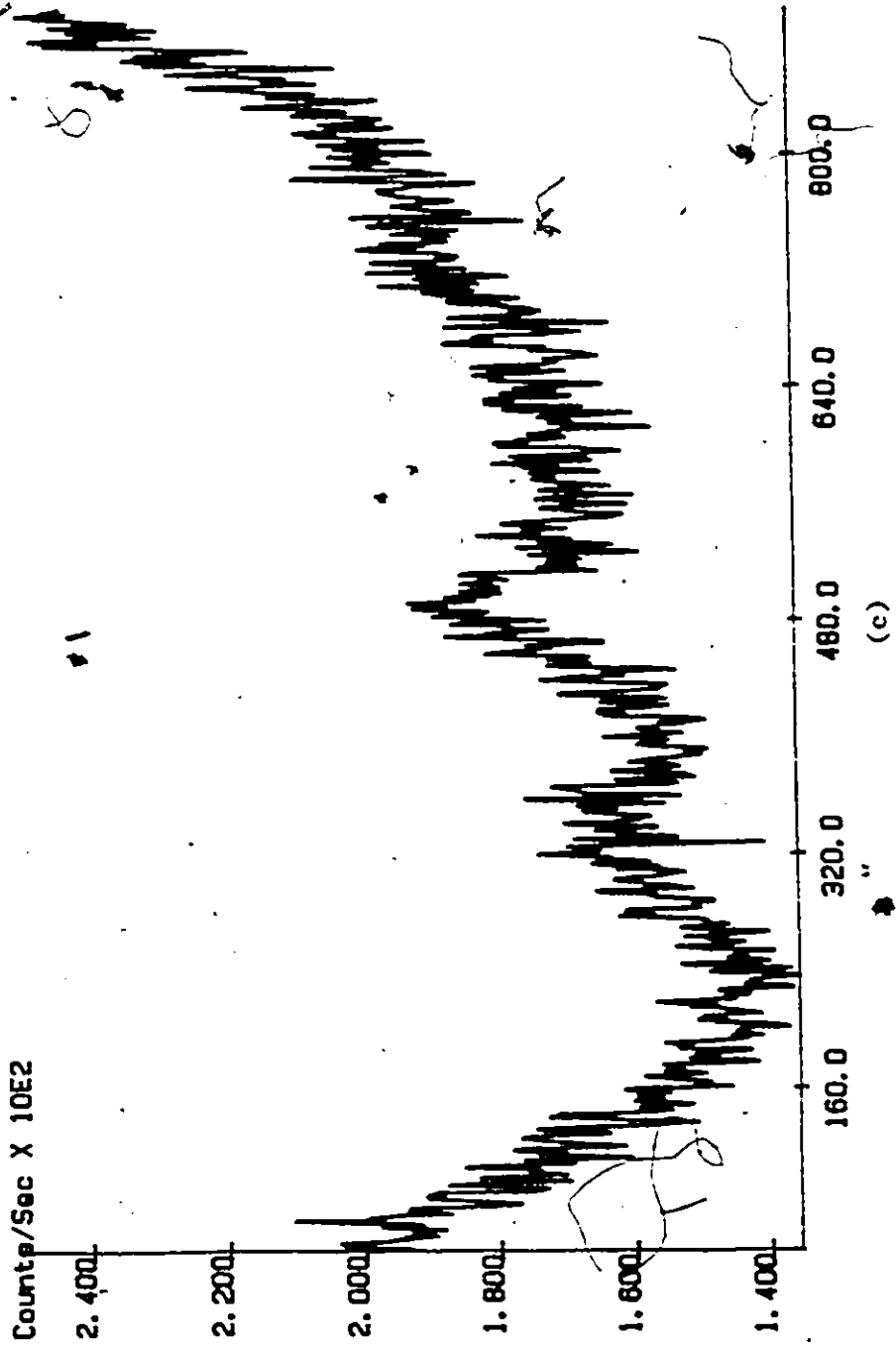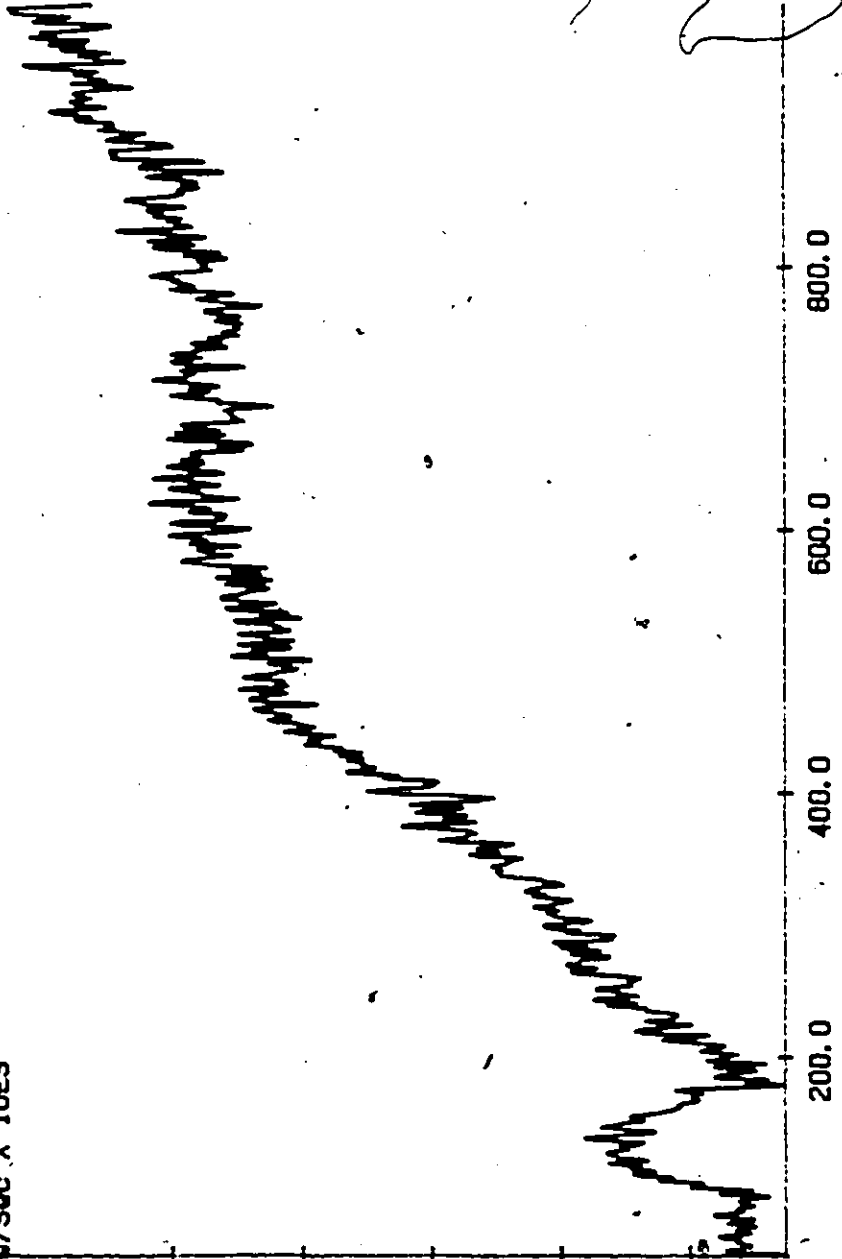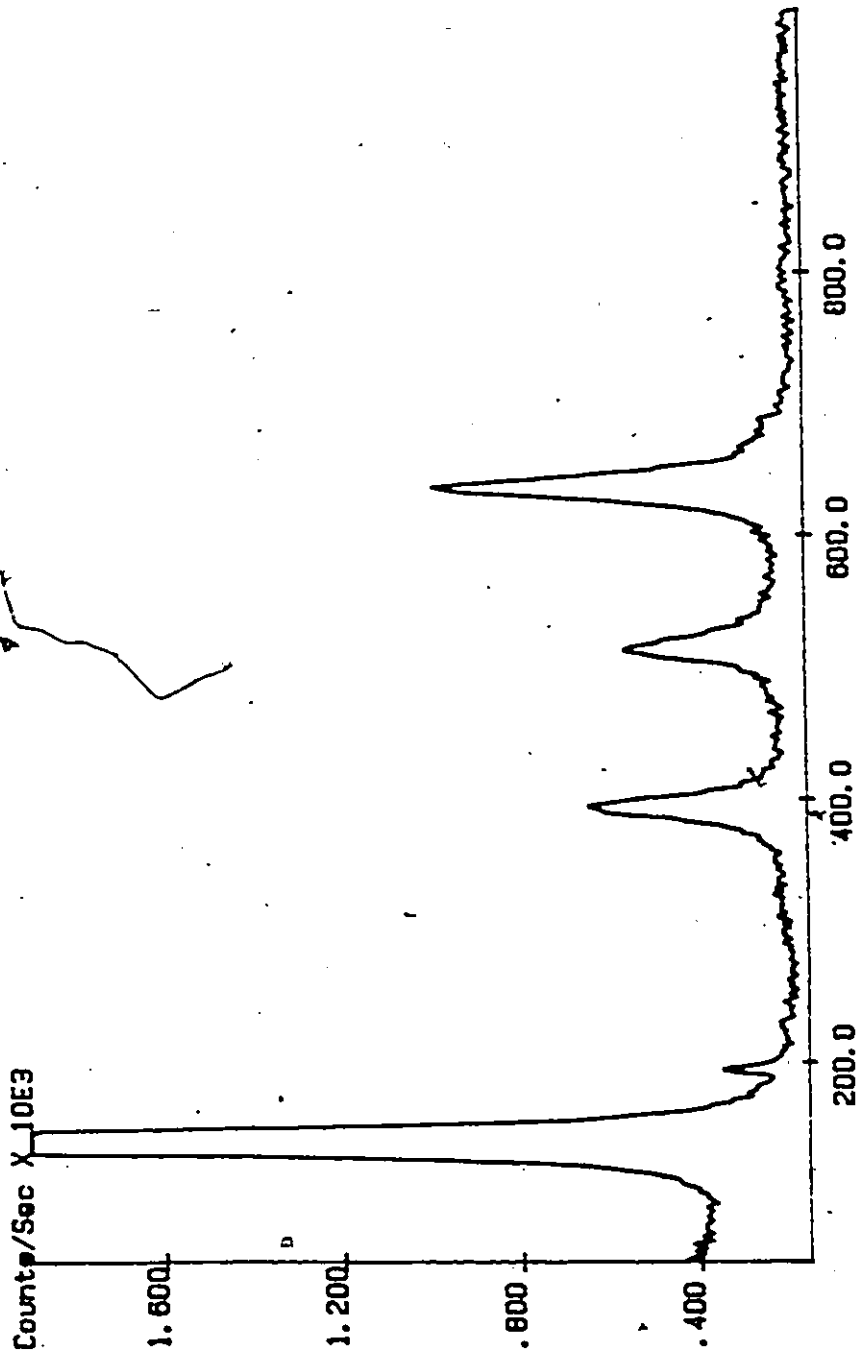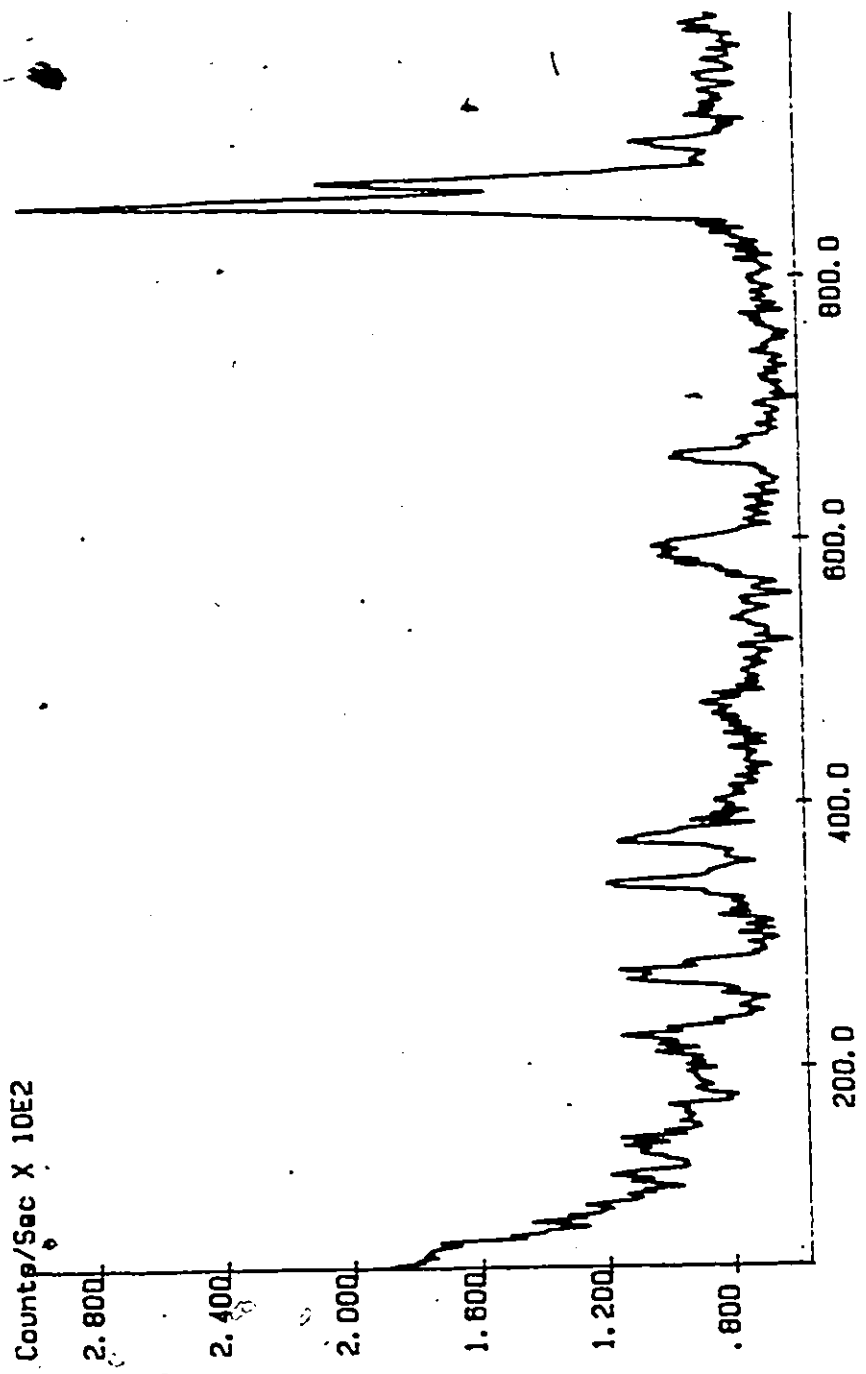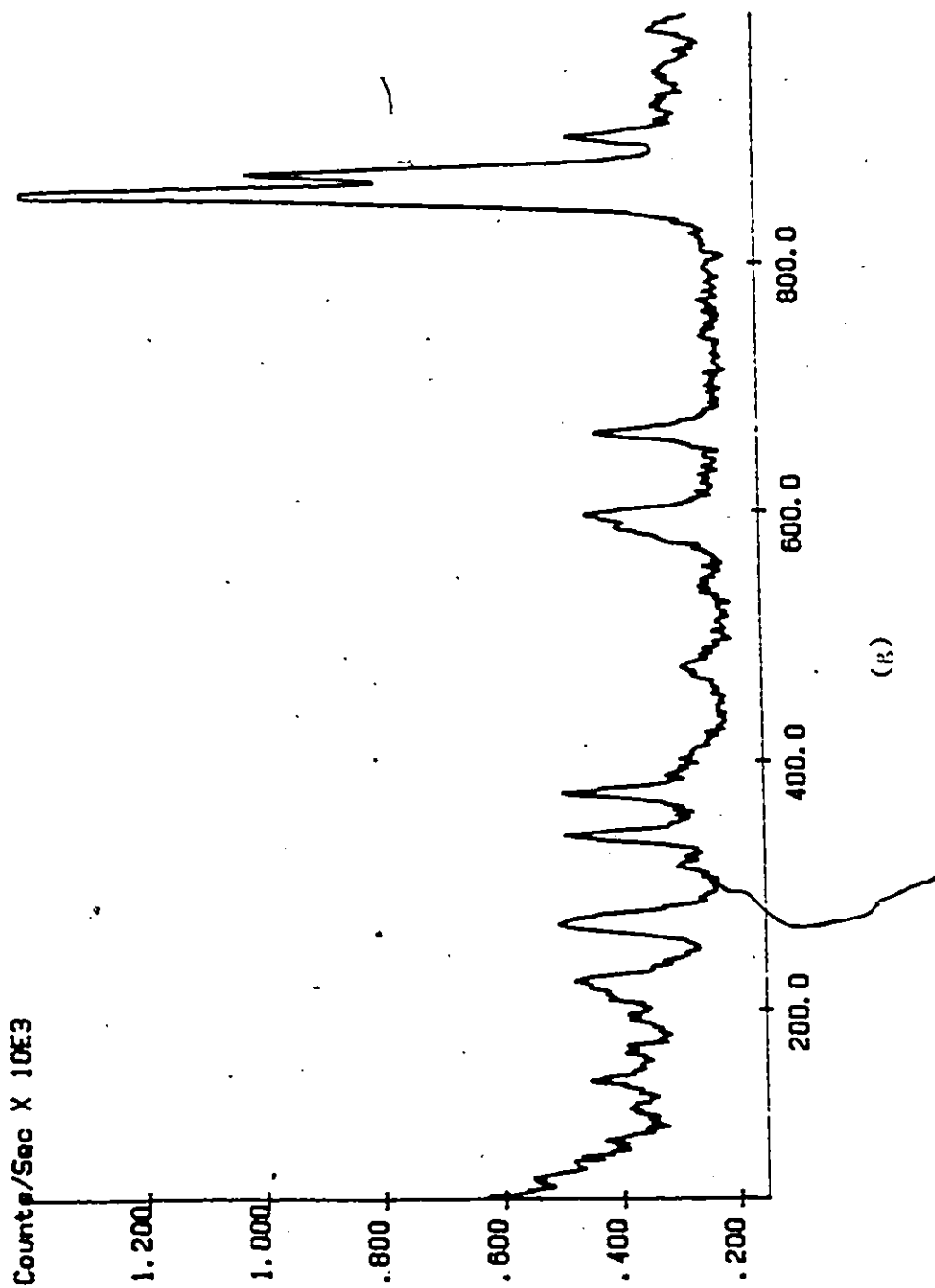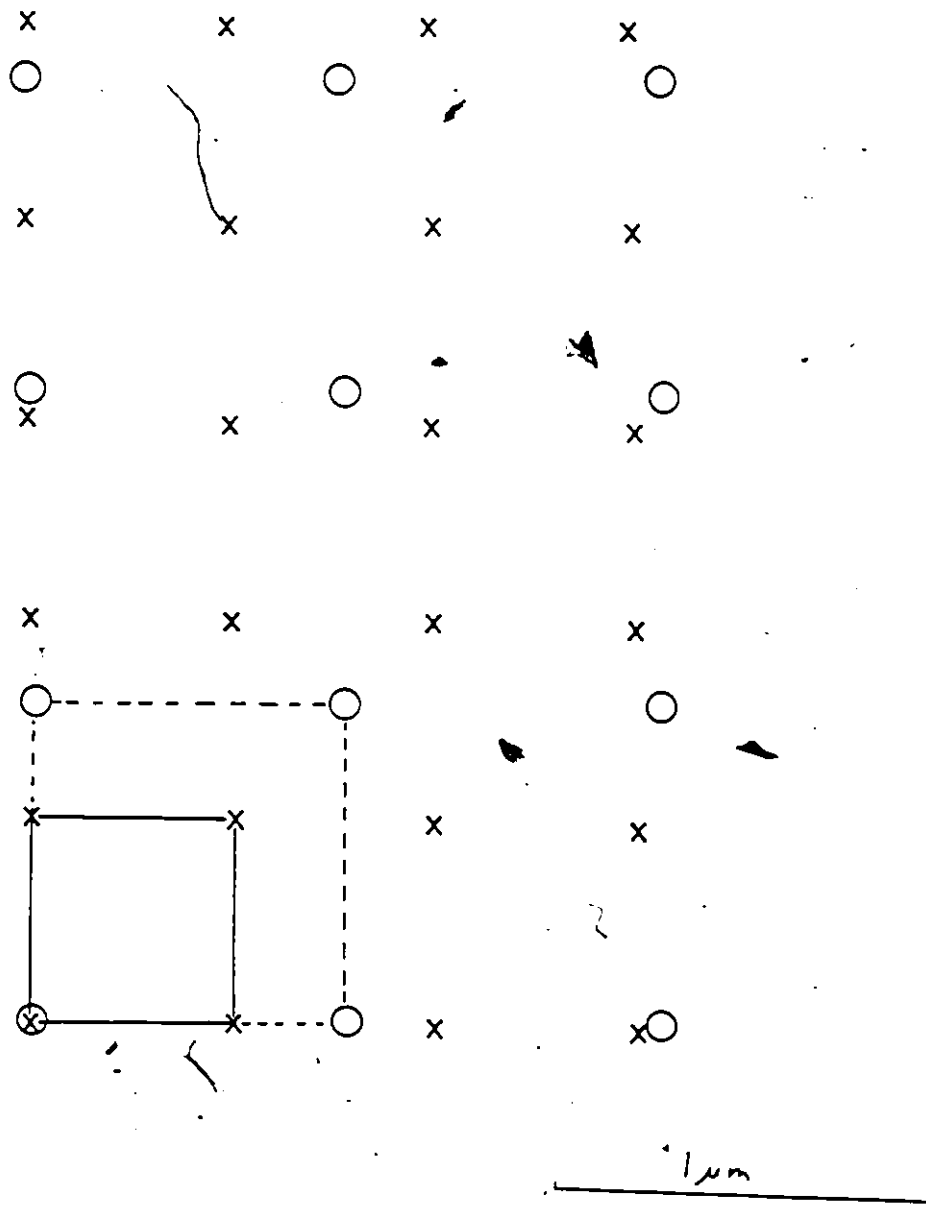
Figure 36: Unit cell match-up of Si (x) and B2TS2 (o) in the (001) plane.

Figure 37: XRD pattern of B2TS2 thin film deposited on (100)Si at 650°C.

250 μm
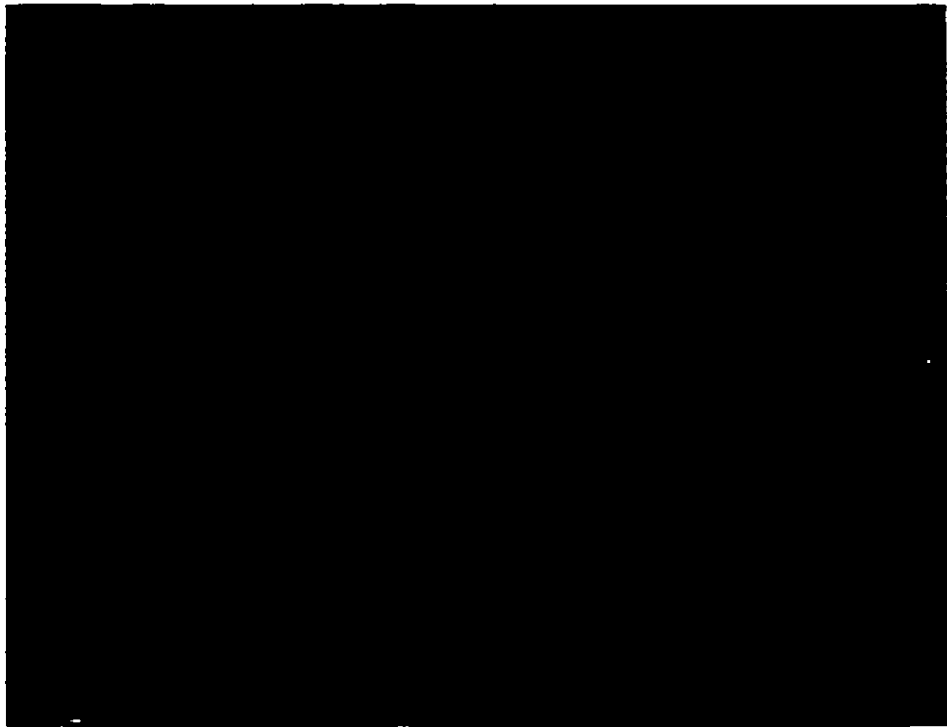
Figure 38: Optical micrograph of B2TS2 thin film
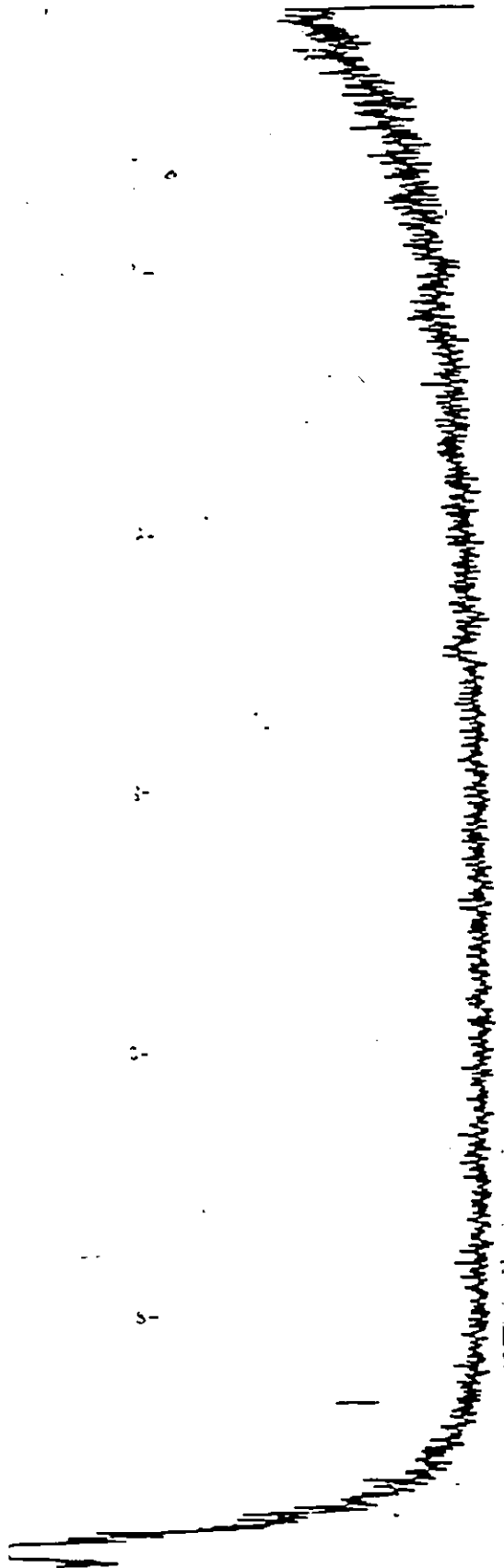deposited on (100)Si at 650°C (400X).
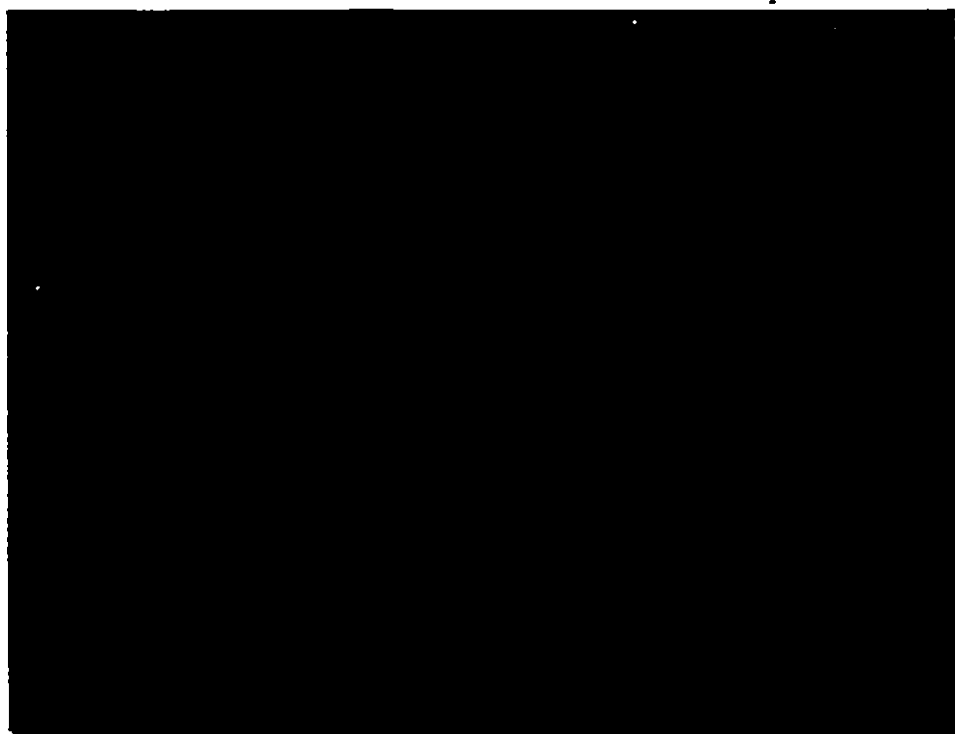
250 μm

Figure 33. Optical micrograph of B2TS2 thin film deposited on (100)Si at 200°C for 24 hours (400X).
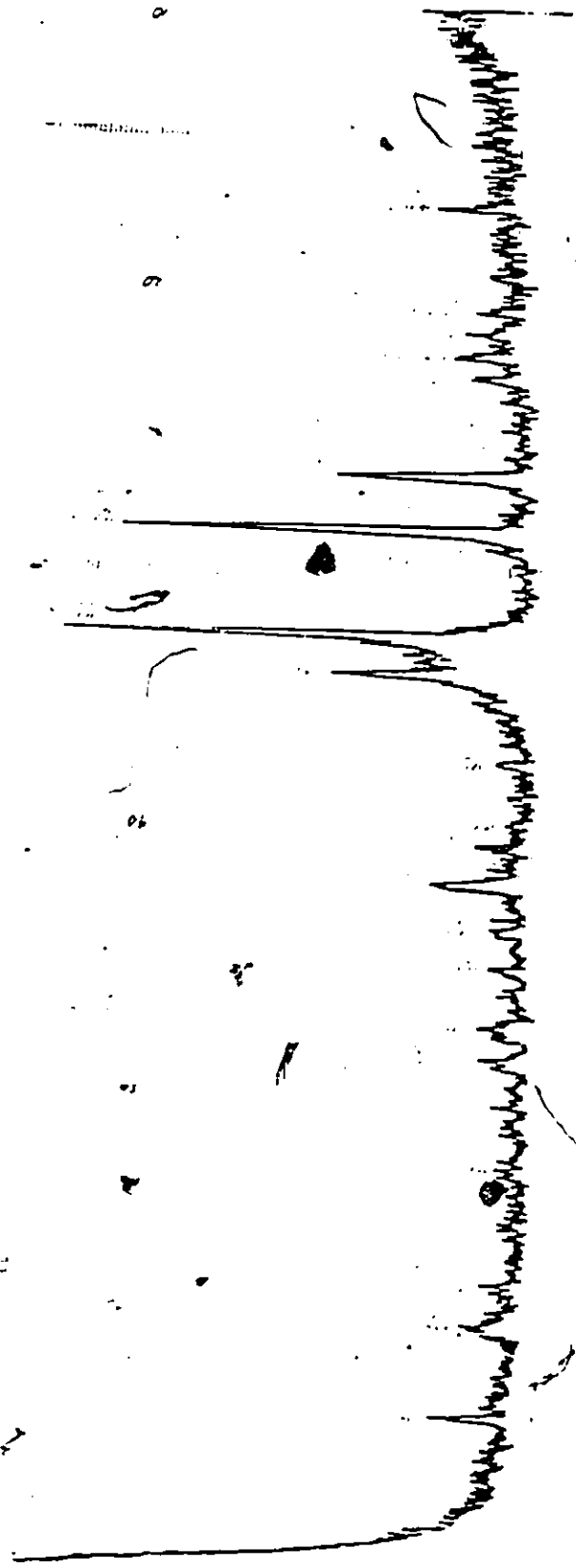
Figure 40: XRD pattern of B2TS2 thin film deposited on (100)Si at 800°C.
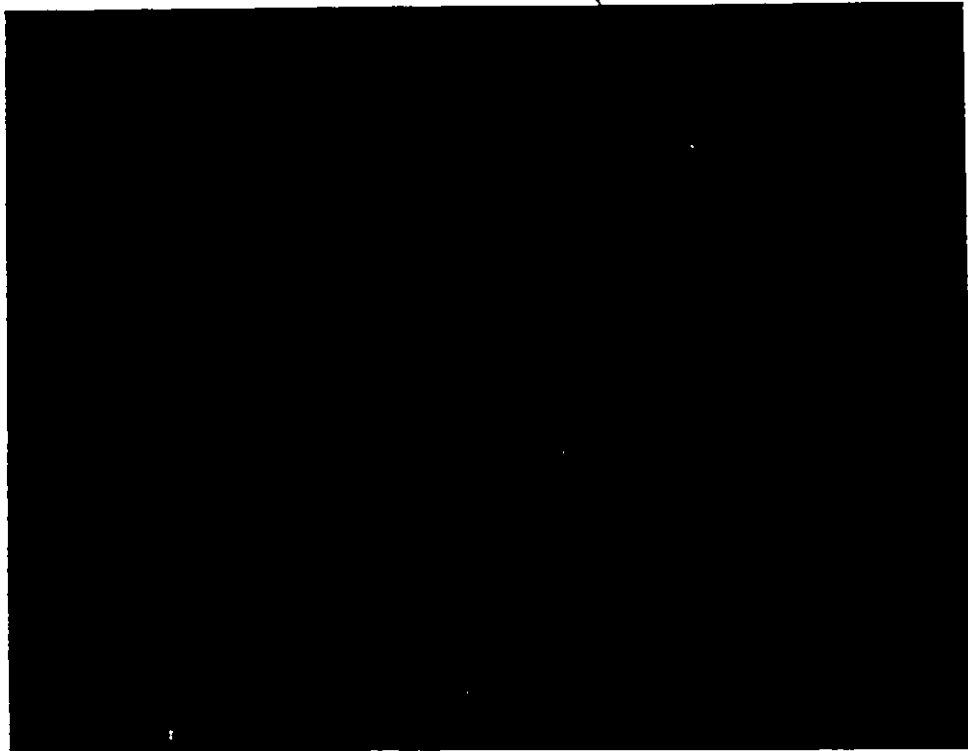
250 μm

Figure 41: Optical micrograph of B2TS2 thin film deposited on (100)Si at 800°C for 5 hours (400X).
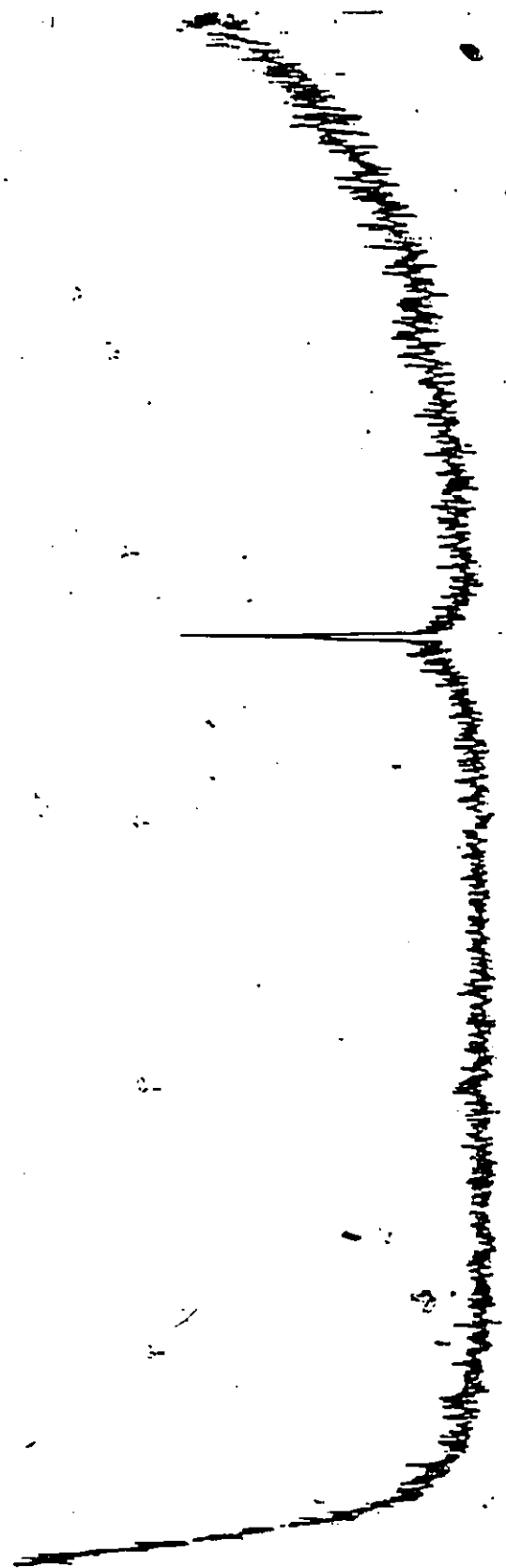
Figure 42: XRD patterns of B2TS2 thin films deposited at:
a) 675°C for 6 hours
b) 700°C for 6 hours
c) 725°C for 7 hours
d) 750°C for 7 hours
e) 775°C for 8 hours

(a)

42 (b)

42 (c)

42 (d)

42 (e)

(a)

Figure 43: Inverse pole figures of:
a) B2TS2 JCPDS standard (card no. 22-513) and
B2TS2 thin films deposited on (100)Si at:
b) 700°C for 6 hours
c) 725°C for 7 hours
d) 750°C for 7 hours
e) 775°C for 8 hours
f) 800°C for 5 hours

110

5

7.60

001

100
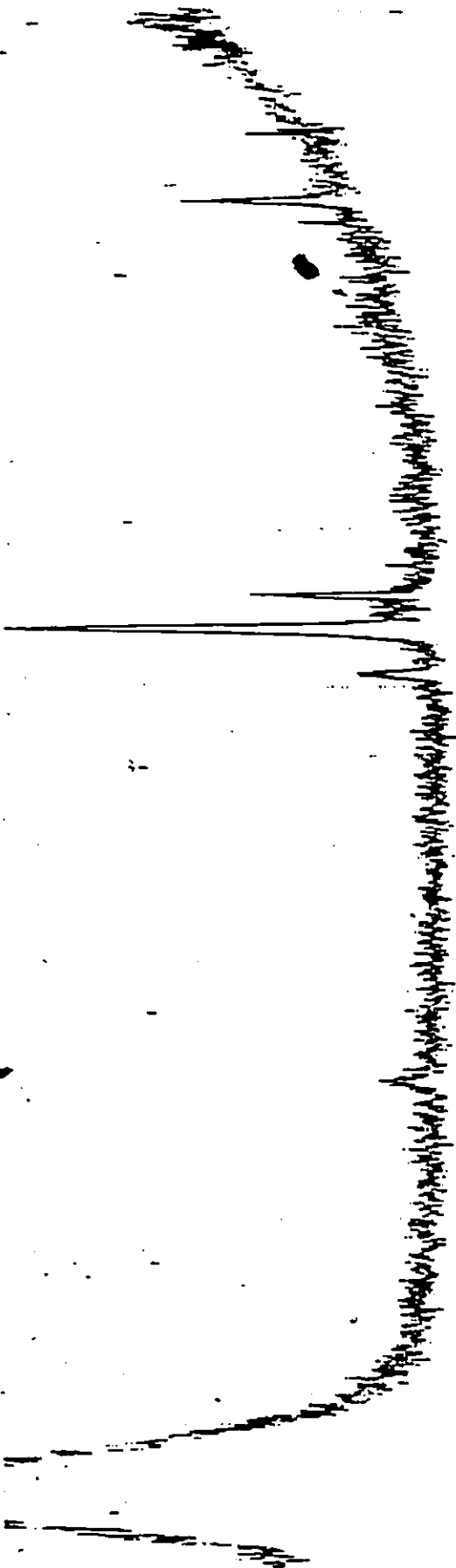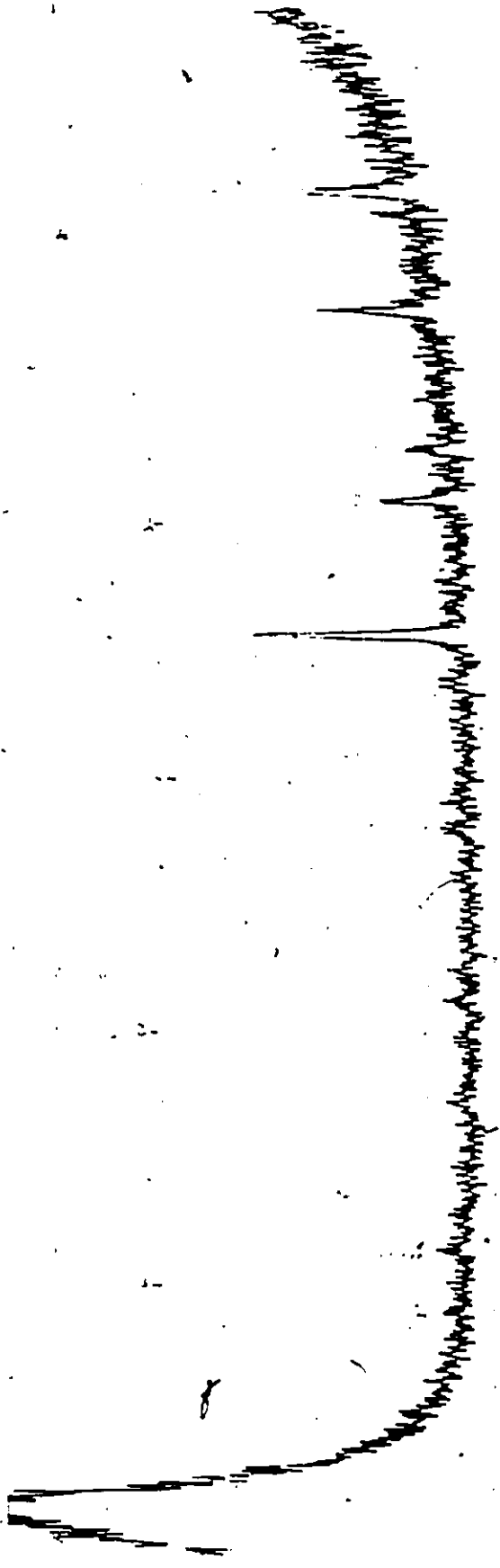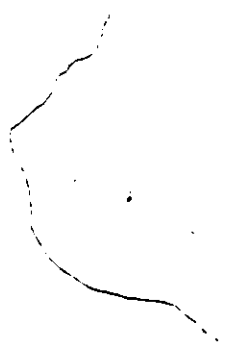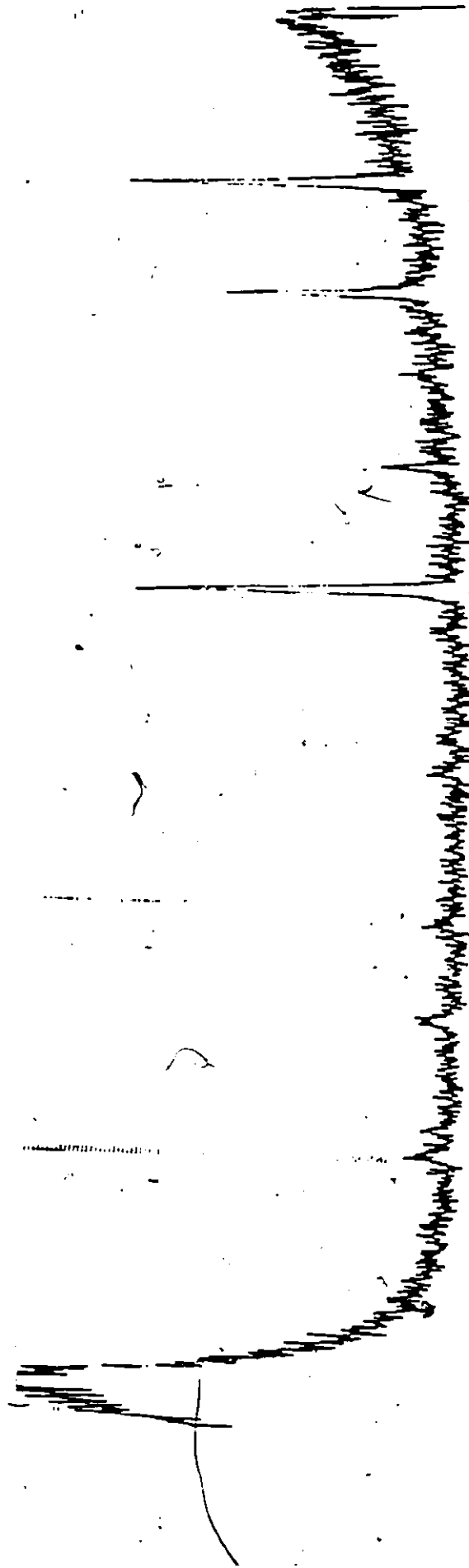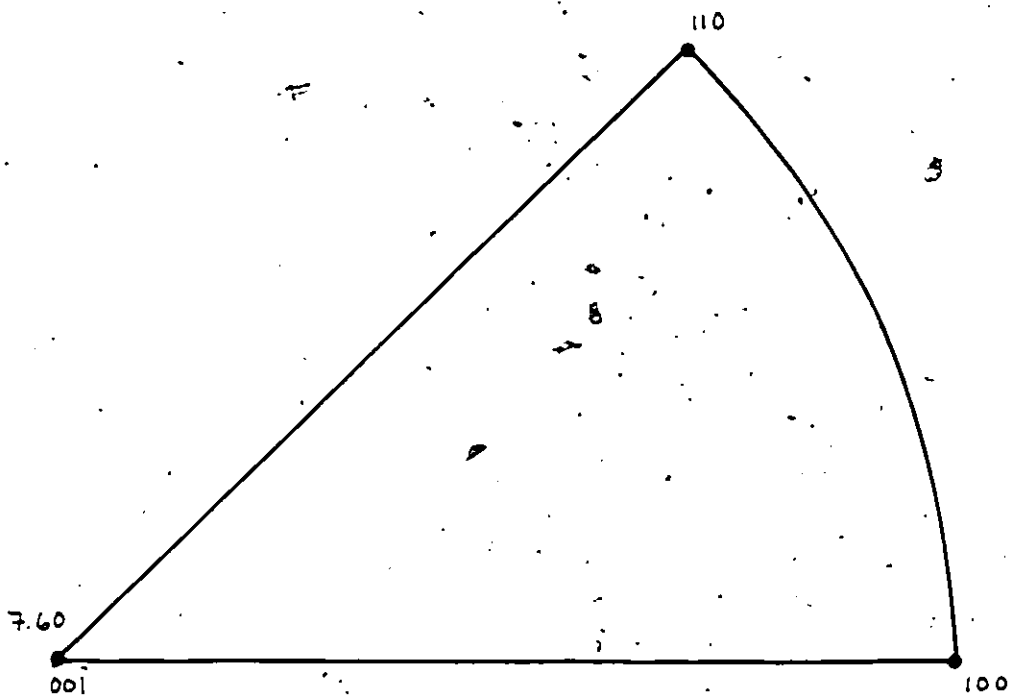
43 (b)

43 (c)

43 (d)

43 (e)

43 (f)
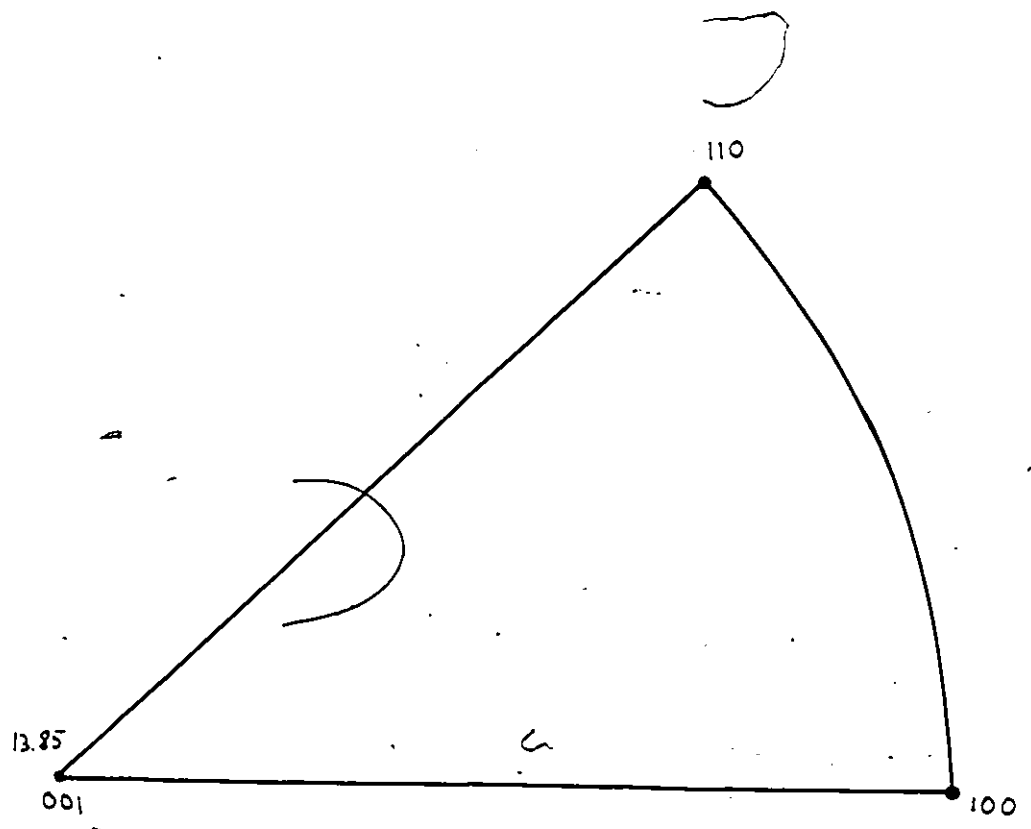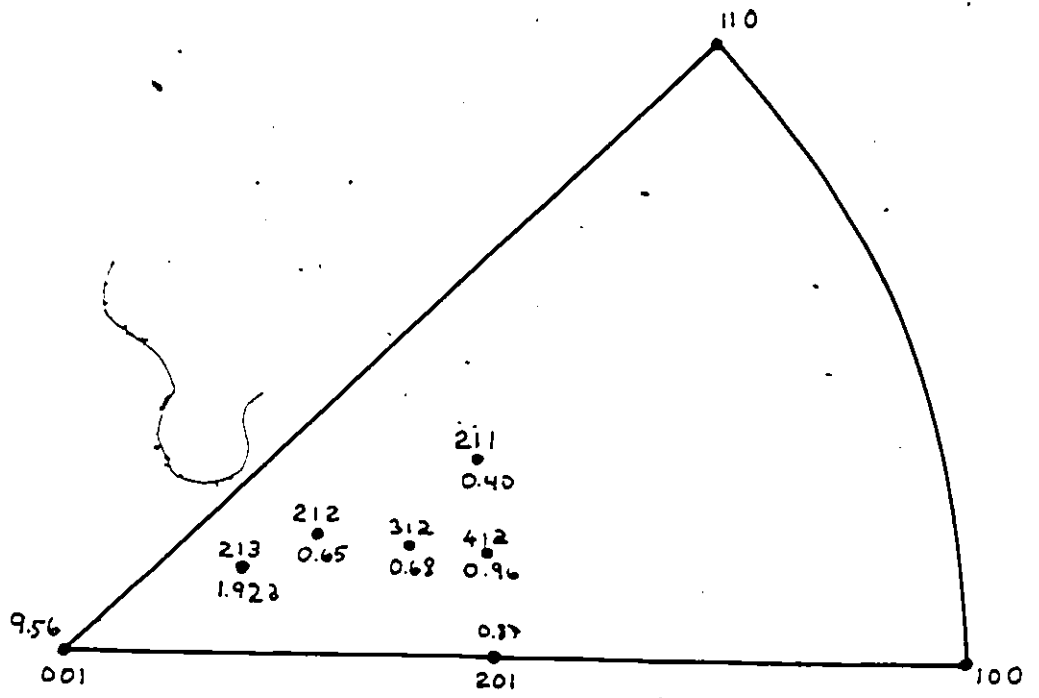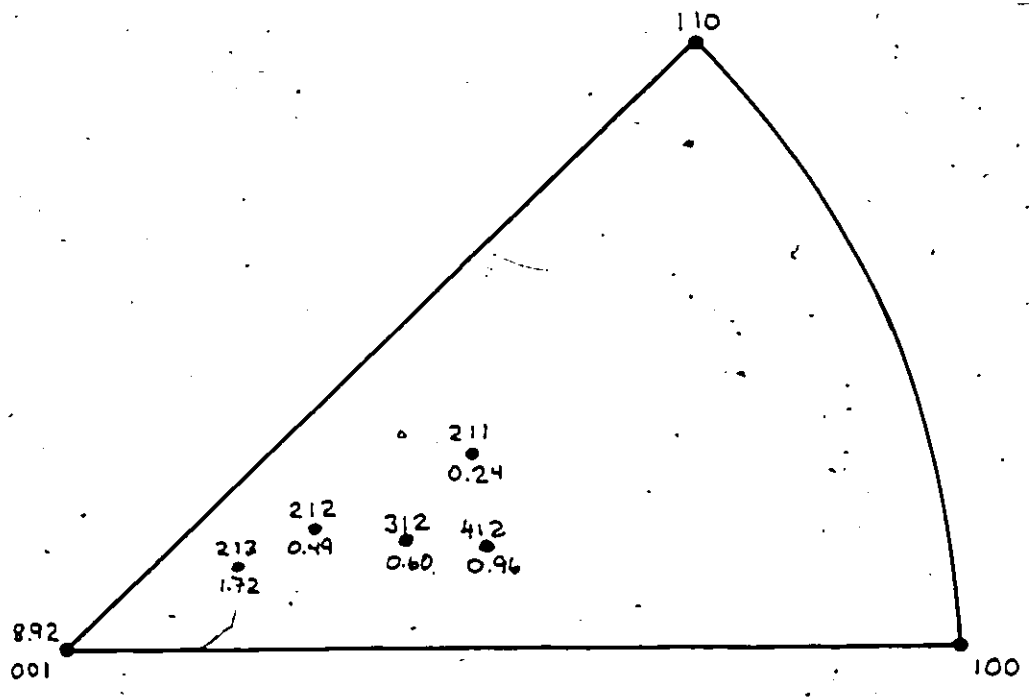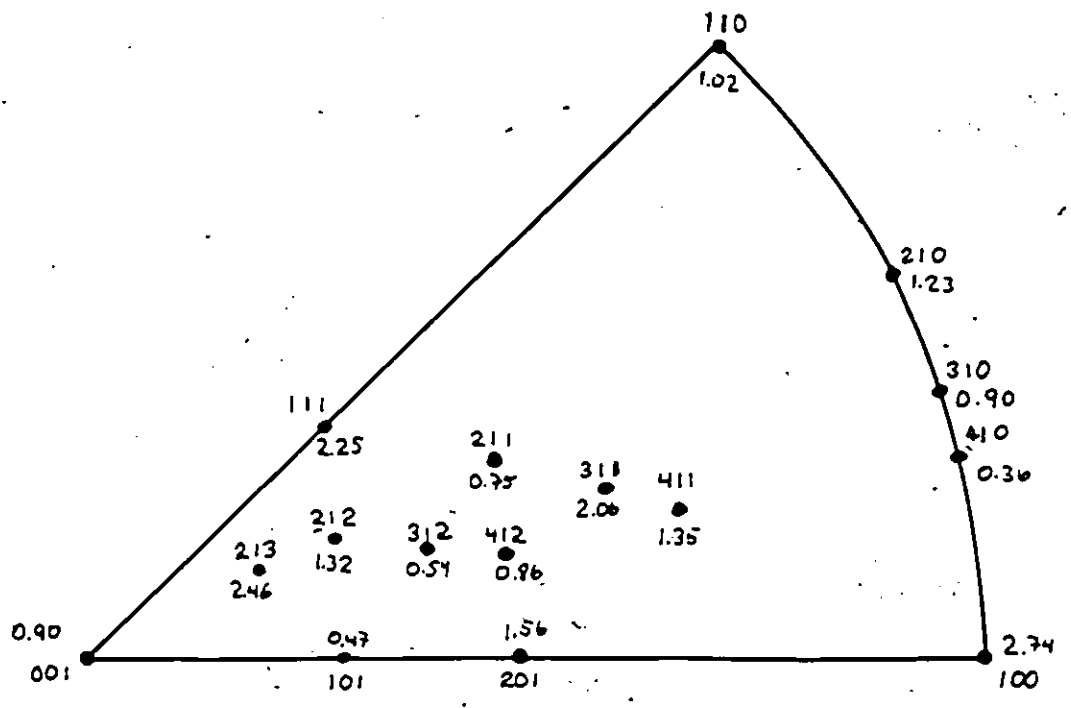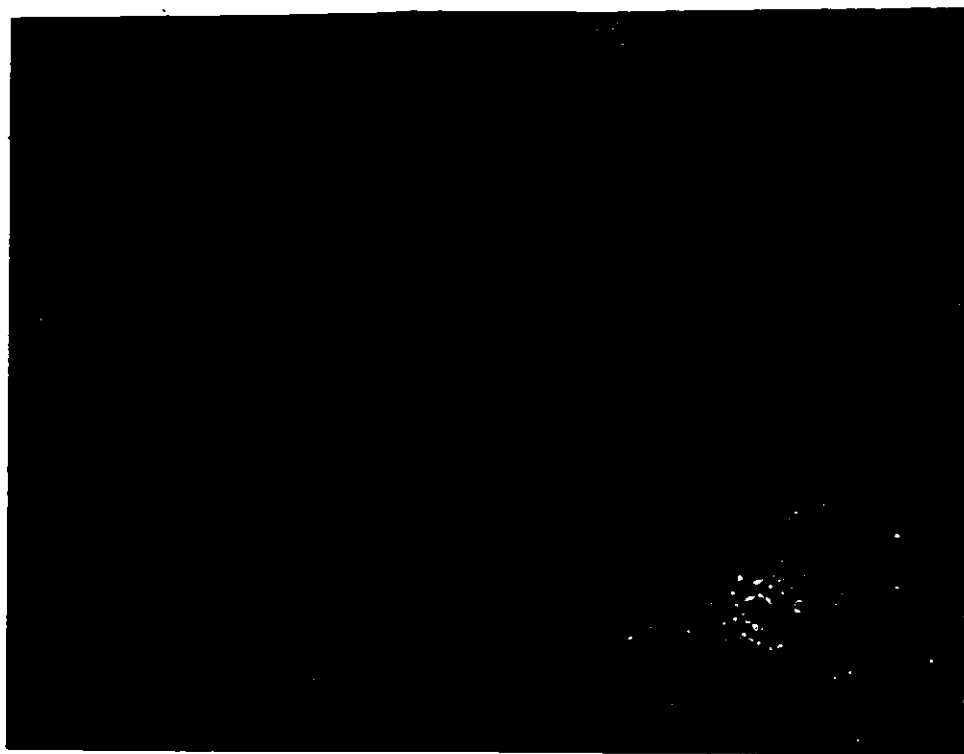
250 μm

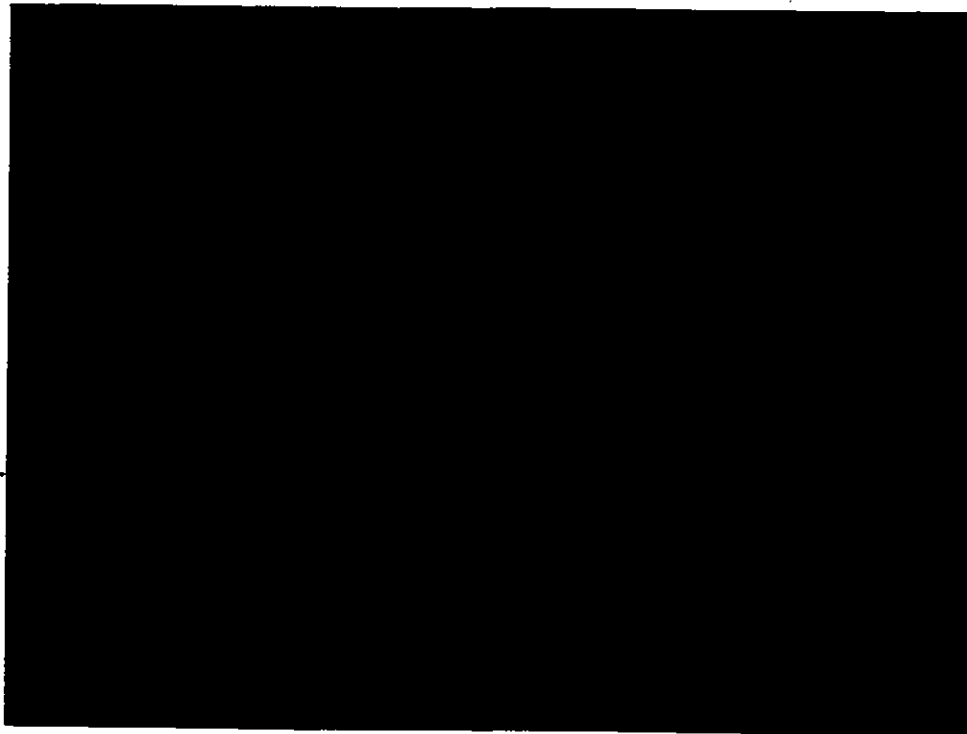Figure 44: Optical micrograph of B2TS2 thin film deposited on (100)Si at 675°C for 6 hours (400X).
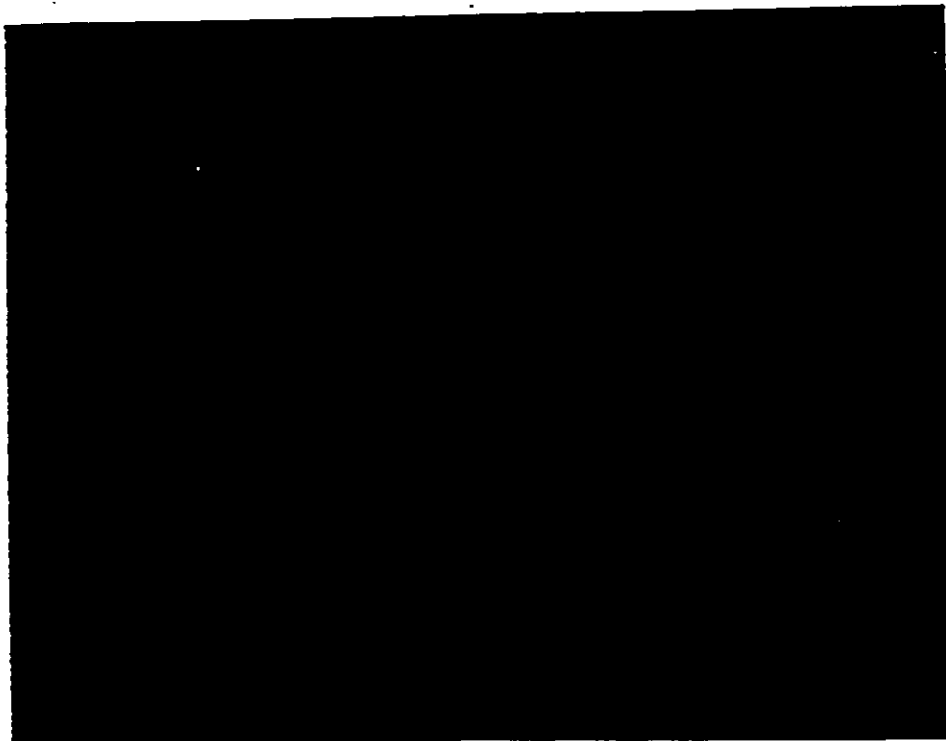
250 μm

Figure 45: Optical micrograph of B2TS2 thin film deposited on (100)Si at 700°C for 6 hours (400X).
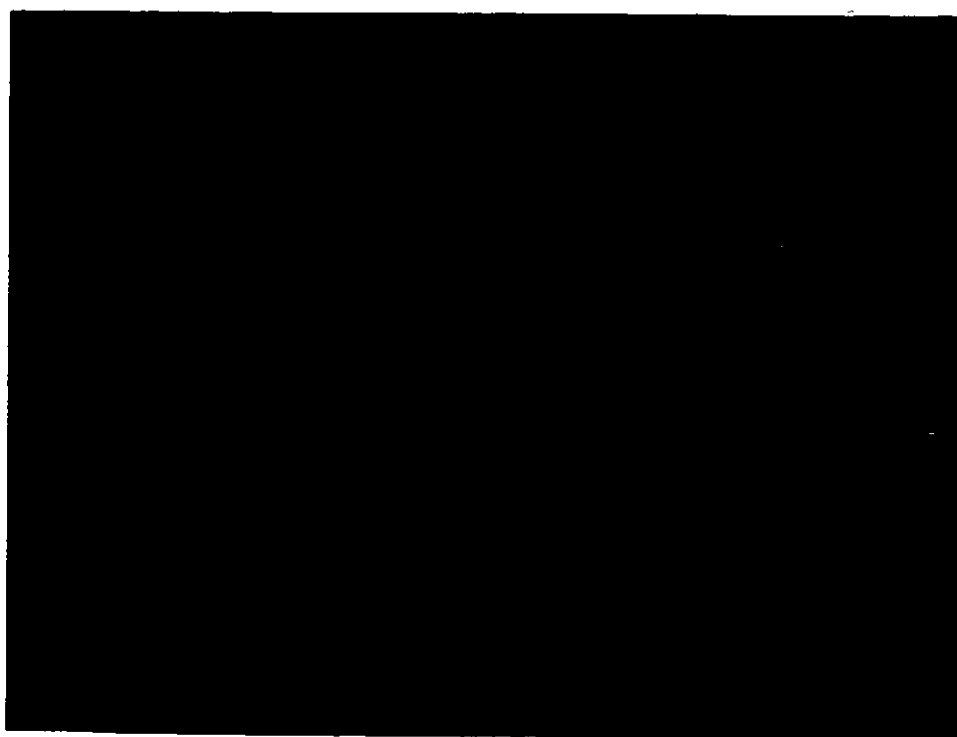
250 μm

Figure 46:   Optical micrograph of B2TS2 thin film deposited
             on (100)Si at 725°C for 7 hours (400X).
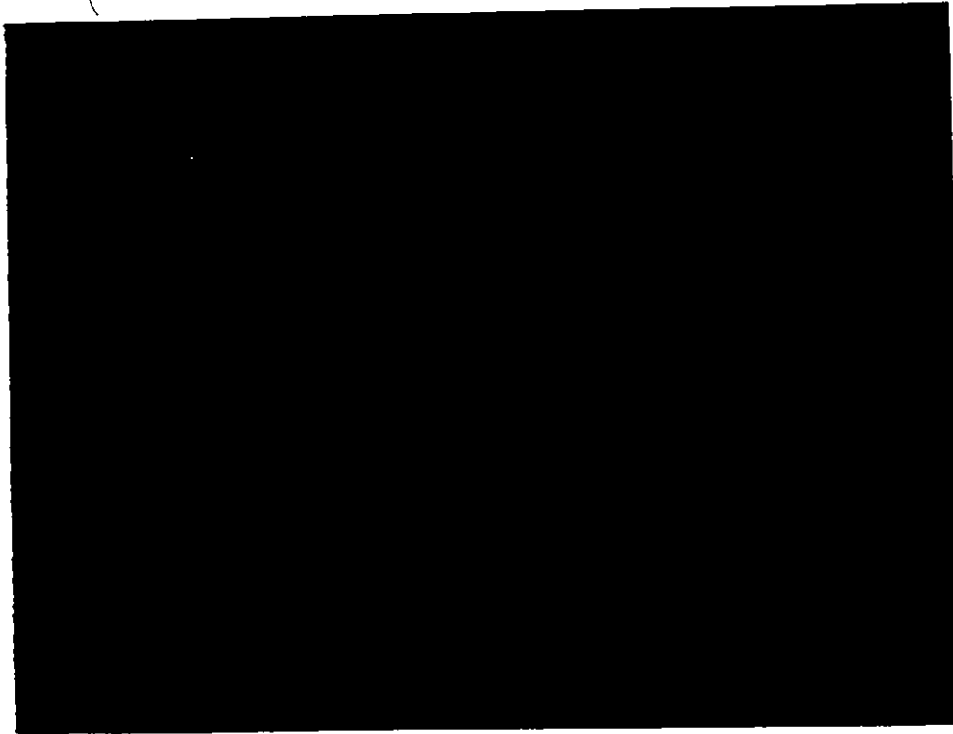
250 μm

Figure 47: Optical micrograph of B2TS2 thin film deposited
on (100)Si at 750°C for 7 hours (400X).

250 μm

Figure 48: Optical micrograph of B2TS2 thin film deposited on (100)Si at 775°C for 8 hours (400X).
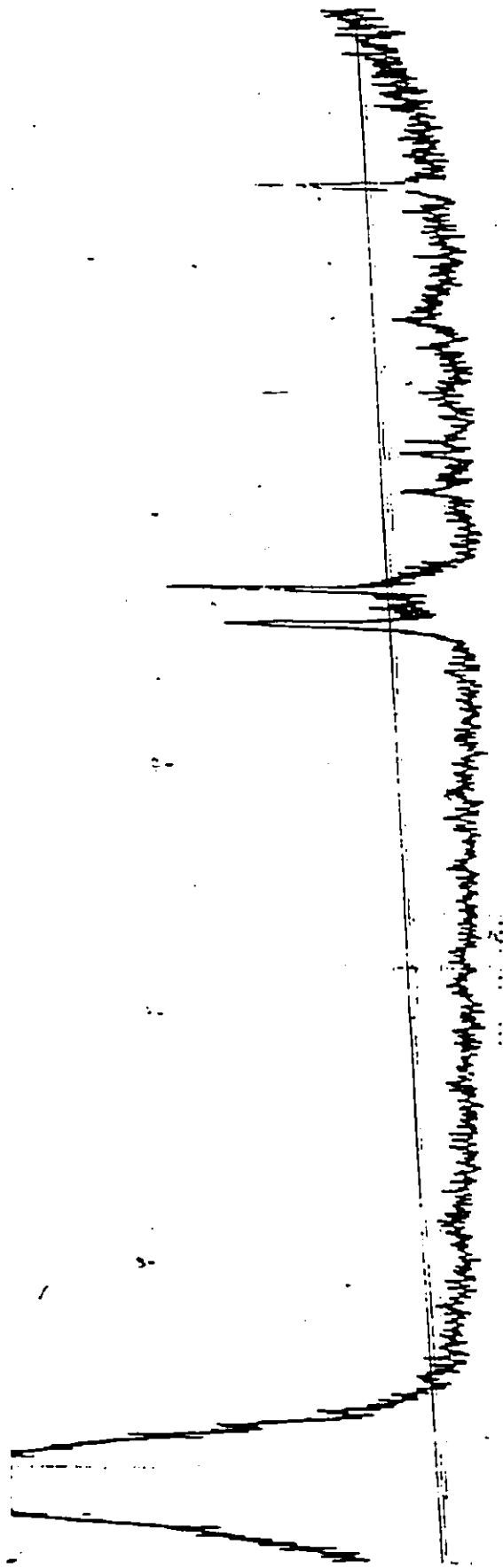
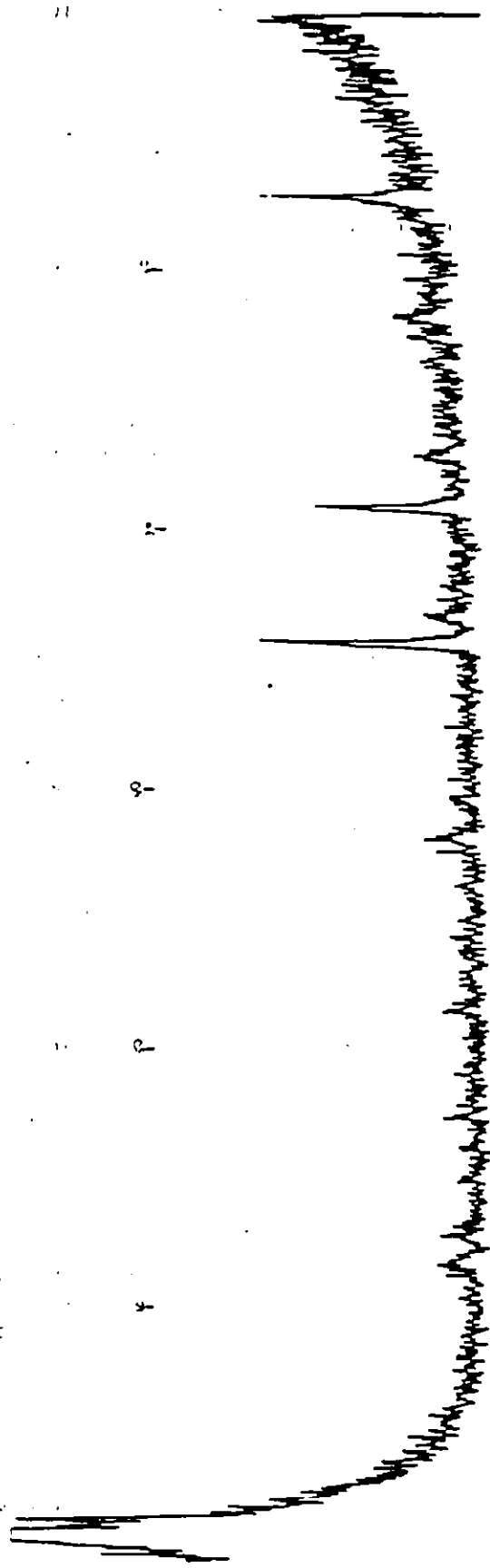Figure 49: XRD pattern of B2TS2 thin film deposited on (100)Si at 700°C for 8 hours.
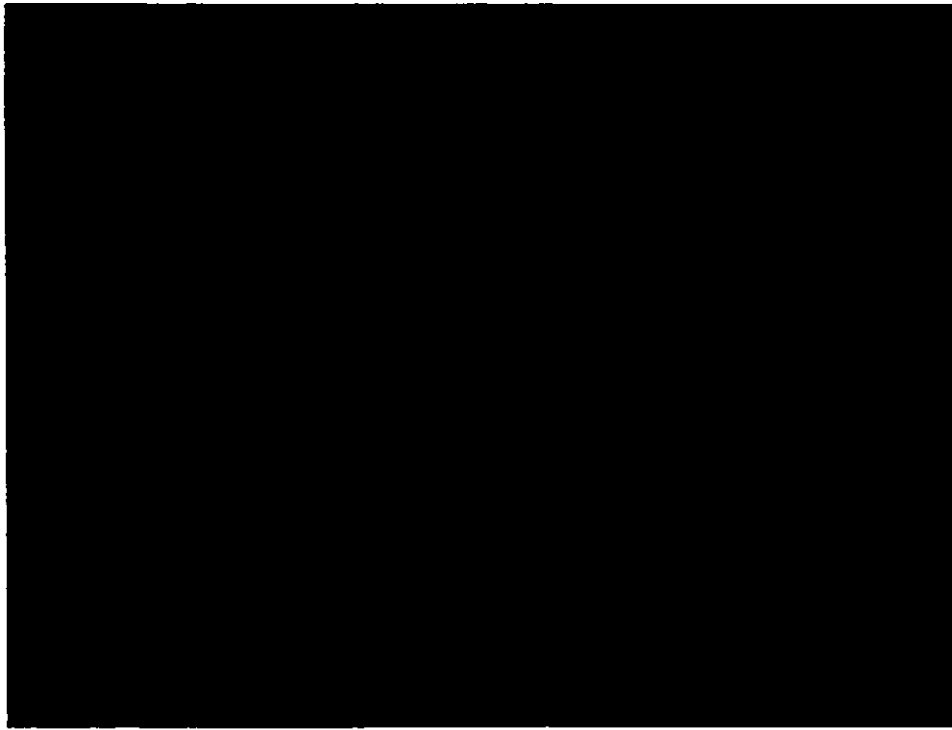
250 μm

Figure 50: Optical micrograph of B2TS2 thin film deposited on (100)Si at 700°C for 8 hours (400X).
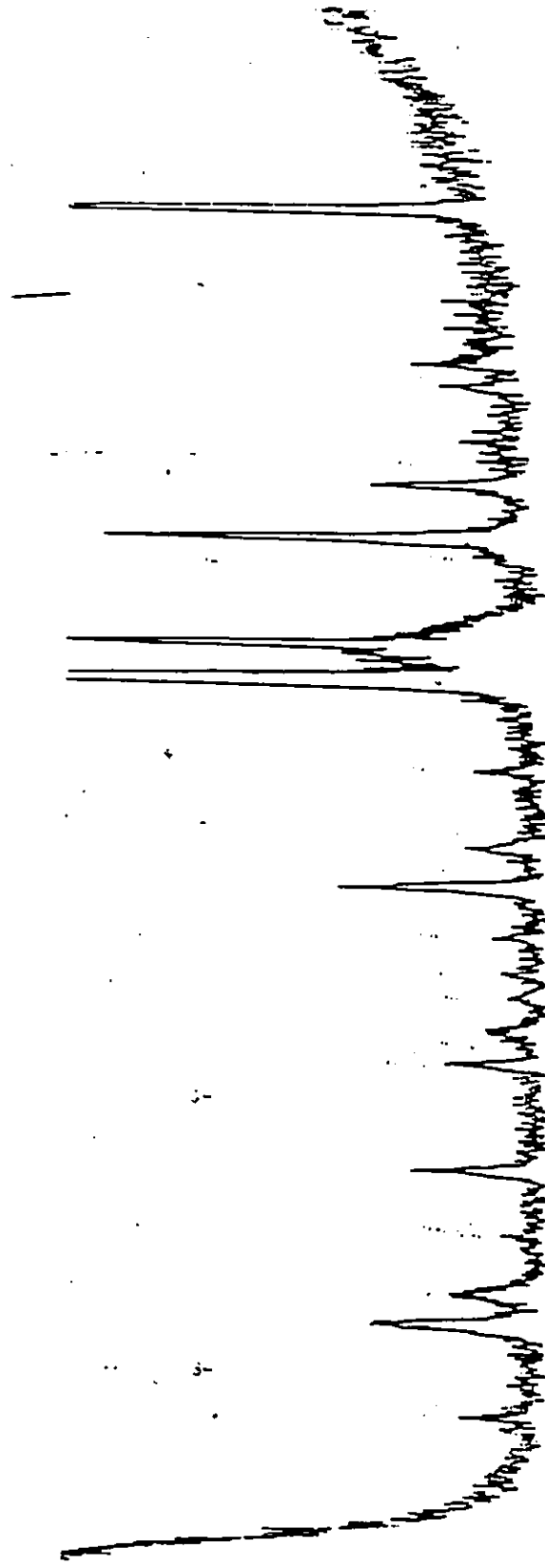
Figure 51: XRD pattern of B2TS2 thin film deposited on (100)Si at 725°C for 13 hours.
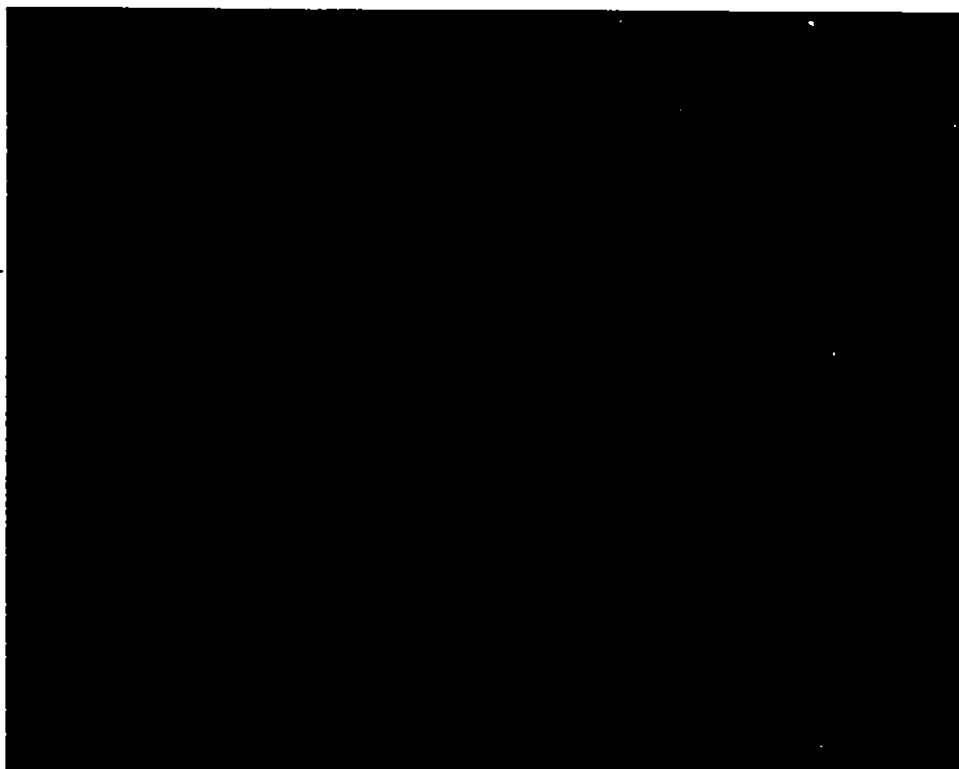
250 μm

Figure 52:   Optical micrograph of B2TS2 thin film deposited
on (100)Si at 725°C for 13 hours (400X).

Figure 53: XRD pattern of B2TS2 thin film deposited on (100)Si
at 725°C for 2 hours.
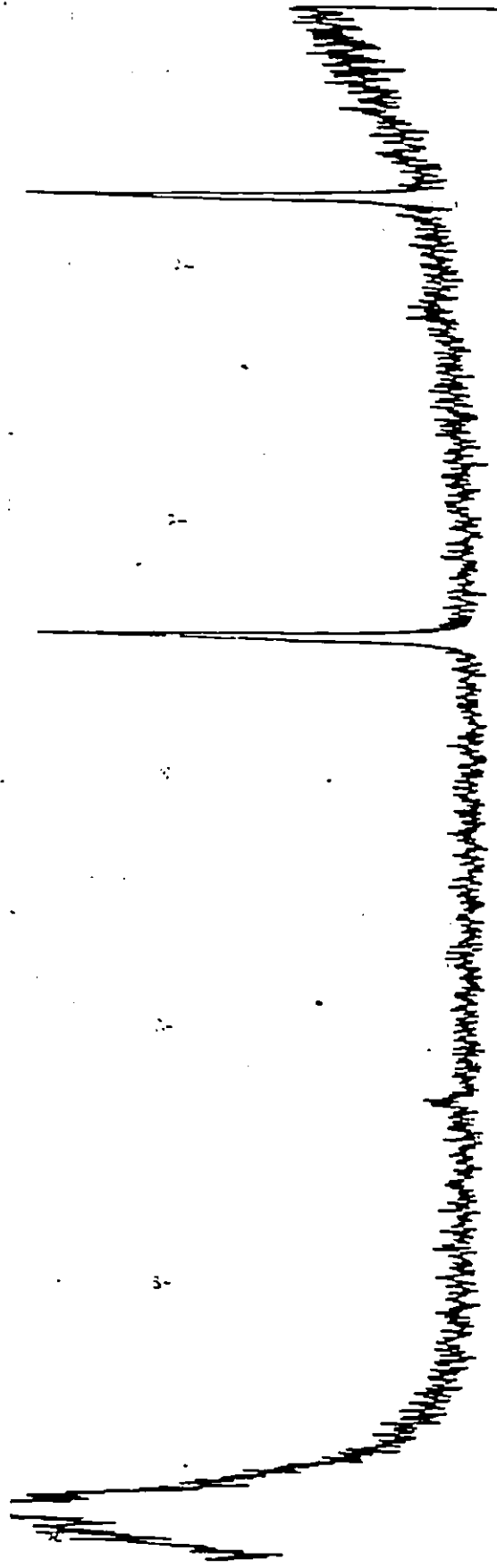
Figure 54: XRD pattern of B2TS2 thin film deposited on (100)S1
at 725 C for 3.5 hours.

250 μm

Figure 55: Optical micrograph of B2TS2 thin film deposited on (100)Si at 725°C for 3.5 hours (400X).

250 μm

Figure 56:   Optical micrograph of B2TS2 thin film deposited
             on (100)Si at 725°C for 5.5 hours (400X).

Figure 57: XRD pattern of B2TS2 thin film deposited on (100)Si at 725°C for 5.5 hours.

Figure 58: XRD pattern of B2TS2 thin film deposited on (100)Si
at 725°C for 4 hours and 700°C for 6 hours

(a)   250 μm

(b)

Figure 59:   Optical micrographs of B2TS2 thin film deposited
             on (100)Si a) 725°C for 4 hours and b) 700°C for
             6 hours (400X).

Figure 60: XRD pattern for B2TS2 thin film deposited on (100)Si at 725°C for 4 hours and 675°C for 6 hours.

250 μm

Figure 61: Optical micrograph of B2TS2 thin film deposited on (100)Si at 725°C for 4 hours plus 675°C for 6 hours (400X).
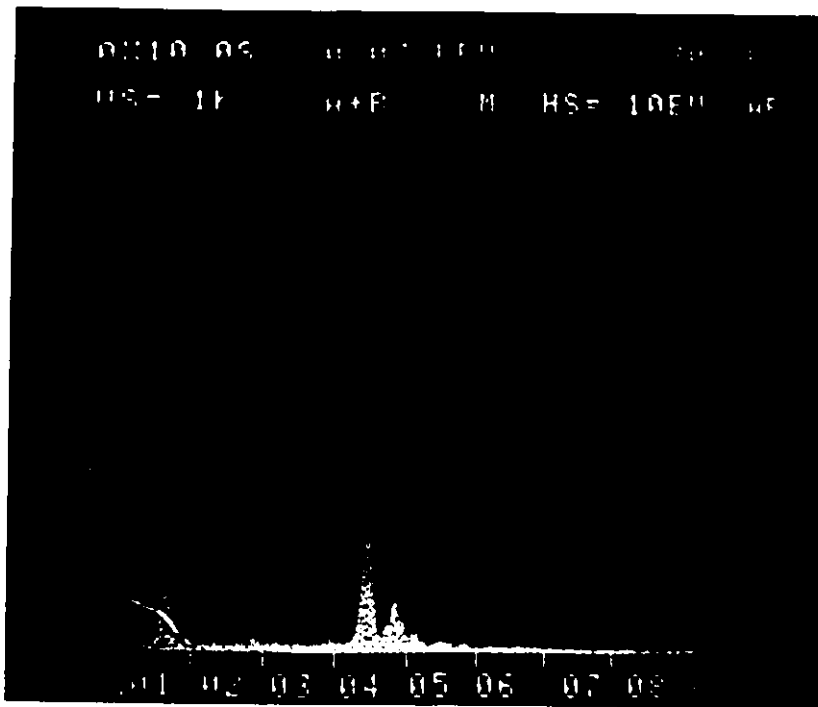
Figure 62: EDS analysis of B2TS2 thin films.
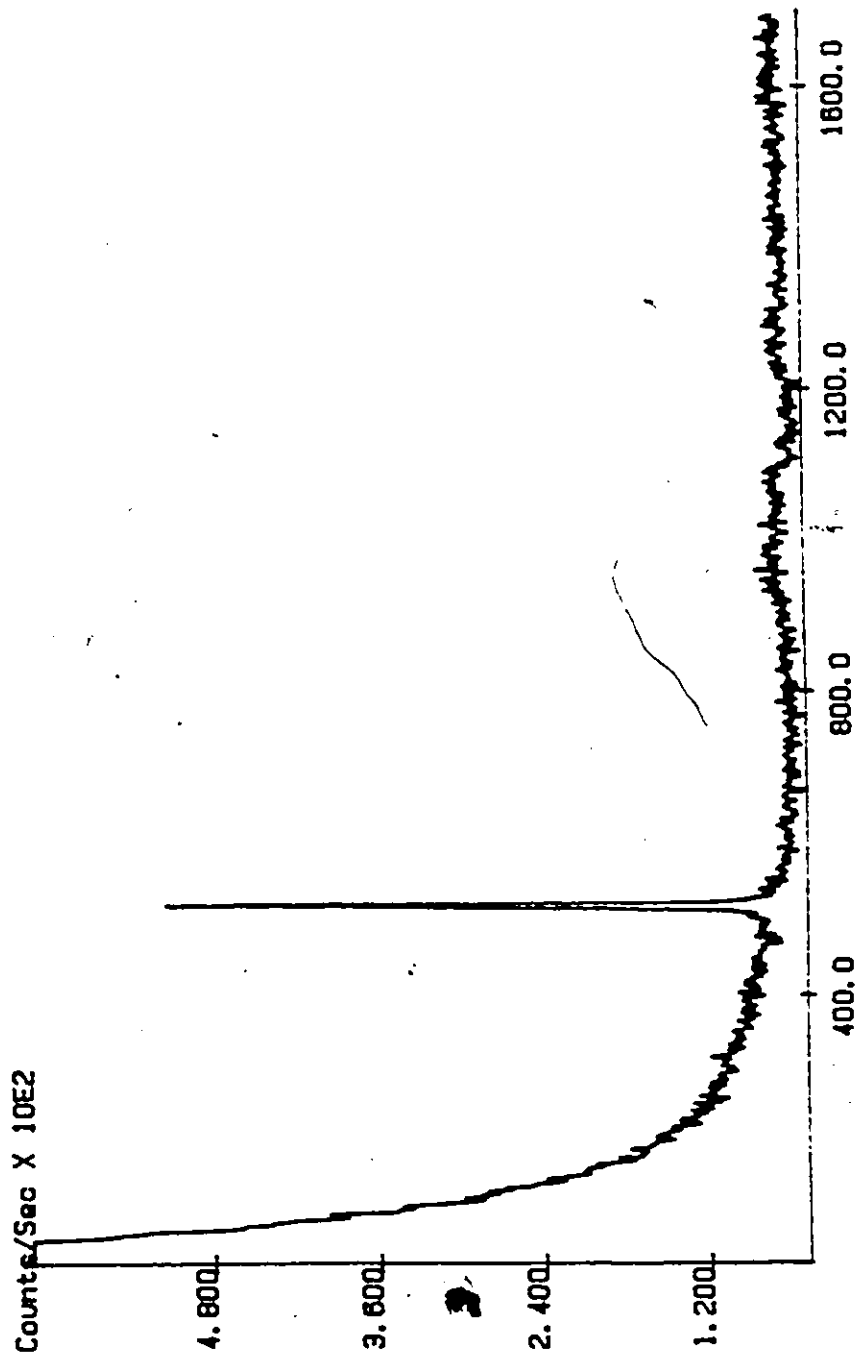
Figure 63: Raman spectroscopy analysis of:
a) (100) silica substrate and the B2TS2
    thin film deposited at:
b) 675° for 6 hours
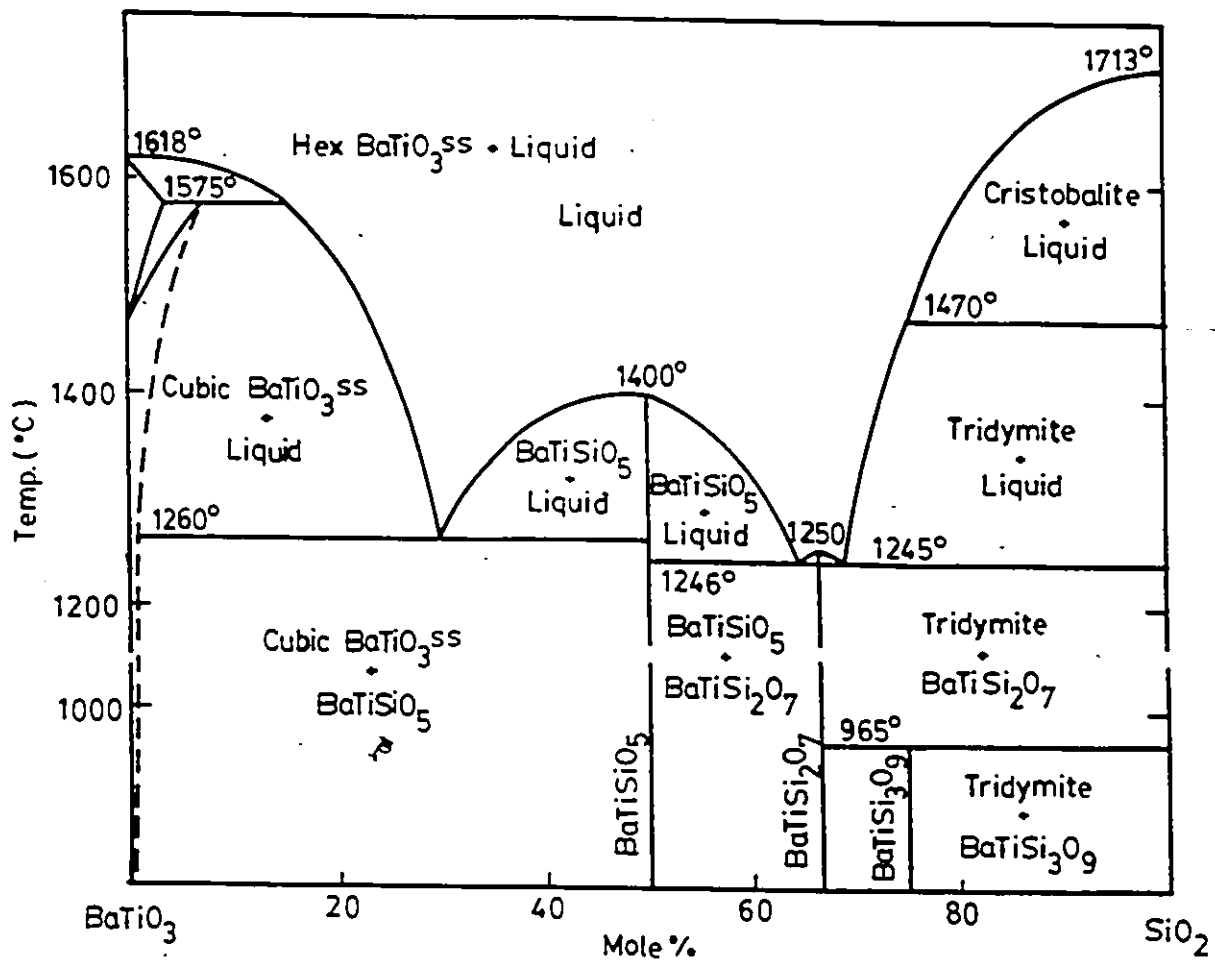c) 725° for 7 hours
d) 775°C for 8 hours

63 (b)

63.-(c)

Counts/Sec X 10E3
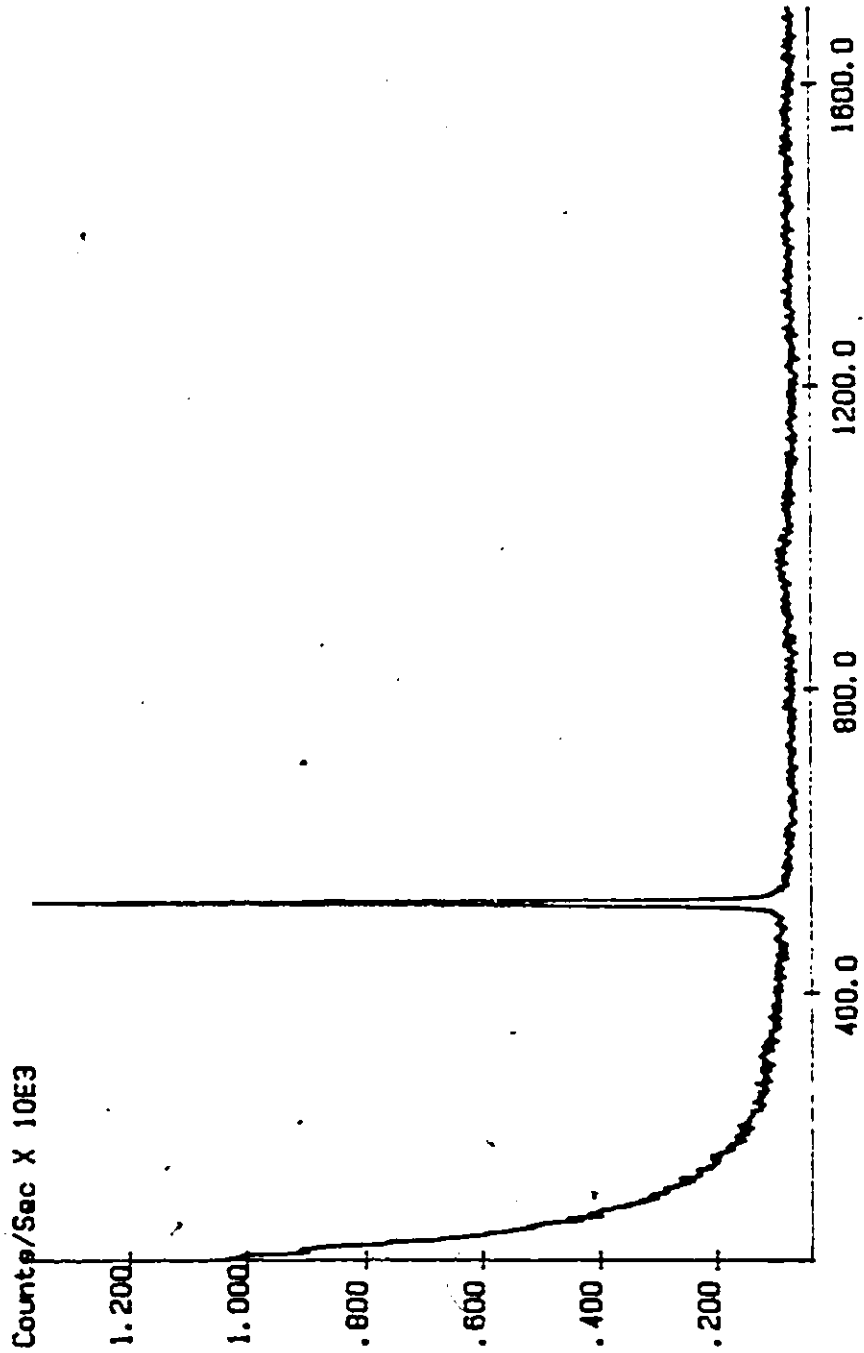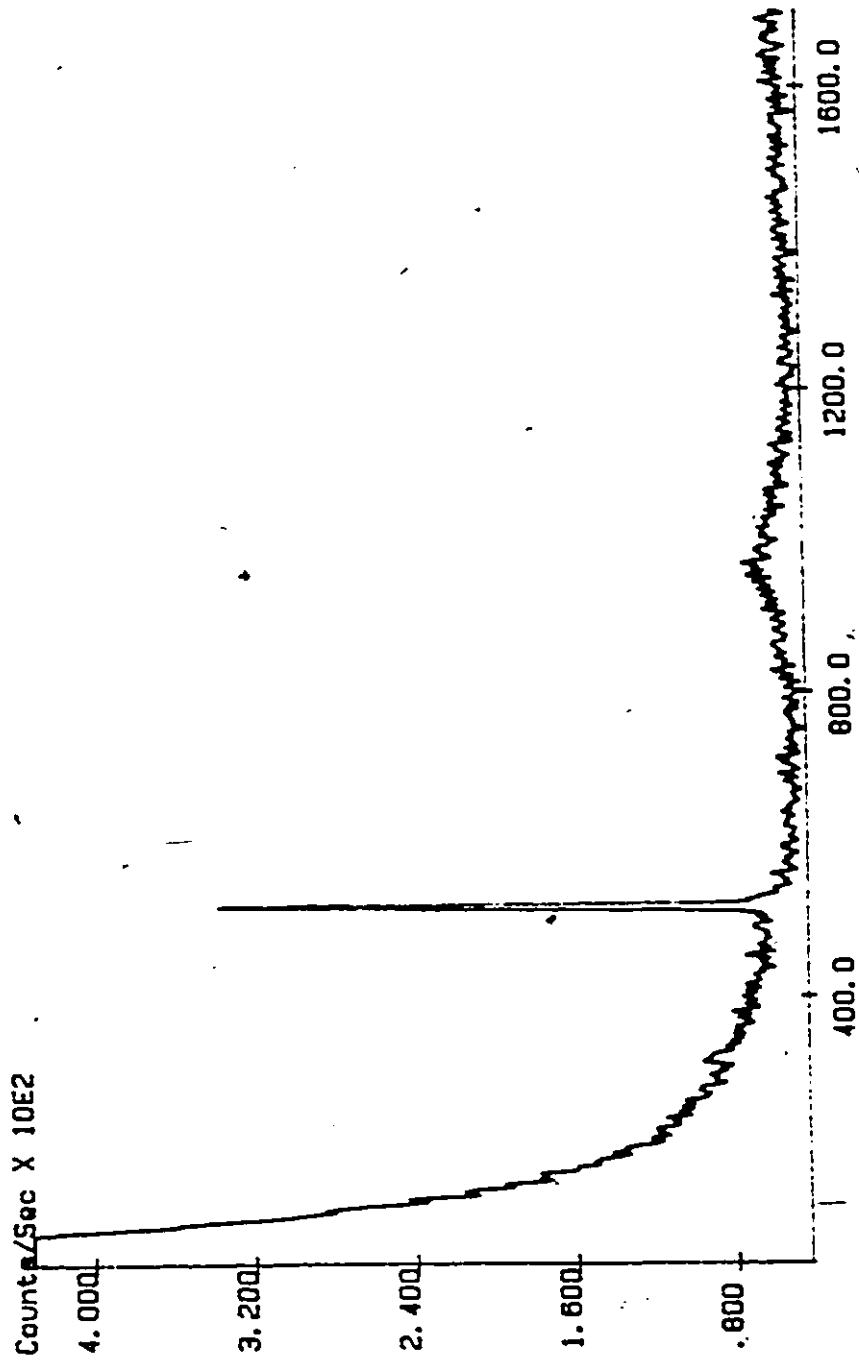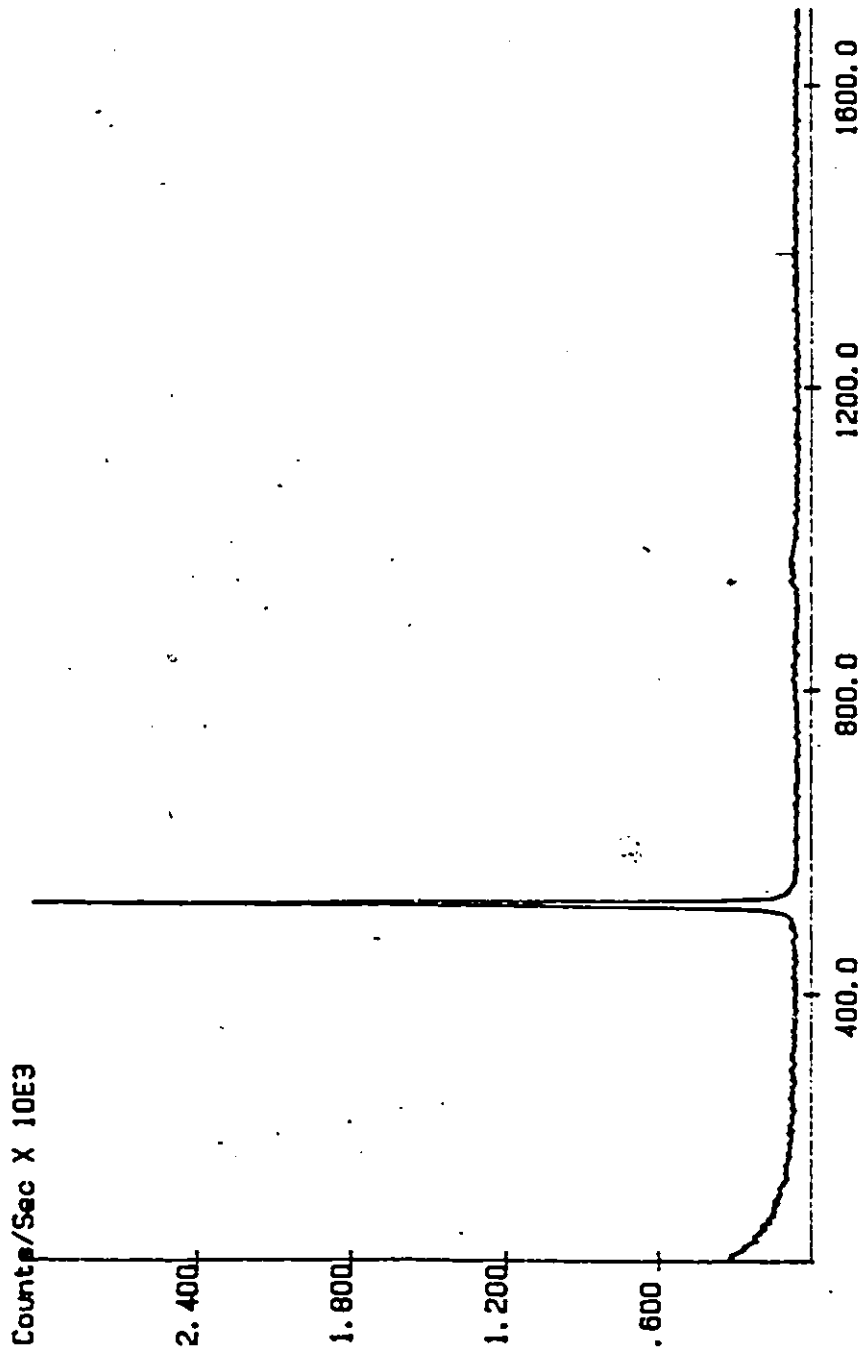
63 (d)

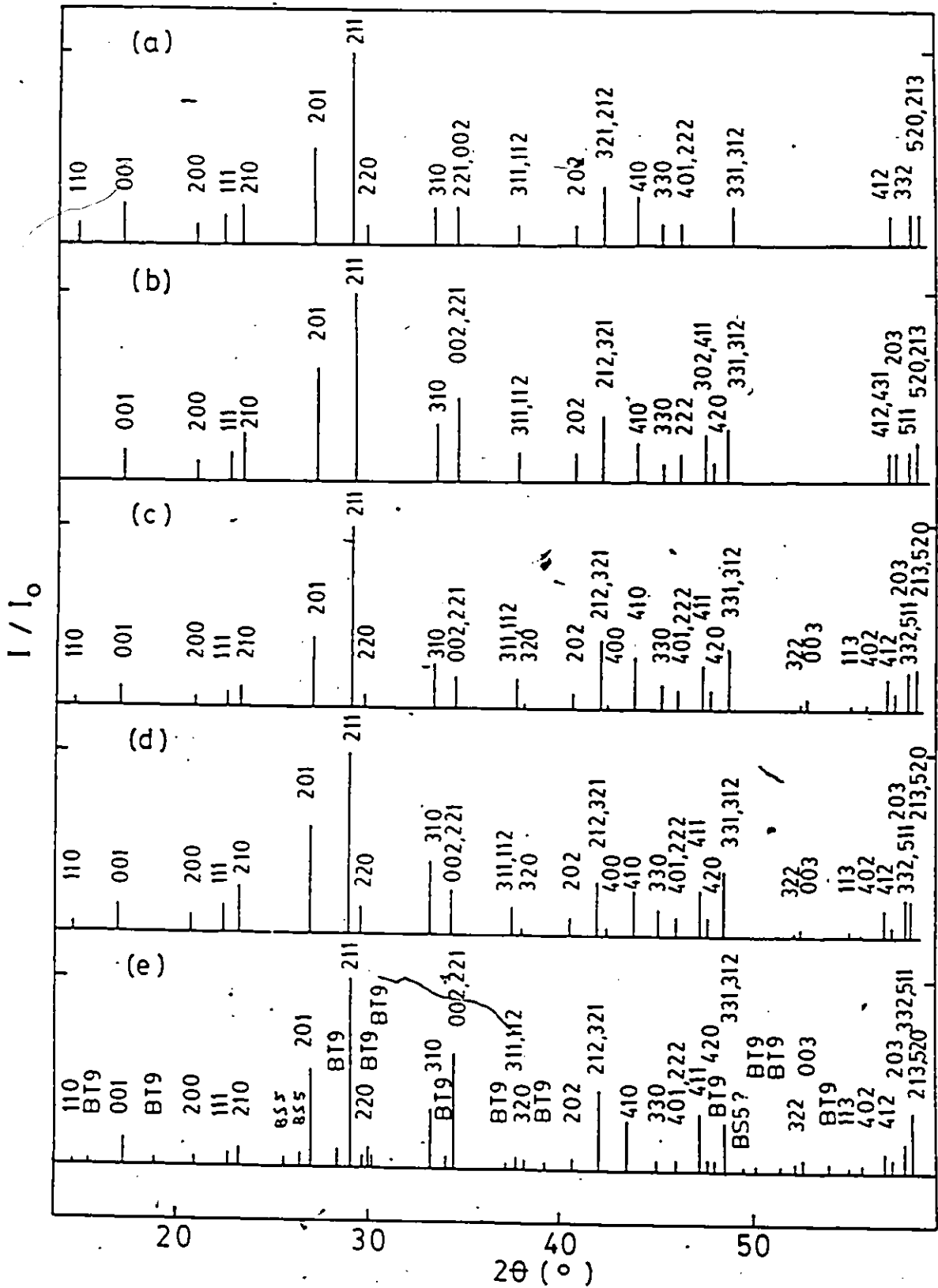Figure 64: Phase equilibrium diagram for the $BaTiO_3$ - SiO_2 system [66]

Figure 65: X-ray diffraction patterns, when CuKα radiation is used, of
(a) $Ba_2TiSi_2O_8$ (from JCPDS data), (b) $BaTiSiO_5$ (from JCPDS
data), (c) $Ba_2TiSi_2O_8$ (calculated), (d) $Ba_2TiSi_2O_8$ (fabricated
at 1300°C), and (e) "$BaTiSiO_5$" (fabricated at 1250°C). All the
indices are those for $Ba_2TiSi_2O_8$.

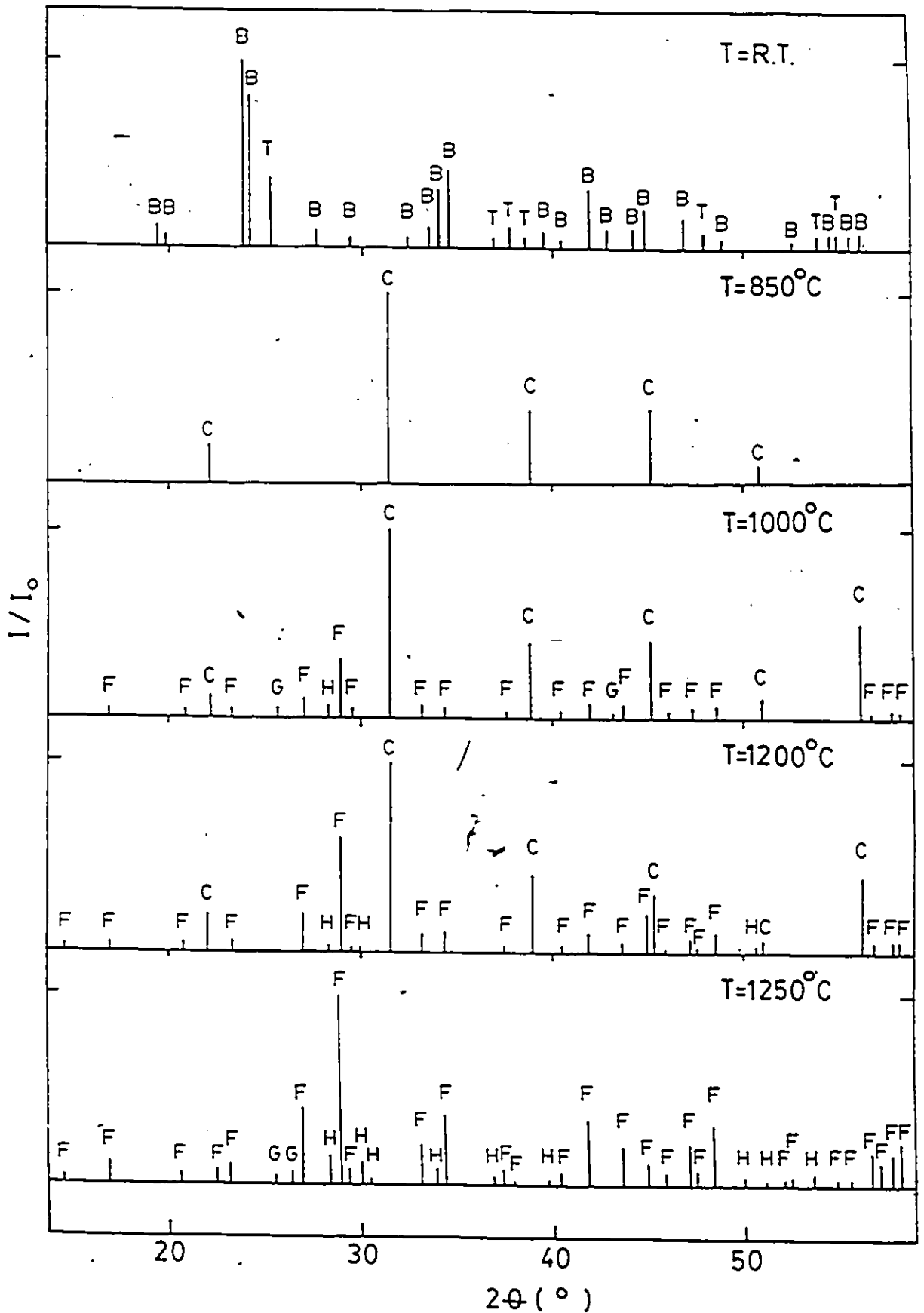Figure 66: X-ray diffraction patterns, when CuKα radiation was used, of the mixture of fine powders of $BaCO_3$, TiO_2, and SiO_2 with Ba:Ti:Si ratios of 1:1:1 which were heated at the indicated temperatures.
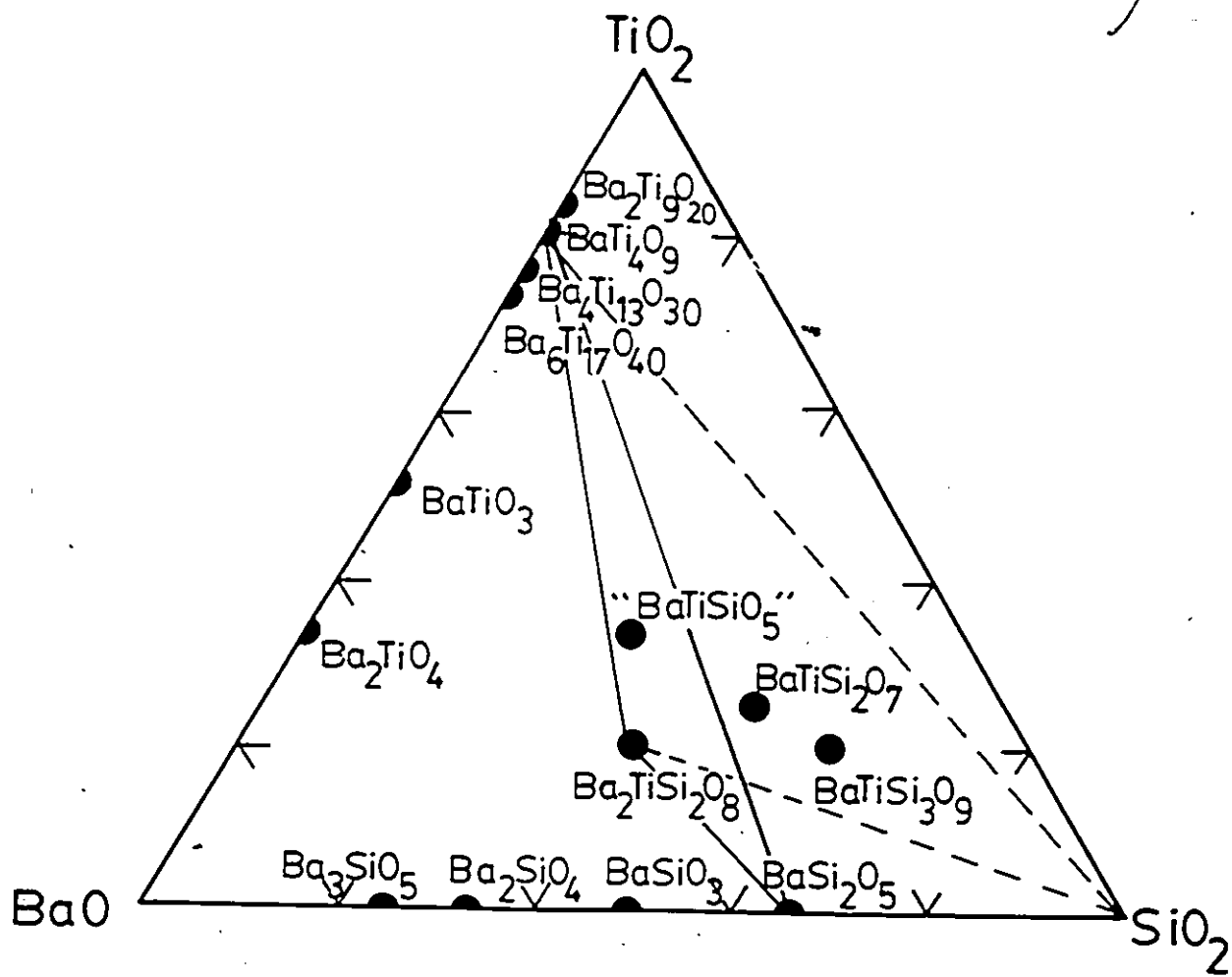
Figure 67   Gibbs triangle for the BaO – TiO_2 – SiO_2 system with major compound phases.   Triangles indicate possible phase relations of composition "$BaTiSiO_5$" at 1250°C